Folding and Dynamic Deployment of Ultralight Thin-Shell Space Structures

Thesis by
Narravula Harshavardhan Reddy

In Partial Fulfillment of the Requirements for the
Degree of
Doctor of Philosphy

CALIFORNIA INSTITUTE OF TECHNOLOGY
Pasadena, California

2023
Defended May 9, 2023

Narravula Harshavardhan Reddy
ORCID: 0000-0003-3897-8162

ACKNOWLEDGEMENTS

I dedicate this thesis to
my mother: Siva Parvathi,
and my teachers:
Prof. Sergio Pellegrino,
Dr. Prashant Saxena,
Dr. Satyajit Panda,
Dr. Priyankoo Sarmah,
and Ms. Mary Nirmala.

I am grateful to the Caltech Space Solar Power Project for funding this research, and to the GALCIT fellowship for supporting for my Master's studies at Caltech. I also thank the Caltech's Center for Autonomous Systems and Technologies (CAST) for lending the motion capture equipment needed for my experiments.

Special thanks to my PhD advisor Prof. Sergio Pellegrino for the wonderful opportunity of working with him. He has been extremely supportive, kind, and perceptive. He provided me with multiple opportunities and facilities to explore all the approaches of research — analytical, numerical, and experimental. I worked on quite a few projects in the beginning with little progress that was not worth publishing. I had to go through several learning curves which required huge amount of time. Prof. Pellegrino was patient and guided me at every step towards progress. Thanks to him, I discovered my affinity for experiments. This discovery instilled confidence in my abilities, and the research thereafter has been much more joyful. The experiments I performed and the corresponding numerical simulations form the bulk of this thesis.

I thank my colleague and friend Alan Truong for his incredible help with composite manufacturing, CAD modelling, and deployment tests; Alexander Wen for his help with CAD modelling and material testing, and his invaluable feedback on my presentations; Uba K. Ubamanyu for his help with composite manufacturing, and his invaluable feedback on my presentations; Noel Esparza-Duan and Michael O'Connell for his help with the motion capture equipment.

I thank the GALCIT incoming students of 2017: Alex Wen, Uba K. Ubamanyu, Kai Matsuka, Michael O'Connell, Avinash Chandra, Kira Hendrick, Jean-Sebastien Spratt, Emile Oshima, Ben Reviere, Conor Martin, Wesley Yu, and Hiro Tsukamoto for their comradierie which made me feel home at Caltech.

I also thank the past and present members of the Space Structures Lab: Antonio Pedivallano, Christophe Leclerc, Serena Ferraro, Yuchen Wei, Fabien Royer, Michael Marshall, Charlie Dorn, Yang Lee, Armanj Hasanyan, Charles Sommer, Alan Truong, Terry Gdoutos, Wen Luo, Jaden Suh Uba K. Ubamanyu, Alex Wen, Gianfranco Canales, John Pederson, Sahangi Dassanayake, Brayden Aller, Meital Carmi, Divesh Soni, George Popov, and Federico Benazzo for their friendship, feedback and help with my research.

ABSTRACT

Thin-shell structures are becoming increasingly popular for space missions due to their high stiffness-to-mass ratio, easy folding and coiling, and self-deployment using stored strain energy. Broadly, two deployment strategies exist: 1) controlled or deterministic, and 2) unconstrained. Controlled deployment involves carefully orchestrated events using control or guidance systems, while in unconstrained deployment, the structure is simply allowed to self-deploy with minimal guidance. Unconstrained deployment offers lighter deployment mechanisms and better packaging efficiency but the unpredictability of this process has been a significant obstacle to its adoption.

This study focuses on demonstrating the predictability of unconstrained dynamic deployment of thin-shell structures, using the Caltech Space Solar Power Project (SSPP) structures as a case study. The Caltech SSPP uses composite triangular rollable and coilable longerons as the primary building blocks to create large bending-stiff structures. The specific objective is to improve the predictability and robustness of the unconstrained dynamic deployment of the Caltech SSPP structures. Deployment is influenced by the initial conditions and the interaction between the structure and the mechanism during the deployment. To understand these effects, high-fidelity numerical simulations are developed and validated against experiments. The study also examines the sensitivity of deployment characteristics to various design parameters and external influences to ensure the robustness of deployment.

This research demonstrates that the interaction between the structure and the deployment mechanism must be minimal to ensure the predictability of deployment, as thin-shell structures can self-deploy using stored strain energy. This study's sensitivity analysis will inform the design of future SSPP deployment mechanisms and structures. Additionally, the numerical simulation techniques developed have broader applicability beyond this specific case study to any deployable thin-shell structure.

Due to the large aspect ratios of thin-shell structures, a very fine finite element mesh is required to model them accurately. A dense finite element mesh is also required to model the contact interactions between the structure and the rigid components of the deployment mechanism. As large spacecraft structures become increasingly complex, full-scale numerical modeling becomes impractical, necessitating

the search for more computationally efficient finite element methods. In this study, NURBS-based isogeometric analysis is explored, and it is shown that it is not yet worth switching to NURBS-based elements for the analysis of thin-shell deployable structures. In addition, h-adaptive meshing for quadrilateral shell elements is investigated, and more efficient refinement indicators and solution mapping techniques for nonlinear analyses are proposed and their superior performance is demonstrated using a test case of quasi-static folding of a tape spring.

This thesis fills a gap in the literature on unconstrained dynamic deployment of space structures, providing crucial insights and numerical modeling tools for further research. It establishes a knowledge and resource foundation to advance space structure design and promote more frequent use of unconstrained deployment, marking a pivotal contribution to the field and enabling safe and efficient space structure deployment. Furthermore, the study provides insights into more computationally efficient finite element methods, such as h-adaptive meshing. These insights are broadly applicable and can inform the design of future deployable structures beyond the tested cases.

PUBLISHED CONTENT AND CONTRIBUTIONS

[1] N. H. Reddy and S. Pellegrino, "Dynamics of the Caltech SSPP deployable structures: Structure–mechanism interaction and deployment envelope," in *AIAA SciTech 2023 Forum*, 2023, p. 2065. DOI: 10.2514/6.2023-2065,

N.H.R. participated in the conception of the project and in designing the experimental setup, performed the experiments and numerical simulations, analyzed the results, and participated in the writing of the manuscript.

[2] N. H. Reddy and S. Pellegrino, "Time-efficient geometrically non-linear finite element simulations of thin shell deployable structures," in *AIAA SciTech 2021 Forum*. 2021, p. 1795. DOI: 10.2514/6.2021-1795,

N.H.R. participated in the conception of the project, performed the simulations, analyzed the results, and participated in the writing of the manuscript.

TABLE OF CONTENTS

LIST OF ILLUSTRATIONS

LIST OF TABLES

Chapter 1

INTRODUCTION

1.1 Motivation

Deployable structures are designed to be compact and easy to transport, but can unfold and expand to create a large and stable structure. The concept of deployable structures has been around for many centuries and has been used extensively in a wide range of applications, both on the ground and in space.

Deployable structures are particularly useful for space applications because they offer a practical solution to the challenges of weight and volume. They can be efficiently packed for launch and then deployed in space to form large structures that would otherwise be impossible to launch in their fully assembled states. This helps to reduce the cost and complexity of launching payloads into space.

While majority of the deployable spacecraft flown to space used rigid elements such as trusses or panels to support lightweight surfaces, the more recent deployable space structures utilize thin-shell components due to their lightweight and flexible nature. Thin-shell structures are better than their rigid counterparts because they offer a higher stiffness-to-mass ratio, higher packaging efficiency, and simplified actuation. Their curved cross-sections provide high moments of inertia, resulting in high bending stiffness despite their thin walls. Additionally, the shape of their cross-section allows them to be elastically collapsed and often coiled into compact volumes. Some examples of space missions utilizing thin-shell deployable components include the Roll-Out Solar Array (ROSA) [2], NASA's Advanced Composite Solar Sail System [3], and MARSIS radar antenna consisting of flattenable and foldable tubes [4].

There are two main types of deployment strategies for thin-shell deployable structures: controlled or deterministic deployment and unconstrained deployment. Controlled deployment involves a carefully orchestrated sequence of events to deploy the structure, typically using motors or other actuators. This approach ideally allows for a high degree of predictability and accuracy in the deployment process, ensuring that the structure unfolds exactly as planned. However, the required deployment mechanism for controlled deployment would be complex and the complexity may increase with the size of the structure. This results in lower packaging efficiency and

higher launch costs. Examples of space missions that use this type of deployment are plenty. James-Webb Space Telescope, NASA's Advanced Composite Solar Sail System are a few examples.

On the other hand, in unconstrained deployment, the structure is simply released and allowed to deploy on its own by releasing the stored strain energy. The deployment may, however, be guided by pulling the structure outward at specific points. Unconstrained deployment has been rarely used in space missions as it can be less predictable and more difficult to control once the deployment process begins. However, since unconstrained deployment does not require extensive control and guidance systems to guide the deployment at every step, it can potentially lead to lighter and more efficient deployable spacecraft. Also for this reason, such a deployment can be quite complex and challenging to predict. An example of a space mission that uses unconstrained dynamic deployment is the Caltech Space Solar Power Project (SSPP).

The majority of the space structures that use thin-shell deployable components use them as antennas [5], hinges [6]–[8], deployable booms [9]–[11], and compression elements to support and pretension thin membranes ([2], [12]). This means that only a small part or a small percentage of the overall spacecraft has stored strain energy in the stowed configuration. On the other hand, the innovative architecture of Caltech Space Solar Power Project (SSPP) utilizes thin-shell foldable and coilable components as the primary building blocks to create large bending-stiff structures (Figure 1.1. A significant percentage of the overall spacecraft has stored strain energy when stowed and hence an unconstrained deployment is the ideal choice.

The Caltech SSPP conceptualizes a constellation of spacecraft that host functional elements to collect solar energy in space and wirelessly transmit them to a receiving stating on the Earth. The modular structural architecture of each spacecraft (Figures 1.1 1.2, and 1.3) consists of bending-stiff trapezoidal strips built from two foldable composite longerons with a TRAC cross-section [13] each that are connected by battens. The strips form structurally independent modules and are attached to diagonal cords suspended between the tips of four diagonal booms and a central mechanism.

Studies of the fundamentals of unconstrained deployment are relatively rare. Majority of the structural design approaches in the current literature only consider stowed and deployed configurations [14]. However, it is crucial to consider the intermediate dynamics of deployment to optimize the design of the structures as well as the

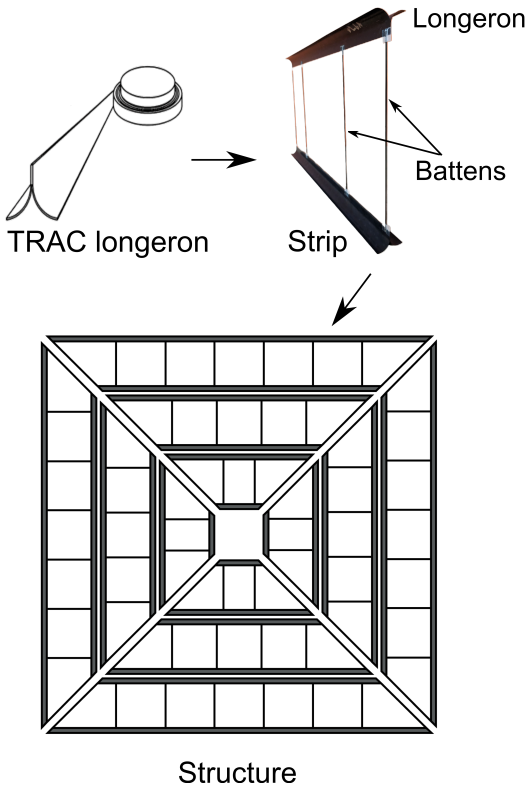

Figure 1.1: Bottom up construction of an SSPP deployable structure.

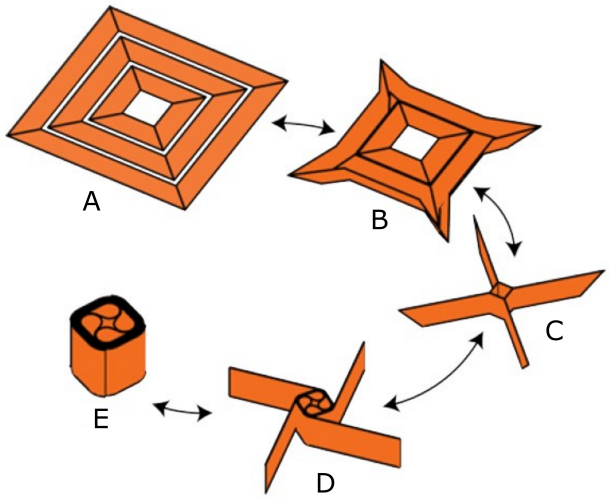

Figure 1.2: Packaging and deployment concept. Focus of this study is on the deployment process (C to A).

deployment mechanisms. Future advancements in the field of deployable structures depend on the ability to accurately model and simulate the dynamics during deployment, enabling the successful deployment of large precision deployable structures in deep space missions [14].

These gaps can be filled by studying the complex dynamic deployment of the Caltech SSPP. Methods developed in the process and the knowledge gained from such a study will also be applicable to the deployment of a wide variety of thin-shell space structures outside of this project.

1.2 Challenges in studying dynamic deployment of Caltech SSPP

Vast amount of literature is available on the Caltech SSPP including the concept, manufacturing, packaging and deployment [15]–[23]. The latest version of the deployable structure as it was flown into the Low Earth Orbit has three strips per quadrant and is of the approximate size 1.7 m × 1.7 m (Figure 1.1).

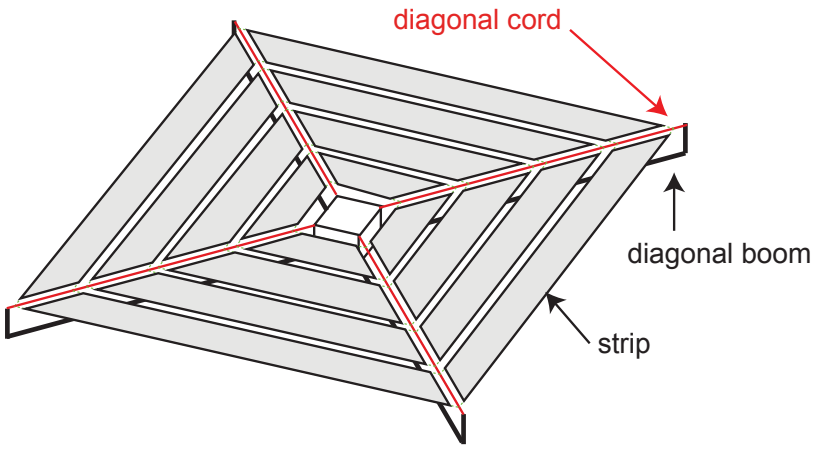

Figure 1.3: Schematic of a single SSPP spacecraft showing the structure and deployment mechanism in fully deployed configuration.

The deployment mechanism consists of a central hub, four diagonal booms and diagonal cords. Four cylinders hinged to the central hub keep the folded structure from deploying. When the cylinders are released, the structures starts to unfold due to its own stored strain energy while the four diagonal cords guide the structure towards the corners. In the fully deployed state, the cords are in tension and provide the needed support to the structure. This highly dynamic process (Figure 1.4) happens in less than two seconds.

This deployment involves a complex interplay of several dynamic factors. The geometry of the structure, rotation speed of the deploying cylinders, tension in the diagonal cords, gravity, and interactions among the strips are all critical components that affect the success of the deployment.

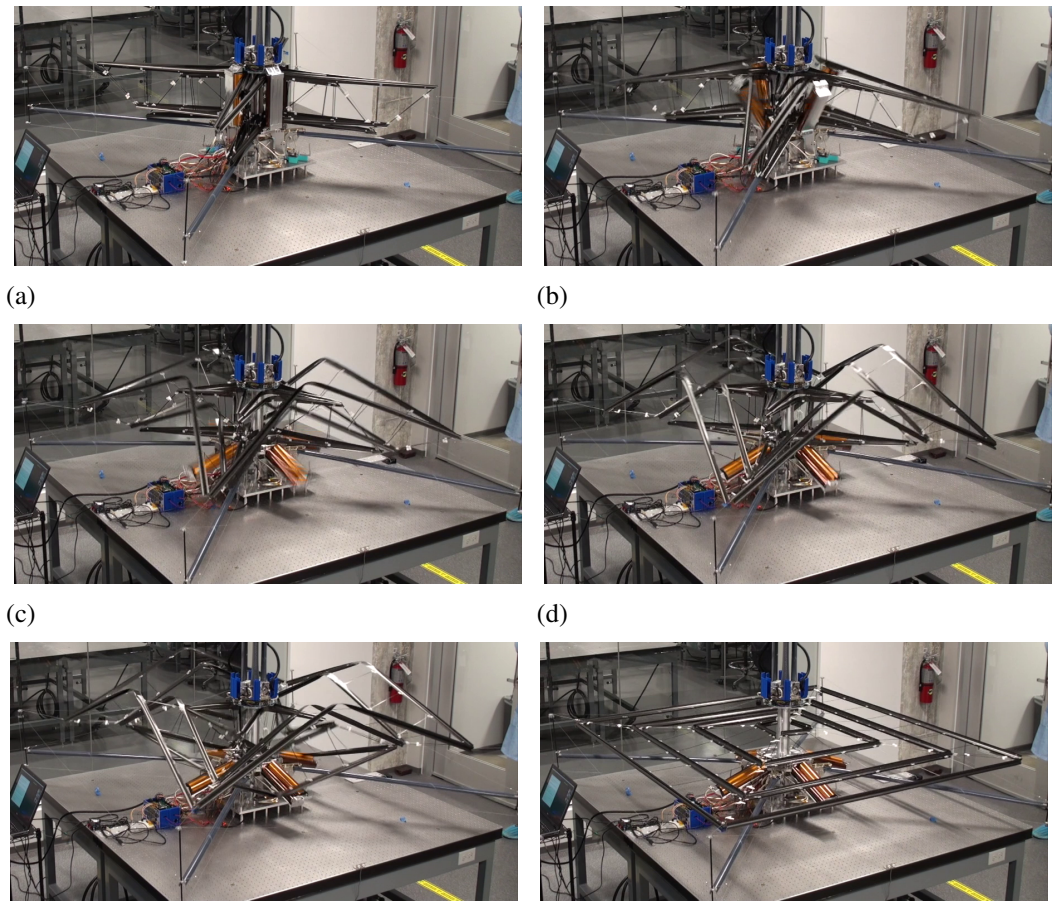

(a) (b)

(c) (d)

(e) (f)

Figure 1.4: Deployment of a Caltech SSPP structure with three strips in each quadrant. (a) is the folded configuration and (f) is the deployed configuration.

Measurement techniques

The deployment (shown in Figure 1.4) is dynamic. There are numerous structural elements to track and observe. The point cloud data from the deployment tests on the prototype (full structure with four quadrants; see [24, Chapter 4]) is too big and does not provide insight into the fundamental behavior of the deployment. Therefore, the deployment mechanism and the structure must be simplified.

To accurately observe and track the behavior of all the structural elements during deployment, it is important to utilize appropriate measurement techniques. Photogrammetry, a non-contact measurement method that uses cameras to record the motion of the structure, is a popular technique that has been used extensively in engineering and science fields.

One of the most common photogrammetry techniques used in this context is Digital

Image Correlation (DIC). DIC involves capturing a series of high-speed images of the structure during deployment and using image processing software to analyze the changes in shape and motion of the structure over time. The advantages of DIC include its high accuracy, non-invasiveness, and ability to capture detailed deformation information.

However, despite its accuracy, DIC has some limitations that make it less suitable for highly dynamic deployments. Capturing the entire SSPP structure using DIC requires a large field of view and larger speckles resulting in poor resolution. Furthermore, the large 3D translations and rotations of the strips during deployment make it difficult to track the speckle pattern, resulting in incomplete data [24, Chapter 4]. Moreover, DIC is sensitive to lighting conditions and the quality of the camera used, which can affect the accuracy of the measurements.

To overcome these limitations, another photogrammetry technique that can be used for dynamic deployments is motion capture, which involves using infrared cameras and reflective markers to track the motion of the structure. Motion capture has several advantages over DIC, including the ability to track non-uniform surfaces and to operate in a wider range of lighting conditions. Additionally, motion capture is highly accurate and can provide real-time data for monitoring the behavior of the structure during deployment. However, motion capture only tracks discrete points on the structure and provides a point cloud data. Shapes of the various components of the structure must be reconstructed or approximated from the available point clouds.

Numerical simulations

Numerical simulations are essential in the design and development of deployable space structures. They play a vital role in predicting the behavior of the structure during deployment and identifying potential deployment failures, which can be addressed before building the spacecraft. Additionally, numerical simulations can be used to study the impact of external influences such as the absence of gravity, which would be challenging or impossible to replicate in experimental testing.

In the existing literature, high-fidelity numerical simulations of thin-shell deployable structures have been limited to studying folding, coiling, or deployment of singular structures such as booms and hinges or systems with very minimal structural elements [7], [11], [25]–[28]. A fully functional numerical model for the dynamic deployment of a structure as complex as that used in the Caltech SSPP is

not yet available although a notable first attempt was recently made to simulate the deployment of the Caltech SSPP structure [24, Chapter 4].

This work aims to develop a high-fidelity numerical model to simulate the deployment dynamics of the Caltech SSPP and verify it against experiments. The challenges faced during such an undertaking are as follows.

1. Deployment of the mentioned structure happens in less than two seconds. Mass and inertia of the ultralight structure are very small compared to that of the mechanical components involved in deploying the structure. To model the deployment dynamics, behavior of all the involved components such as the material constitutive properties, behavior of cords and springs, friction in hinges and pulleys, contacts among surfaces and various geometric constraints must be accurately modelled.

2. The structure and the deployment mechanism consist of numerous structural elements to track and simulate. To simplify the analysis, both experimental and numerical, a simplified version must be chosen. However, this must not compromise the complexity of the original deployment dynamics and the knowledge gained using the simplified version must be readily transferable to the original deployment.

3. Employing a high-fidelity approach to model all components of the deployment mechanism poses significant computational costs. Therefore, it is essential to selectively model those components that directly impact boundary conditions or interact with the structure. However, a priori knowledge regarding these crucial components remains elusive, as does the identification of areas where appropriate approximations may be made. Precisely how much attention and accuracy must be devoted to modeling each component remains uncertain, resulting in a pressing need for extensive experimentation and observation to establish an effective approach for modeling these complex mechanisms.

4. To study the deployment of the structure from folded to unfolded states using numerical simulations, the folded state must first be accurately simulated. This is achieved by beginning the analysis with an unfolded, stress-free structure followed by simulating the folding process. The intermediate path taken from initial stress-free state to the folded state in non-unique. At the end of the

folding process, kinetic energy should be negligible. In addition, throughout the process, artificial energy should be negligible and total energy should be constant. One such appropriate folding technique is unknown a priori and arriving at one requires extensive trials.

5. To appropriately model the moving contact surfaces throughout the deployment, explicit dynamic solvers can be used. Explicit finite element analyses require extremely small time increments. Moreover, the accuracy of the results produced by explicit solvers must be rigorously validated, and this process can be time-consuming and require numerous trials to ensure the reliability of the simulation outcomes.

6. A very fine finite element mesh is required to model the TRAC longerons because of the long aspect ratios. Highly dense finite element mesh is often also required to accurately model the contact interactions between the structure and the rigid components of the deployment mechanism.

7. For the above two reasons, numerical simulation of a dynamic deployment of the structure requires days of computations making an already difficult process extremely time consuming.

1.3 Research objectives

The primary objective of this research is to demonstrate that the unconstrained dynamic deployment of thin-shell space structures can be rendered predictable through a comprehensive understanding of the deployment dynamics of the Caltech SSPP. The deployment process is influenced by the initial conditions and the interplay between the structure and the mechanism during deployment. To investigate these effects on the deployment process, high-fidelity numerical simulations will be developed and verified using experimental data. The research will address the following specific objectives.

- **Experiment benchmark and high-fidelity numerical simulations:** The deployment is highly dynamic and there are numerous structural elements to track and observe. The point cloud data from the deployment tests on the prototype (full structure with four quadrants; see [24, Chapter 4]) is too big and does not provide insight into the fundamental behavior of the deployment. Therefore, the deployment mechanism and the structure must be simplified. The simplified version must have only the necessary components needed for

deployment. To verify the numerical simulations, the motion of the structure during deployment will be reconstructed from the motion capture data.

To provide input to the numerical simulations, properties of all the involved components such as the material constitutive properties, tensile behavior of cords, stiffness of springs, friction in hinges and pulleys will be quantified through experiments.

- **Structure-mechanism interaction:** The structure is constrained by the cylinders in folded configuration (Figure 1.4). The deployment begins when the cylinders are released. The strips of the structure can unfold completely out of their own stored strain energy. However, the diagonal cords are needed to pull the strips to their desired final positions. In addition, the tensions in the cords stabilize the fully deployed structure. Although the cylinders do not have an intended role to play upon release, they do interact with the structure and act as obstacles in the path of the deploying structure. The slower the cylinders rotate, the longer they interact with the structure. In addition, a greater pulling force in the diagonal cords might increase the duration of this undesirable interaction. These two effects will be investigated and quantified to make the deployment predictable.

- **Sensitivity of deployment characteristics to design parameters:** Upon minimizing the structure-mechanism interaction, the dependence of the deployment to various design parameters and external influences will be investigated.

  While the Caltech SSPP structures are intended for space applications, thus far, the deployment tests have been performed on the ground and under the influence of gravity. Hence, it is essential to know how well on-the-ground deployment tests can predict the in-space deployment.

  As mentioned earlier, the Caltech SSPP structures would carry photovoltaic cells and functional elements to wirelessly transmit electricity to the Earth. Hence, the numerical simulations will be used to understand their effect.

  In addition, the sensitivity of the deployment characteristics to initial conditions such as initial orientation and locations of cord-structure intersections will be studied using numerical simulations.

- **Building larger SSPP structures:** Maximum length of the structure used in the current prototype and the flight model shown in Figure 1.4 is approximately

1.7 m owing to the limitations on the size of the autoclave used to manufacture the composite laminates. However, the next generation SSPP structures will be larger. Hence, an out-of-autoclave bonding technique to build a longer TRAC longeron from the shorter TRAC longerons cured in autoclave will be proposed. The robustness of the developed numerical simulations will be tested by simulating the deployment of a larger structure with four strips and verifying the result against experiments.

- **Reducing the computation cost in modeling folding of thin-shell structures:** The numerical simulations require a large number of degrees of freedom because of the long aspect ratios and localized instabilities that are typical of thin-shell deployable structures. For these reasons, numerical simulation of the dynamic deployment in the commercial software Abaqus[29] requires days of computations making an already difficult process extremely time consuming. Moreover, the next generation and significantly larger SSPP structures cannot be simulated at full scale using the current finite element techniques. Therefore, the total number of degrees of freedom used to model the structure must be reduced.

  For this purpose, the applicability of isogeometric analysis and h-adaptive finite element analysis will be investigated. As a test case, the widely studied problem of folding of a tape spring [30]—the simplest and most fundamental deployable structure—will be used.

1.4 Layout of the thesis

This thesis is organized as follows.

Chapter 2 focuses on designing a simplified version of the deployment mechanism and the deployable structure. One quadrant of the original SSPP structure is chosen as the test object. Various physical parameters involved in the mechanism such as friction in the hinge and pulleys, tensile behavior of cords, constitutive behavior of composite laminate are characterized experimentally. A new experimental technique to quantify the coefficient of friction in a pulley is proposed and implemented. The resulting numerical data is provided as input to the numerical simulations. For simplicity, hanging masses at the ends of the diagonal cords are used to drive the deployment of the structure. Movement of the structure is tracked using infrared motion capture cameras and the shapes of the individual strips are reconstructed from the point cloud data. Detailed steps to implement high-fidelity numerical

simulations of the deployment are presented. Results from the simulations are verified against the data from experiments.

Chapter 3 uses high-fidelity numerical simulations to study the sensitivity of the deployment to various influences such as the interaction between the mechanism and the structure; effects of gravity, constant deploying force in the cords, initial orientation of the structure, mass of the functional elements installed on the structure, constraints applied by the adjacent quadrants in a full structure, and the locations of the strip-cord connectors. This chapter presents a blue print to assist the design of the next generation SSPP structures and deployment mechanisms.

Chapter 4 discusses a technique to build larger SSPP structures and the deployment tests conducted to test the robustness of the technique. Efficiency of the numerical simulations is further tested by simulating the deployment of a four-strip SSPP structure and comparing with the experiment.

Chapter 5 investigates the efficiency of NURBS-based isogeometric analysis in reducing the computation cost of studying thin-shell deployable structures. Opposite-sense bending of a tape spring, the simplest and most fundamental deployable structure, is chosen as the test case. Bi-quadratic and bi-cubic NURBS elements, and traditional Lagrange finite shell elements available in the commercial finite element package LS-Dyna are used. The CPU times needed to achieve reasonably accurate solution using the elements of interest are compared. This chapter demonstrates that it is not yet worth switching to isogeometric analysis to study deployable structures.

Chapter 6 presents a brief literature review of adaptive finite element analysis and uncovers the need for further research in the area in relation to geometrically nonlinear analysis of deployable structures. Using the opposite-sense bending of a tape spring as an example, this chapter shows that the widely used error estimator based on energy norm and solution mapping procedure on recovered stresses fail in case of nonlinearity. In their places, strain energy based refinement indicator and a direct transfer of solution between the old and new integration points are proposed and their efficiency is demonstrated. A few mesh refinement techniques are investigated, and an improvement to an existing red-blue refinement strategy is proposed. This chapter demonstrates the applicability of h-adaptive meshing for nonlinear analysis of shells and provides a few tools to drive future research in this area.

Chapter 7 presents the conclusions of this research and directions for future research

in the area of numerical modeling of deployment dynamics and in the area of time-efficient finite elements for deployable shell structures.

Chapter 2

EXPERIMENTS AND NUMERICAL SIMULATIONS

Parts of this chapter were modified from the following publication.

N. H. Reddy and S. Pellegrino, "Dynamics of the Caltech SSPP deployable structures: Structure–mechanism interaction and deployment envelope," in *AIAA SciTech 2023 Forum*, 2023, p. 2065. DOI: 10.2514/6.2023-2065,

2.1 Introduction

Studies of the fundamentals of unconstrained deployment are relatively rare. In this chapter we attempt to fill this gap by explaining in detail the development of high-fidelity numerical simulations for this type of deployment. We will use the deployment of the Caltech Space Solar Power Project (SSPP) as an example, but the methods presented here can be used to study the dynamic deployment of many other thin-shell space structures outside of this project. The numerical simulations developed will be validated through experiments on a Caltech SSPP structure.

Figure 2.1 shows schematically the modular structural architecture adopted by the Caltech SSPP. It consists of bending-stiff trapezoidal strips bounded by foldable longerons with a TRAC cross-section [13] that are connected by battens. The strips form structurally independent modules and are attached to diagonal cords suspended between the tips of four diagonal booms and a central mechanism. Of the four identical quadrants in the full architecture, the present study focuses on a single quadrant to simplify the deployment and understand its fundamental behavior.

This chapter is organized as follows. Section 2.2 explains the experimental benchmark and the procedures used to quantify the various components involved. Specifically, the constitutive behavior of the composite laminate and the diagonal cords, and friction in the hinge and pulleys are quantified to provide input to the numerical simulations. To drive the deployment of the structure, weights are attached to the diagonal cords. Motion of the structure during deployment is tracked using infrared motion capture cameras. Section 2.4 explains, in detail, the steps involved in developing numerical simulations of folding and deployment. Section 2.5 presents the results from experiments and simulations, and compares the two. The comparison metrics used are the positions of the strip-cord connectors, fold angles in the two

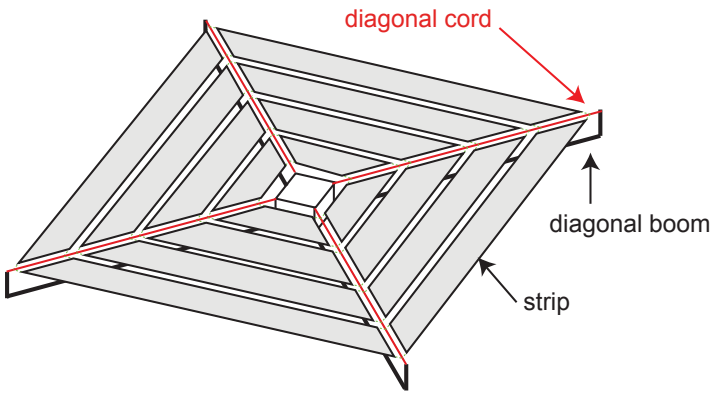

Figure 2.1: Full architecture of the Caltech SSPP.

outermost strips, and the time taken for all the longerons to latch into their flat states. The simulations are accepted if the individual errors in the comparison metrics are less than 10%.

2.2 Experimental setup

The only way to truly verify the fidelity of numerical simulations is to compare them with experiments. The composite structure of interest and the deployment mechanism that was designed to study its deployment are described below.

Structure

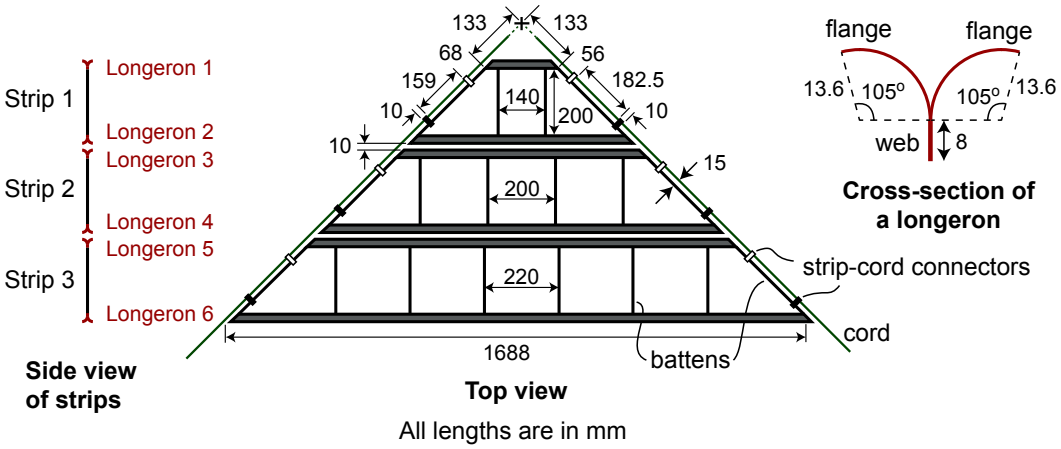

Figure 2.2: Geometry of structure.

The composite structure used in this study comprises three strips (Figure 2.2). Each strip consists of two bending-stiff longerons of TRAC cross-section ([13]). The composite layup in the flanges of a TRAC longeron is $[\pm 45_{GFPW}/0_{CF}/\pm 45_{GFPW}]$,

and that in the web region is $[\pm 45_{GFPW}/0_{CF}/\pm 45_{3,GFPW}/0_{CF}/\pm 45_{GFPW}]$, where CF represents a thin ply with unidirectional Pyrofil MR 70 12P Carbon fibers made by Mitsubishi Chemical (30 gsm). GFPW represents plain weave scrim glass (25 gsm). Both plies are impregnated with North Thin Ply Technology's ThinPreg 415 resin. The longerons are fabricated in-house using the techniques laid out in [18]. A strip is made torsion-stiff by connecting its two longerons at specific locations by carbon fiber rods called battens. The battens, made of carbon fibers, have a rectangular cross-section with a width of 3 mm and thickness 0.6 mm. Placement of the battens in a strip and the placement of strips in relation to one another was adopted from [21]. The battens are bonded to the web regions of the longerons with epoxy.

The three strips are connected via cords. To support a strip with the cord, two 3D printed sleeves called strip-cord connectors are rigidly bonded to the leftmost and rightmost battens (Figure 2.2). The cord is bonded, using epoxy, to the outermost strip-cord connectors of every strip. These connectors are shown in black in Figure 2.2.

Table 2.1: Mass properties of the composite structure.

Areal density of flange	1.196×10^{-4} g/mm^2
Areal density of web	2.908×10^{-4} g/mm^2
Density of batten	1.61×10^{-3} g/mm^3
Total mass of 6 longerons	45.4 g
Total mass of 18 battens	12.4 g
Total mass of 12 strip-cord connectors	7.5 g

The deployment mechanism

Inspired by the designs described in [21], [28], we designed a simplified deployment mechanism that incorporates only the essential components to trigger the release of the structure and study its deployment, but does not provide other key functions of the full flight mechanism. Also, instead of using constant-force retractors attached to the ends of the diagonal cords, for the purpose of verifying the numerical simulations, hanging masses were used in our experiments. The masses can be more easily tailored in the experiment, and are easier to quantify compared to other sources of deployment force such as retractor springs.

The deployment mechanism depicted in Figure 2.3 is built around a rigid cylinder labeled central shaft. Two annular plates made of acrylic are placed at the top and bottom of this shaft to mimic the mechanism in [21], [28]. The central shaft

supports the quick release mechanism at the very top, and is connected to the hinge and diagonal frames at the bottom. One end of each of the two cords is rigidly attached to the central shaft. The metallic frames placed along the diagonals of the quadrant support pulleys mounted on vertical columns at the outer ends (Figure 2.3). The central shaft, deploying cylinder, and the hinge components are made of aluminum while the top and bottom plates are made of acrylic.

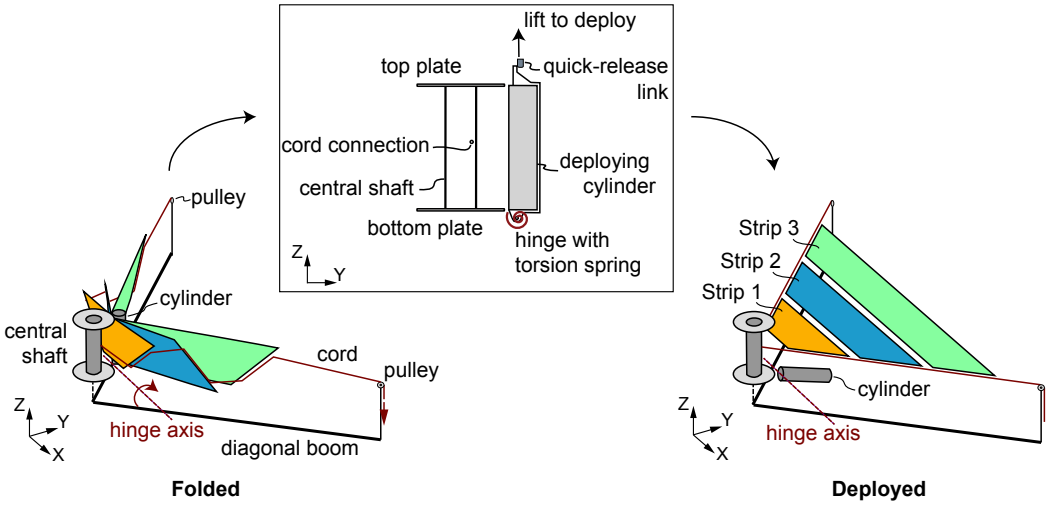

Figure 2.3: Deployment mechanism and structure in folded and deployed configurations, along with a schematic of the cylinder and hinge assembly. Strip 1 of the structure is shown in orange, Strip 2 in blue, and Strip 3 in green.

Motion capture

In order to verify the numerical simulations of the deployment, the motion of the structure was recorded using six infrared motion capture cameras, set a frame rate of 180 fps, marketed as *Prime 41* by *NaturalPoint Inc*. These cameras track the reflective markers attached to the structure at chosen locations. Flat reflective stickers were attached at all the longeron-batten intersections. A reflective sticker was placed also on the webs of the longerons, in the middle of two longeron-batten intersections. These flat markers include discs of diameter 7.5 mm and squares of each edge length 12.7 mm. In addition, to track the motion of the strip-cord connectors, reflective spheres 6.4 mm in diameter were glued to them. These passive markers reflect infrared (IR) light emitted from the camera and are subsequently detected by the camera's sensor. The captured reflections are then utilized to determine the 2D position of the markers. The software associated with the cameras: *Motive* leverages this information to calculate the corresponding 3D positions through reconstruction.

Calibration of the motion capture setup was performed before each experiment following the instructions laid out by the manufacturer [32]. The process of calibration is crucial in ensuring the optimal performance of optical motion capture systems. By performing calibration, the system calculates the precise position, orientation, and image distortions for each camera. These measurements are then utilized to construct a three-dimensional capture volume in Motive software. This construction involves the examination of synchronized 2D images from multiple cameras and the correlation of known calibration markers' positions through triangulation.

Before each experiment, the calibration was performed multiple times until the resulting mean 3D reprojection error was below 0.25 mm. For example, the mean 3D error over the six cameras in the motion capture of the deployment tests mentioned in Figure 2.12 was 0.184 mm. This error can be considered negligible with respect to the size of the structure. For example, the smallest length of Longeron 1 of the structure is approximately 184 mm (1000 times the mean 3D error) and the smallest distance between any two reflective markers on the structure is 27 mm (147 times the mean 3D error).

Measurement errors can arise also from the size of the reflective markers. A marker with a finite size is tracked as a single point with coordinates at the center of the visible portion. Consequently, the precise position of the point changes based on the visibility of the marker.

2.3 Characterization of composite laminates and deployment mechanism

To develop high-fidelity simulations of the dynamic deployment, it is essential to quantify the constitutive behavior of the composites, tensile behavior of the cords, and friction in the hinge and pulleys. The quantities measured will be used in the dynamic simulations presented in Section 2.4.

Material properties

The elastic stiffness of the flange and web laminates (Figure 2.2) was modeled with the generalized stiffness matrices $\boldsymbol{A}, \boldsymbol{D}$ for symmetric laminates [33],

$$\begin{Bmatrix} \boldsymbol{N} \\ \boldsymbol{M} \end{Bmatrix} = \begin{bmatrix} \boldsymbol{A} & \boldsymbol{0} \\ \boldsymbol{0} & \boldsymbol{D} \end{bmatrix} \begin{Bmatrix} \boldsymbol{\epsilon} \\ \boldsymbol{\kappa} \end{Bmatrix}, \tag{2.1}$$

where $\boldsymbol{N}$ and $\boldsymbol{M}$ are the in-plane forces and out-of-plane moments per unit length, $\boldsymbol{\epsilon}$ and $\boldsymbol{\kappa}$ are the mid-plane strains and curvatures, respectively; $\boldsymbol{A}$ is the in-plane

stiffness matrix, and $\boldsymbol{D}$ is the bending stiffness matrix.

To fold a longeron, the flanges are first flattened inducing a bending strain in the transverse direction (along the circumference of the circular arc, direction 2) followed by bending the flanges and web in longitudinal direction (direction 1). Hence, the elements of the stiffness matrices $\boldsymbol{D}$ contributing significantly to the stored strain energy due to bending are D_{11}^{web}, D_{11}^{flange} and D_{22}^{flange}.

We conducted four-point bending tests on the flange and web laminates to experimentally measure the stiffness values D_{11} and D_{22}, and tensile tests in longitudinal direction to measure the compliance values a_{11} and a_{21}, where the compliance matrix $\boldsymbol{a} = \boldsymbol{A}^{-1}$. The missing elements of $\boldsymbol{D}$ and $\boldsymbol{a}$ for both flange and web laminates were taken from an earlier study [18] conducted on similar laminates. The non-zero stiffness values used in the numerical simulations are listed in Table 2.2.

Table 2.2: Generalized stiffness values for flange and web laminates.

	Flange	Web
A_{11}(N/mm)	6218.5	11476.1
A_{12}(N/mm)	637.38	1112.8
A_{22}(N/mm)	1078.55	2291.54
A_{33}(N/mm)	736.5	1727.4
D_{11}(Nmm)	0.76	39.61
D_{12}(Nmm)	0.48	4.32
D_{22}(Nmm)	0.59	10.42
D_{33}(Nmm)	0.46	4.93

Behavior of the cord

Cords are the primary members carrying the deploying force in addition to holding various strips of the structure together (Figures 2.2 and 2.3). Knowing the tensile behavior of the cord helps accurately estimate the transfer of forces along the cord in numerical simulations. In addition, deformed lengths of the various segments of a cord decide the positions of the strips in relation to one another (see Figure 2.13).

Cords used in this study are 8 strand weave fishing lines with a load rating of 50 lb, marketed as *J-Braid* by *Daiwa*. To measure the elastic behavior (reaction force vs extension) of these cords, we conducted tensile tests on a sample using Instron machine. Extension was measured using two laser extensometers (LE-01 and LE-05 from Electronics Instrument Research), and the reaction force in the cord was measured using a 500 N load cell. The resulting data (Figure 2.4) was given as a direct input (in the form of a table) to the simulations.

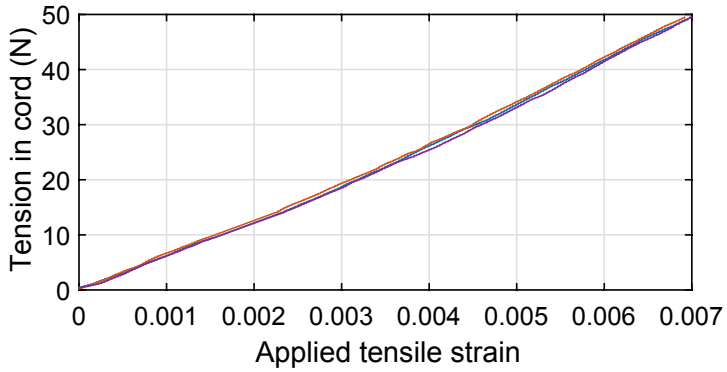

Figure 2.4: Response of the cord to applied tensile strain. Measurements from three repetitions of the tensile test are presented.

Characterization of the hinge

Deployment of the structure begins the instant the deploying cylinder is released. Initial dynamics of the structure depends on the rotational speed of the cylinder. This speed in turn is governed by the stiffness of the torsion springs and friction in the hinge (see Figure 2.3). Therefore, quantifying the elastic and friction contributions to the moment at the hinge axis is essential to accurately simulate the initial dynamics of the deployment. Elastic stiffness of the torsion springs was obtained from the data sheets, and was verified experimentally. To measure the friction moment at the hinge axis, we released only the cylinder, without any structure, and tracked its motion using motion capture cameras (Figure 2.5(a)). The measured rotation of the cylinder as a function of time, $\theta_{exp}(t)$, will be used in the following analysis to obtain a constant value for friction moment in the hinge.

The equation of motion of the cylinder at a rotation angle θ is

$$Mgd\sin(\theta+\theta_0)+T_e-T_f=I_h\ddot{\theta}, \tag{2.2}$$

with the initial conditions

$$\theta(0)=0 \quad \text{and} \quad \dot{\theta}=0, \tag{2.3}$$

where M is the measured mass of the cylinder, g is the acceleration due to gravity, T_e is the elastic moment due to the torsion spring in the hinge, T_f is the opposing friction moment, I_h is the rotational moment of inertia about the hinge axis, d is the distance of the center of gravity from the hinge axis, θ_0 is the angular position of center of gravity from the hinge axis with respect to the longer edge of the cylinder.

Mass of the cylinder was measured as $M = 885$ g. The location of the center of gravity of the cylinder ($d = 171.2$ mm and $\theta_0 = 9.14^o$) was obtained from the CAD model and was verified with experiments. Moment of inertia $I_h = 38.25\times10^{-3}$ kgm^2 was obtained from the CAD model.

The hinge has two torsion springs with measured stiffness of 54.1 Nmm/rad each. Since each spring was pre-compressed by 180°, the elastic moment is given by

$$T_e = 108.2(\pi - \theta) \text{ Nmm.} \tag{2.4}$$

The equation of motion 2.2 has two unknowns, constant T_f and $\theta(t)$, and needs to be solved iteratively. For a given value of friction moment T_f, Equation 2.2 can be integrated numerically to obtain the rotation as a function of time, $\theta_{an}(t)$. The value of T_f that minimizes the difference between the experimental measurement and the analytical result,

$$J = \text{norm}\left(\theta_{exp} - \theta_{an}\right), \tag{2.5}$$

was searched for using the unconstrained optimization solver `fminunc` in MATLAB.

The aforementioned experiment was repeated four times and four corresponding values for friction moment were obtained. The average value $T_f = 137.9$ Nmm was used in the numerical simulations that follow.

Coefficient of friction of the pulleys

Deployment of the cord ends is driven by gravity. The deploying force is carried by the cords which go over pulleys. Due to friction in a pulley, the tension force available to deploy the structure is smaller than the force applied at the loose end of a cord.

The miniature pulleys made of acrylic are mounted over ball bearings and are of diameter 12.7 mm each. We aim to approximate the friction moment in this assembly as a linear function of the total radial force acting on it. This linear behavior will then be simulated using *hinge* connector element in Abaqus [29]. The linear proportionality constant is the kinetic coefficient of friction.

Total radial force on the pulley supporting a cord is the vector addition of the tension forces in the two segments of the cord. The tension forces can be generated by attaching the ends of the cord to known masses. In a dynamic experiment, the

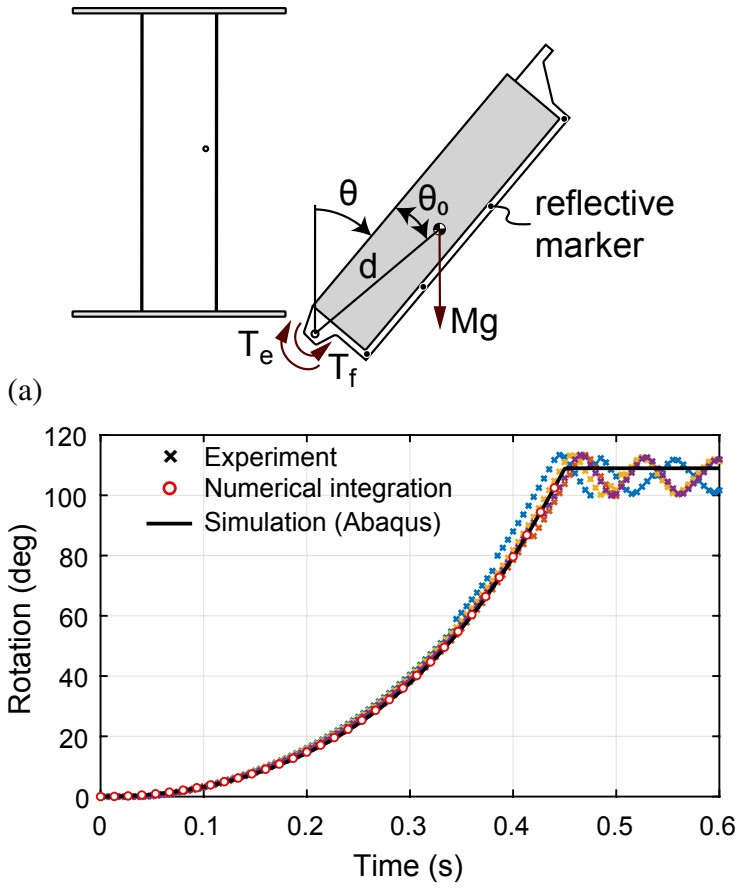

Figure 2.5: Estimating the friction moment in the cylinder hinge. (a) Schematic of the experiment. Cylinder is deployed without the structure. (b) Rotation of the cylinder with time. Friction moment T_f = 137.9 Nmm was used for the curves from numerical integration and Abaqus simulation. Cylinder locks at a rotation of 109^o in the simulation.

tension forces can be calculated from the known weights and measured motion of the masses. Due to the small size of the pulley, to avoid clashing between the two masses, our experimental setup utilizes two identical pulleys at the same horizontal level (Figure 2.6). The cord (of the same material used in the deployment experiments) running over the two pulleys is connected to two masses. When released, the heavier mass moves downward and the lighter mass upward. The reflective spheres attached to two masses were tracked using the motion capture cameras at a speed of 200 fps.

Applying Newton's second law of motion at masses M_1 and M_2,

$$T_1 = M_1(g + \ddot{h}), \tag{2.6}$$

$$T_2 = M_2(g - \ddot{h}), \tag{2.7}$$

where T_1 and T_2 are the tension forces in the cord at M_1 and M_2, respectively, g is the acceleration due to gravity, and $\ddot{h}$ is the acceleration of the masses.

The equations of rotational motion of the two pulleys are

$$TR - T_1R - M_{f1} = I\ddot{\beta}, \tag{2.8}$$

$$T_2R - TR - M_{f2} = I\ddot{\beta}, \tag{2.9}$$

where T is the tension in the portion of the cord between the two pulleys, R and I are the radius and moment of inertia of the pulleys, respectively, M_{f1} and M_{f2} are the friction moments in the left and right pulleys, respectively. When there is no slip between the cord and a pulley, rotation $\beta = h/R$.

The vertical displacement h of the masses we measured is a quadratic function of time, so the acceleration $\ddot{h}$ is a constant and is known. Therefore, tension forces T_1 and T_2 in Equation 2.6 are known. The moment of inertia I of the pulley was previously measured in [24] to be 1.9×10^{-8} kgm^2. To solve the three unknowns T, M_{f1}, and M_{f2} in Equation 2.8, we used the optimization solver `fmincon` in MATLAB.

Assuming that the friction moment in a pulley is directly proportional to the total radial force at the pulley bearing,

$$M_{f1} = \mu_1 r F_{n1}, \tag{2.10}$$

$$M_{f2} = \mu_2 r F_{n2}, \tag{2.11}$$

where μ_1 and μ_2 are the coefficients of friction in the pulleys, $r = 1.59$ mm is the radius of the bore, and F_{n1} and F_{n2} are the total reaction forces at the pulleys.

The force resultants on the pulleys are

$$F_{n1} = \sqrt{T_1^2 + T^2}, \tag{2.12}$$

$$F_{n2} = \sqrt{T_2^2 + T^2}. \tag{2.13}$$

This experiment was conducted with 21 different combinations of masses (Figure 2.7) with 2 to 4 repetitions for each combination. Using linear fits, the coefficients of friction were found to be 0.0323 and 0.0326 for the two pulleys.

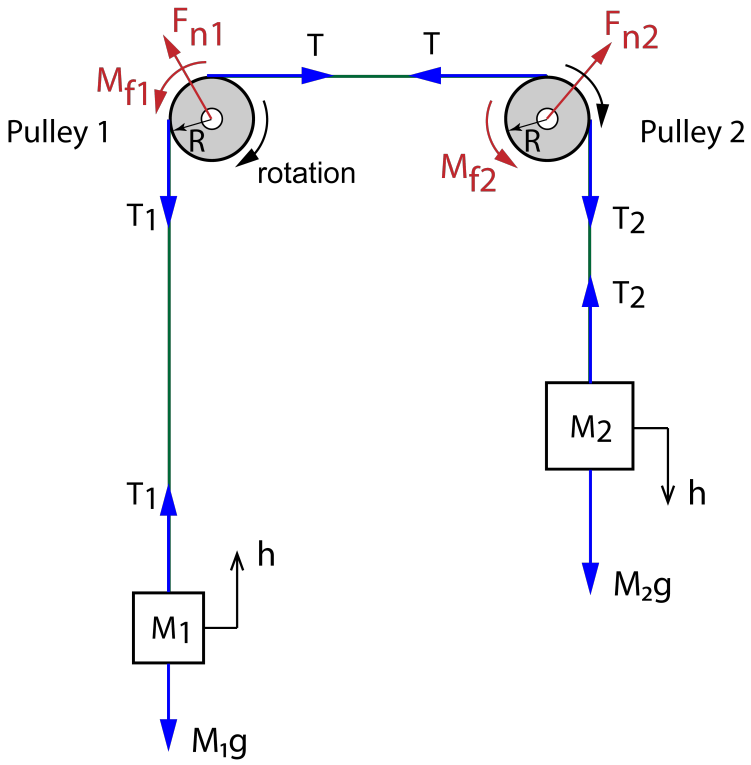

Figure 2.6: Schematic of the experiment to measure the friction coefficients of the pulleys.

2.4 Numerical simulations

Using the data presented in Section 2.3 for the composite laminates and the components of the deployment mechanism, we implemented explicit dynamic simulations in the commercial finite element package Abaqus, version 2020 using the Dynamic/Explicit solver.

Since the deployment tests were performed in air, air damping was approximated in simulations as a stagnation pressure with coefficient 1.41 kg/m^3 as proposed in [24, Chapter 2]. However, air effects are expected to be negligible on the current structure as observed in [24] for a similar structure.

To simulate the deployment of the structure, the initial condition is its folded configuration at rest (zero kinetic energy) which is unknown. Therefore, a first, key step of the analysis is to determine the folded configuration, starting from the known geometry of the unfolded structure. The exact path taken to achieve the folded configuration is unimportant as long as the total energy is conserved and the kinetic energy is negligible at the end of the folding process. In the experiments, each longeron has maximum one fold, mid-way along the length. Therefore, at the end

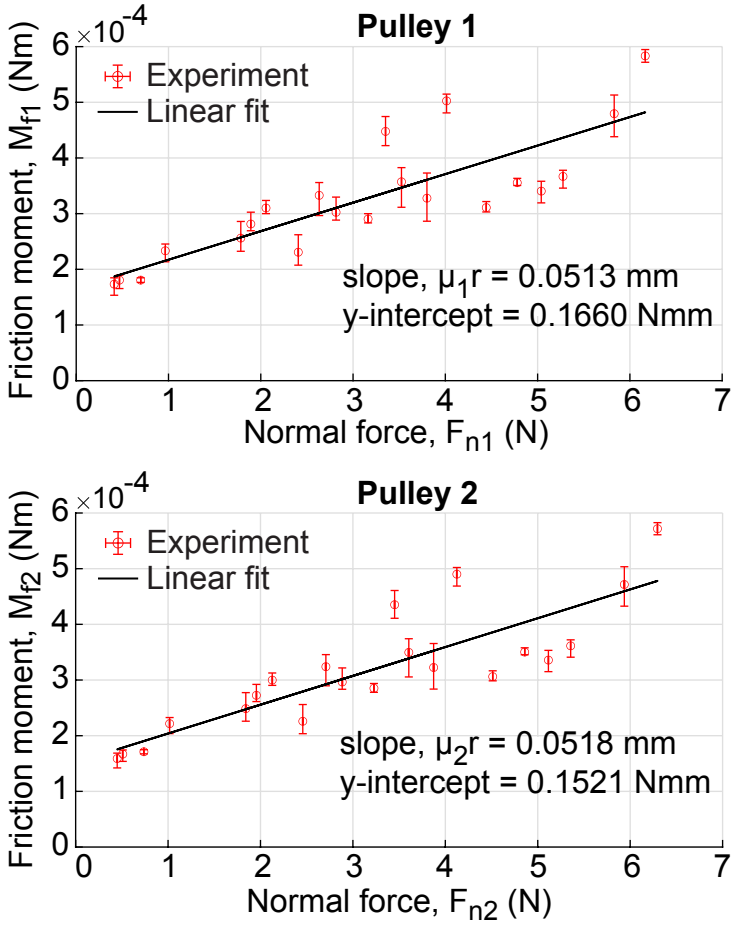

Figure 2.7: Friction moments in the pulleys in relation to the total radial forces acting at the centers. In pulley 1, coefficient of friction, $\mu_1 = 0.0322$, and in pulley 2, $\mu_2 = 0.0326$. The mean value $\overline{\mu} = 0.0324$ is used in the finite element analyses.

of the folding process in the simulations, the structure was visually inspected to make sure that it has the same number of folds and that there are no local buckles away from the expected folds. In addition, the folded configuration in the simulation was quantitatively verified by comparing the coordinates of all the strip-cord connectors and the fold angles in the longerons with those from the experiments. The deviations in these quantities from the simulations relative to those from the corresponding experiments were restricted to less than 5%.

The procedure used to simulate the folding process in this study is summarized below.

1. We began the analysis with a Z-folded structure with all the longerons, battens, and cords in their unstressed states (Figure 2.8).

2. To induce elastic folds in the TRAC longerons, the flanges were flattened by pinching the longerons. To pinch a longeron, a small pressure normal to the surface of each flange was applied over a length of 25 mm in the middle of the longeron.

3. All the longerons were then folded by applying vertical displacements to the ends of the suspension cords (regions of the cords between pulleys and hanging masses) as shown in Figure 2.8. During this, the tensions in the suspension cords were linearly ramped up to their intended value F or when hanging masses were used to drive deployment, gravity was linearly ramped up to its final value.

4. The displacement boundary conditions at the tips of the suspension cords were released and the structure was allowed to reach its natural folded state under the influence of the applied deploying forces. During this process, viscous damping pressure was applied over all the surfaces to dissipate the kinetic energy. It was linearly ramped up to its intended value, held constant for a certain duration, and linearly ramped back to zero.

The rigid components of the mechanism such as the semi-annular plate and the cylinder were modeled using quadrilateral shell elements R3D4. The mesh size for the cylinder was 2 mm. Interactions between surface pairs were modeled as frictionless, hard contact.

Modeling the deploying cylinder

The pre-compressed, elastic torsion spring used to deploy the cylinder, and the constant friction moment in the hinge were modeled in Abaqus using the connector element `hinge`. In the folded state, the rotation of the hinge connector about its axis was set equal to zero. This rotation constraint was deactivated at the beginning of the deployment step. The dynamics of the cylinder deployment, without the structure, was found to agree with that in experiments (Figure 2.5).

Modeling the strips

The composite laminates were modeled using quadrilateral shell elements with reduced integration, S4R. The flange and web sections of the longerons were modeled individually with the generalized stiffness values listed in Table 2.2. The mesh size for these elements was 2 mm, and the total number of such elements in the model was approximately 44000.

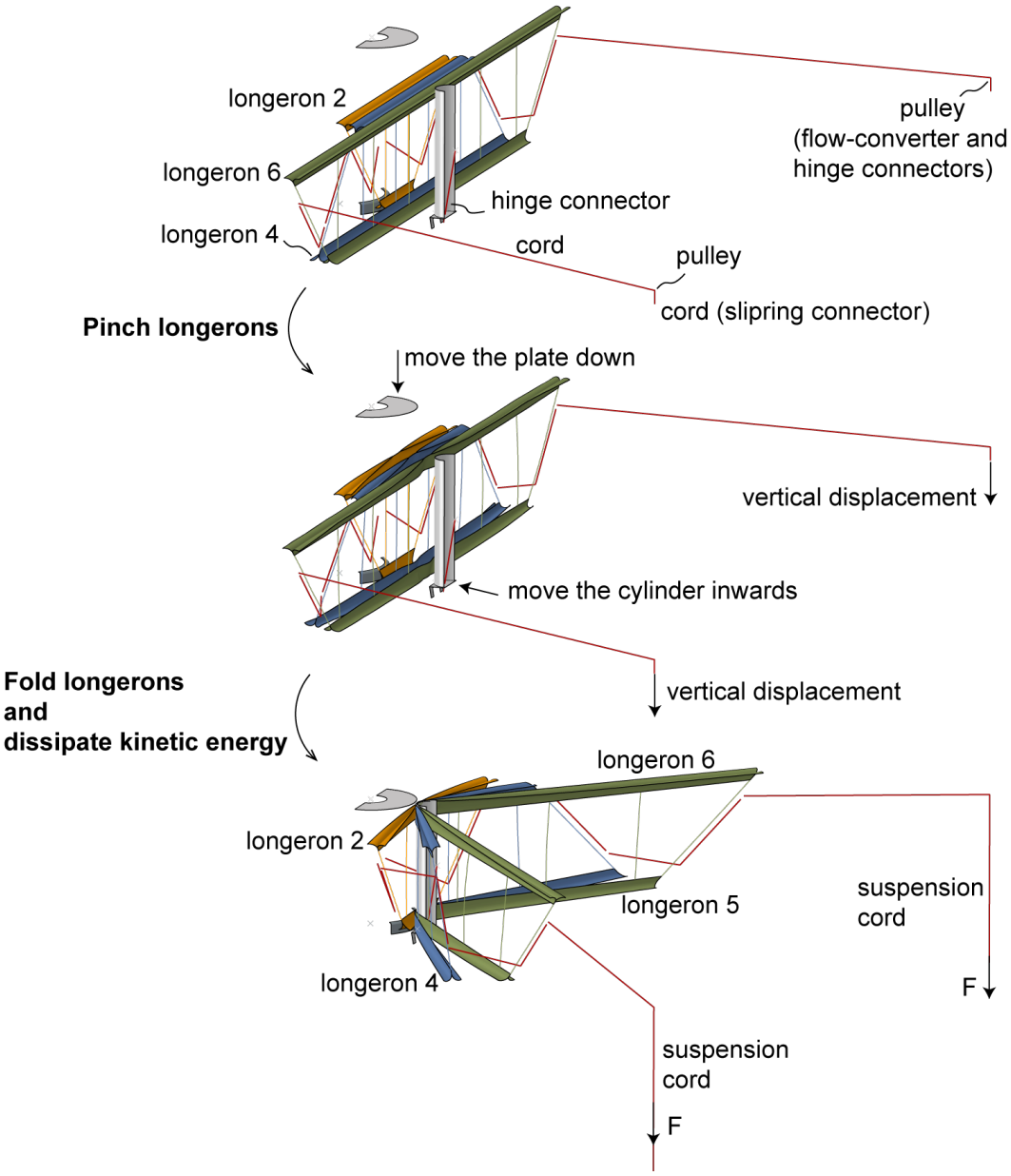

Figure 2.8: Illustration of the steps to achieve a folded configuration in the finite element simulations.

The battens were modeled as isotropic beams with Young's modulus of 137 GPa and Poisson ratio 0.3. Beam elements B31 each of length 4 mm were used for the finite element discretization.

The rigid connections between battens and longerons were modeled using kinematic coupling. The end of a batten was rigidly coupled to the nodes over a small region of the corresponding web laminate. This means that each degree of freedom was constrained to be equal at all the nodes involved in the coupling.

With the mentioned finite element mesh sizes, the stable time increment in the explicit analysis was approximately 7.4×10^{-8} s, and the critical elements deciding this time increment were the beam elements used to model the battens. To increase the stable increment of the analysis—to reduce the overall computation cost—a mass scaling can be applied to artificially raise the material density of a batten. However, it was observed that the deployment dynamics of the structure are highly sensitive to the mass of the structure. Therefore, no mass scaling was applied in any step of the analysis.

Modeling the cords

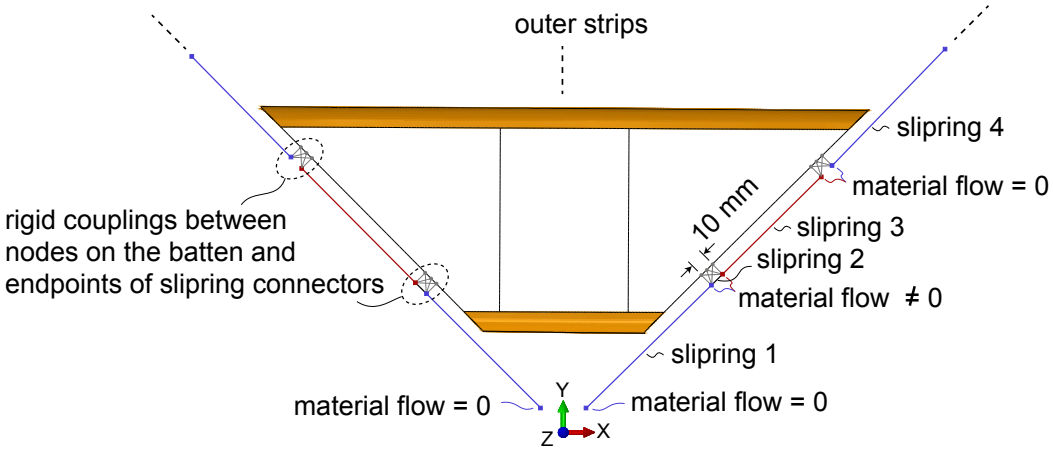

Figure 2.9: Cords were modeled using slipring connector elements in Abaqus.

As mentioned earlier, each of the two cords is fixed at one end to the central shaft, goes through six strip-cord connectors, goes over a pulley, and is connected to a force or a hanging weight (as in our experiment) at the other end. In the simulations, the cords were modeled with `slipring` connector elements. The elastic behavior observed in Figure 2.4 was provided as an input to these elements. A slipring element in Abaqus is defined as a straight line between two nodes. Each node has a *material flow* degree of freedom in addition to three translations. This degree of

freedom allows the flow of material between two adjacent elements (or two segments of a cord). Where the end of a cord is rigidly bonded to a batten or to the central shaft (Section 2.2), material flow was constrained to be zero (Figure 2.9).

To simulate a rigid strip-cord connector of finite width, two nodes were placed at a distance of 10 mm and were rigidly coupled (constraining all six degrees of freedom) to the nodes over the same span of the batten (Figure 2.9). These two nodes represent the two sides of the strip-cord connector that the cord goes through.

Modeling the pulleys

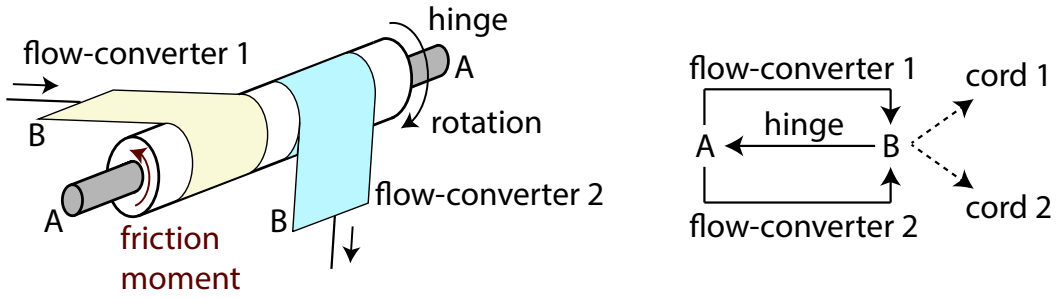

Figure 2.10: Modeling a pulley using flow-converter and hinge connector elements in Abaqus. Nodes A and B are coincident. Two segments of the cord are connected at node B.

Abaqus allows flow of material between two adjacent slipring elements at their common node. Such a joint is, by default, frictionless and a special arrangement was needed to model the friction moment in the pulleys (as described in Section 2.3).

The connector element `hinge` can model friction between two rotating surfaces. Specifically, the friction moment at the interface, about the axis of rotation, can be made to linearly vary with the total reaction force (see Figure 2.7 and Equation 2.10). To convert the material flow of the cord at one side into rotation of the hinge, and to convert the same rotation into material flow at the other side, two `flow-converter` elements were used. This conversion emulates a no-slip contact between the cord and the pulley. These three elements were defined between coincident nodes A and B as shown in Figure 2.10. The specific ordering of the nodes within a connector element, and the boundary conditions at the nodes were chosen based on the definition of these elements in Abaqus. The translation degrees of freedom at node A, and the rotation degrees of freedom at node B were set to zero. The two slipring elements modeling the two segments of the cord on either side of the pulley were connected at node B.

2.5 Results

Repeatability of experiments

The structure was deployed three times with 300 gram hanging masses and the deployment path was found to be repeatable. As an example, fold angles in the longerons of the outermost Strip 3 are shown in Figure 2.12.

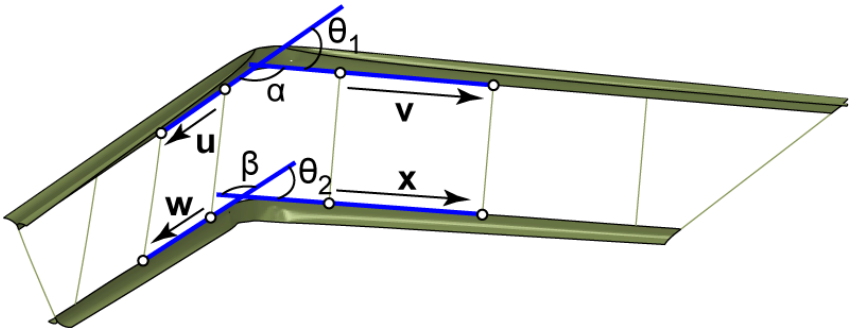

Figure 2.11: Estimating the fold angles from the positions of the reflective markers (shown as white dots). Fold angles θ_1 and θ_2 are obtained as $\pi - \alpha$ and $\pi - \beta$, where α and β are angles between the vectors $(\mathbf{u}, \mathbf{v})$, and $(\mathbf{w}, \mathbf{x})$, respectively.

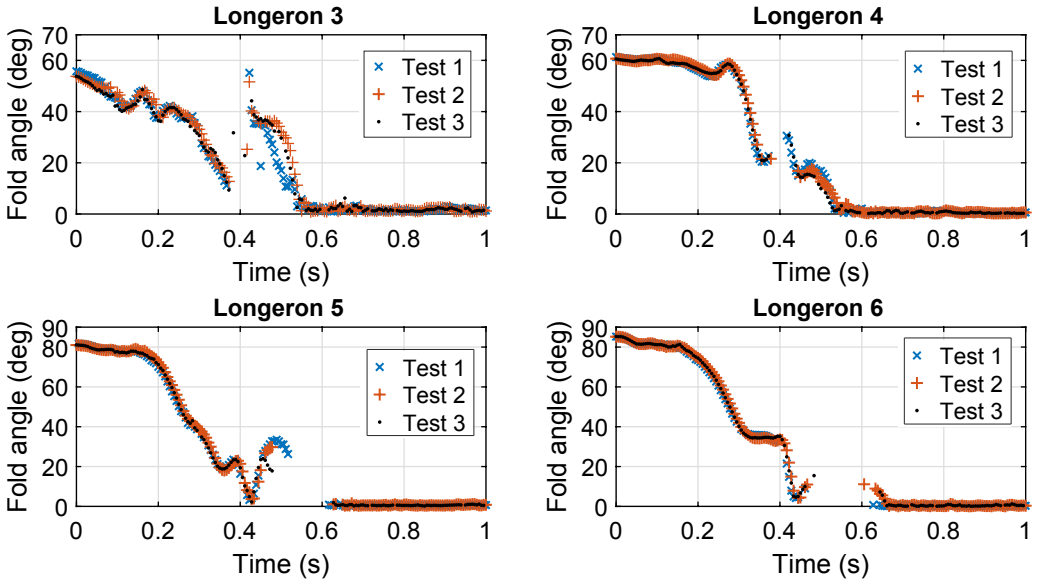

Figure 2.12: Fold angles in the longerons of Strips 2 and 3 from three repetitions of the deployment with 300 g hanging masses.

Explanation of the folded configuration

The folded configuration of the structure, prior to deployment, is shown in Figure 2.13. For a qualitative comparison, a top view of the folded structure from an experiment is provided. At a first glance, our simulations capture the folded configuration accurately. Quantitative comparisons are provided in the following sections.

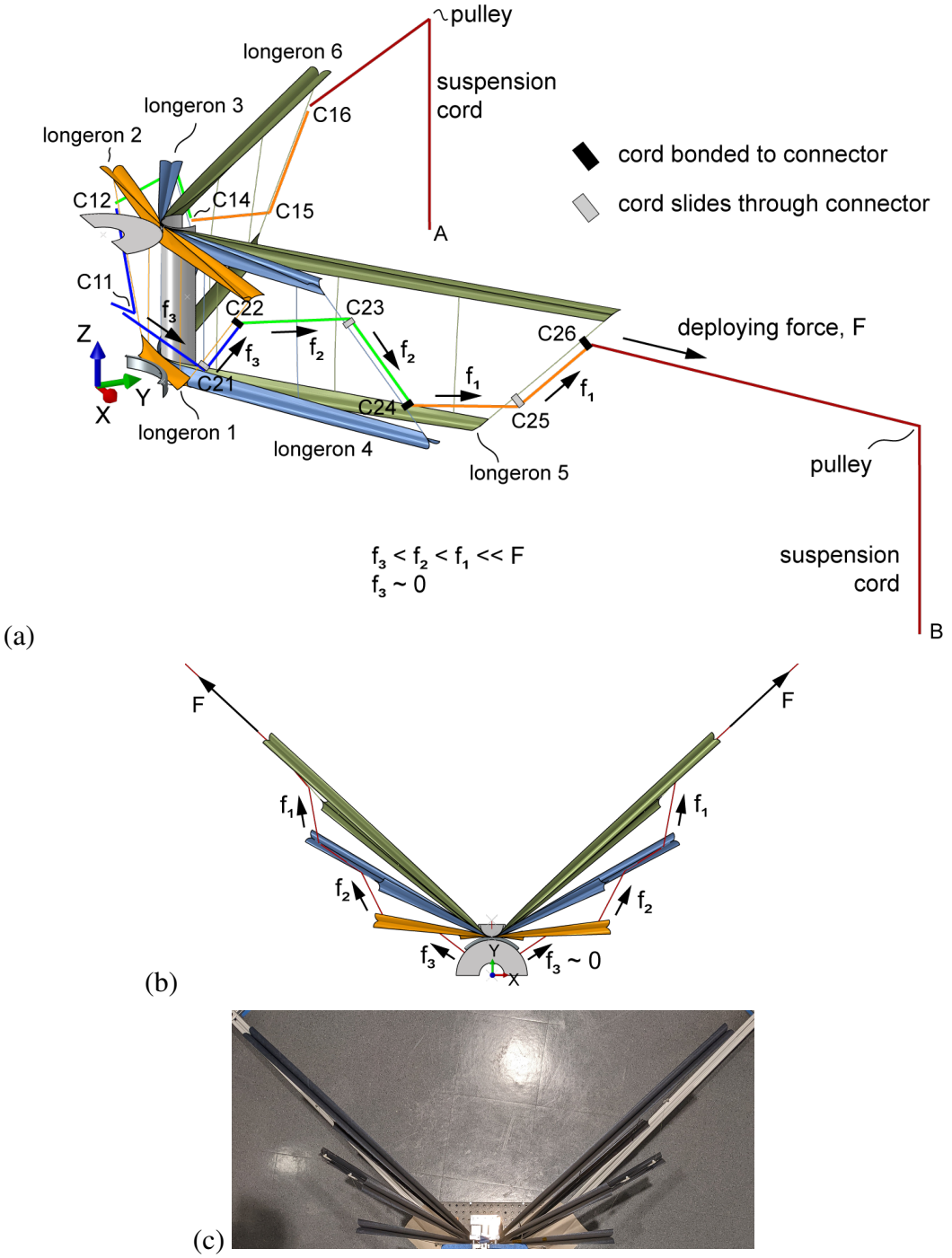

Figure 2.13: Structure in folded state: (a) perspective view and (b) top view in simulation, and (c) top view in an experiment. Cord is rigidly bonded to alternate strip-cord connectors hence the discontinuity in tension forces. Deploying force acts directly on the outermost strip. Fold angles in the inner strips are determined only by the unextended lengths of the cords. The innermost cords attached to the central shaft are slack.

The two cords holding the three strips together transmit the force that causes the deployment. Each cord is rigidly bonded to the strips at the outermost strip-cord connectors of every strip (shown in black in Figure 2.13(a)). This is done to ensure that the required length of the cord is available between a pair of strips to make the deployment possible. The required cord length is the length of the cord between the pair of strips in the fully deployed state (Figure 2.2).

The forces that cause deployment act directly upon the outermost strip-cord connectors C16 and C26 and are not transferred to the interior segments of the cords. Due to the elastic strain energy stored in the folded strips, a certain amount of force is required to prevent them from unfolding. This required force results from the tension forces in the interior segments of the cords. Therefore, the folded configuration of the interior strips (Strips 1 and 2) is dictated by the lengths of the cords between strips.

A longeron is said to have latched when it snaps back into its unfolded state i.e. when the fold angle first becomes approximately 0^o. The longerons (1 and 2) of the innermost Strip 1 are the least folded and are very close to their latched state. Hence the tension force required to keep the strip folded is very small compared to the applied force. When deployed, these longerons move almost straight along the $y-$ axis while the strip rotates about the $x-$ axis to reach its deployed state (Figure 2.14). The longerons (5 and 6) of the outermost Strip 3 are the most folded and follow more complex paths to reach their latched state. Upon deployment, the structure exhibits highly transient oscillations as seen at the end of every curve in Figure 2.14. While in experiments these oscillations are naturally dissipated and the structure comes to complete rest, the structure in the simulation continues to oscillate.

Energy history in simulation

The validity of the solution from an explicit finite element analysis must be established using the energy histories. As an example, Figure 2.15 shows the energy output by Abaqus for a simulation of the deployment with 300 g hanging masses.

The kinetic energy is negligible at the beginning of deployment as needed. Since the rotation of the cylinder was arrested at 109° (see Figure 2.5), the kinetic energy of the cylinder was removed out of the system and hence, the kinetic energy and the total energy dropped instantly (Figure 2.16(a)). This fall in total energy is equal to the amount of kinetic energy removed. Before this instant and after, the total energy remains constant. At the end of deployment, the kinetic energy becomes negligible

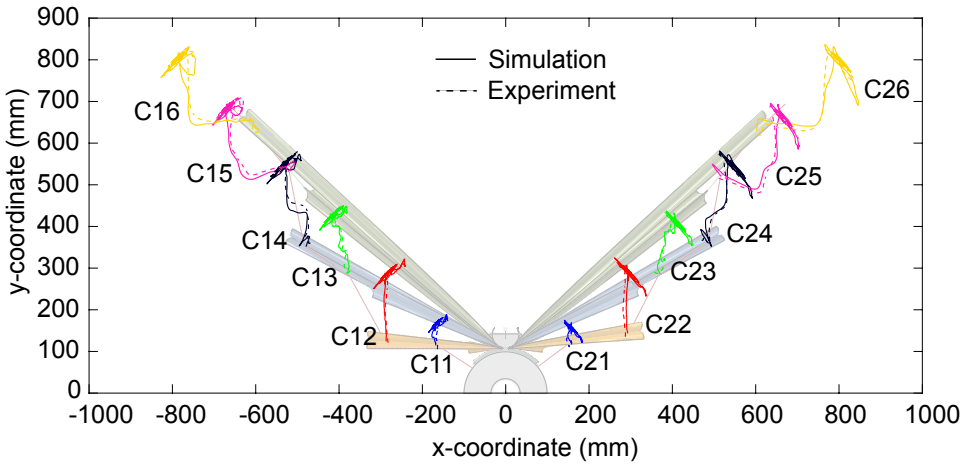

Figure 2.14: Simulation vs. experiment: comparison of the x and y coordinates of the strip-cord connectors (defined in Figure 2.13(a)) during the first 1 s of deployment. Hanging masses are 300 g. Top view of the folded structure is included in the background to assist the visualization.

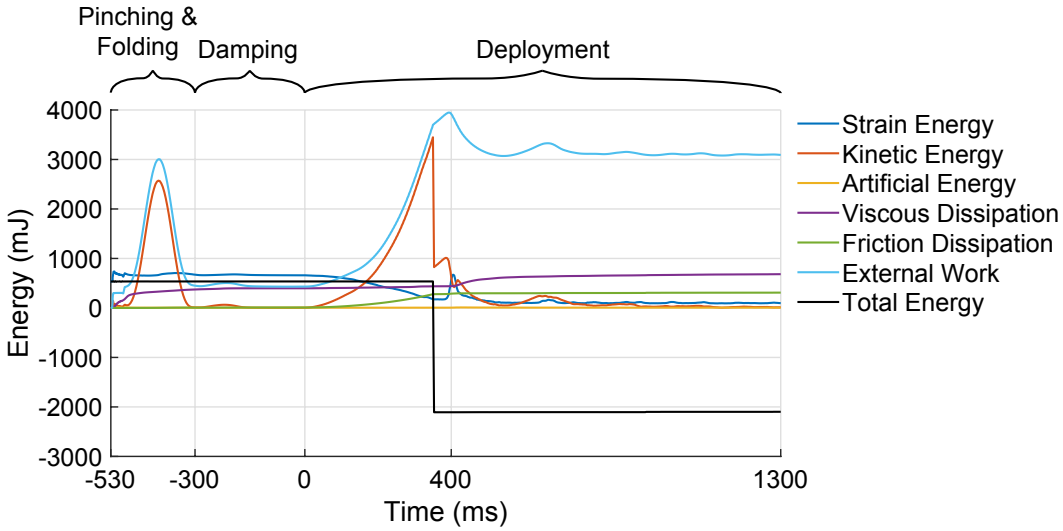

Figure 2.15: Evolution of the energies in the explicit finite element analysis of folding and deployment with hanging masses 300 g each. Deployment begins at time = 0.

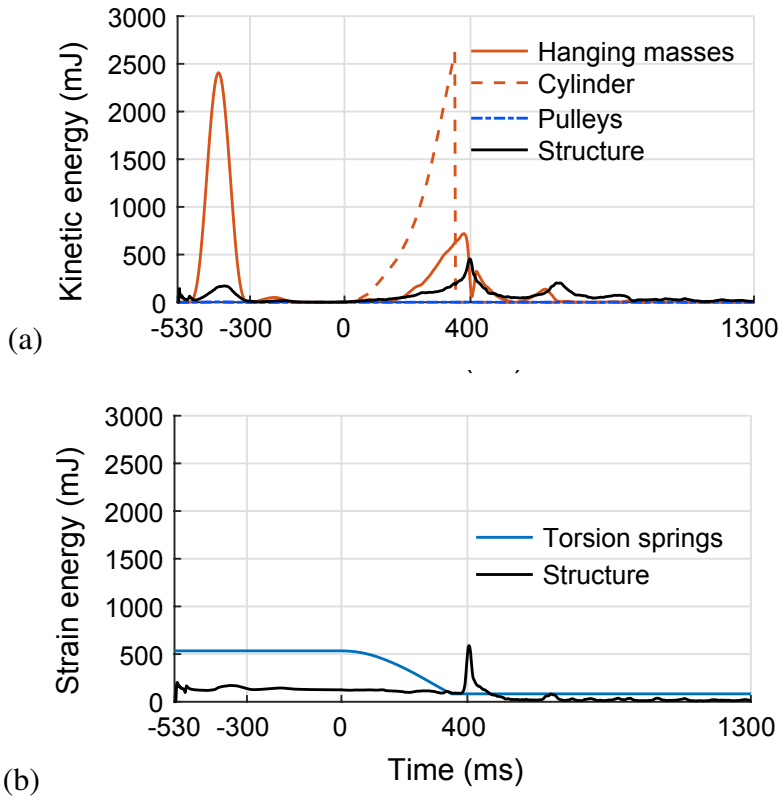

Figure 2.16: Contribution of the mechanism and the structure to the kinetic and strain energies. (a) Distribution of kinetic energy among the two hanging masses (300 g each), cylinder, two pulleys, and the structure. (b) Strain and kinetic energies of the structure. Deployment begins at time = 0. Hanging masses are 300 g.

as the structure gets close to its fully deployed state.

The total strain energy (in Figure 2.15) starts from a non-zero value as it includes the strain energy stored in the torsion springs (precompressed by 180°) in the cylinder hinge (Figure 2.16(b)). As mentioned in Section 2.5, the longerons were pinched over a duration of 30 ms to assist folding. This lead to a sharp rise in the strain energy of the structure (Figure 2.16(b)). The total strain energy remains constant throughout the damping step and starts to decrease when the cylinder is released. Towards the end of deployment, the strain energy reaches a non-zero steady state value equal to the strain energy remaining in the torsion springs that are still compressed by 81°.

The local maxima in total strain and kinetic energies after the cylinder is locked are due to the oscillation of the hanging masses as shown in Figures 2.16(a) and 2.17.

In addition, the artificial energy is less than 6.5% of total strain energy throughout the simulation.

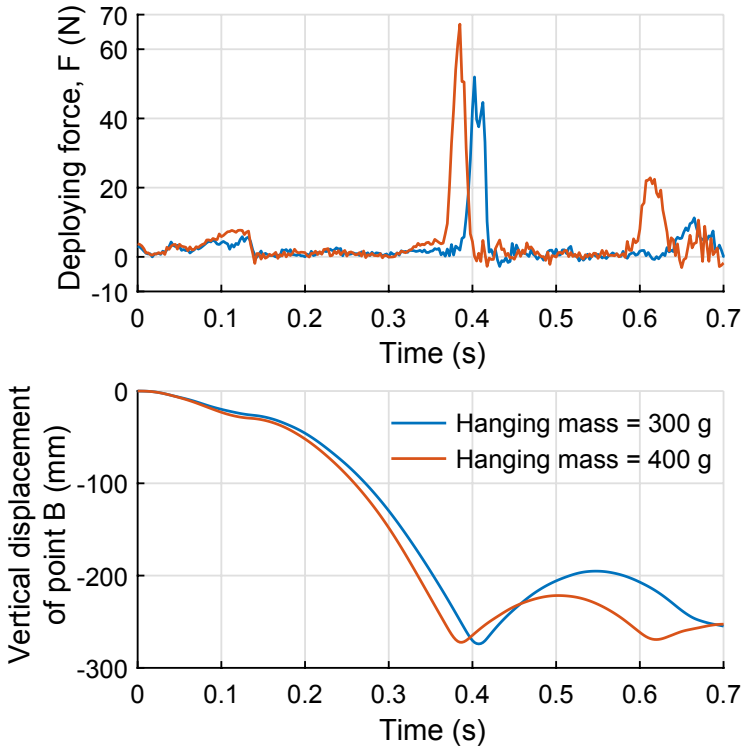

Figure 2.17: Effective deploying force in the suspension cord and vertical displacement of the hanging mass at point B. Tension in the cord rises suddenly at approximately 0.4 s due to the momentum of the hanging masses.

The only two sources of friction dissipation are the friction in the cylinder hinge and the friction in the pulleys (see Sections 2.3 and 2.3). The friction dissipation starts to rise at the start of deployment and remains almost constant after the cylinder is locked since the cylinder hinge contributes the most to the friction dissipation.

Experiment vs. simulation

Table 2.3: Percentage of absolute deviation from experiments in distances from origin of the strip-cord connectors before 0.4 s. Hanging masses are 300 g.

Location	Mean	Standard deviation	Maximum
C22	5.17	2.61	10.02
C24	0.95	0.56	2.30
C26	1.00	0.63	2.00

To compare the implemented numerical simulations with the experiments, we performed the deployment of the structure with two different hanging masses: 300 gram and 400 gram. Reflective markers on the structure were tracked using the infrared motion capture cameras mentioned in Section 2.2. Only the data from the first 0.4

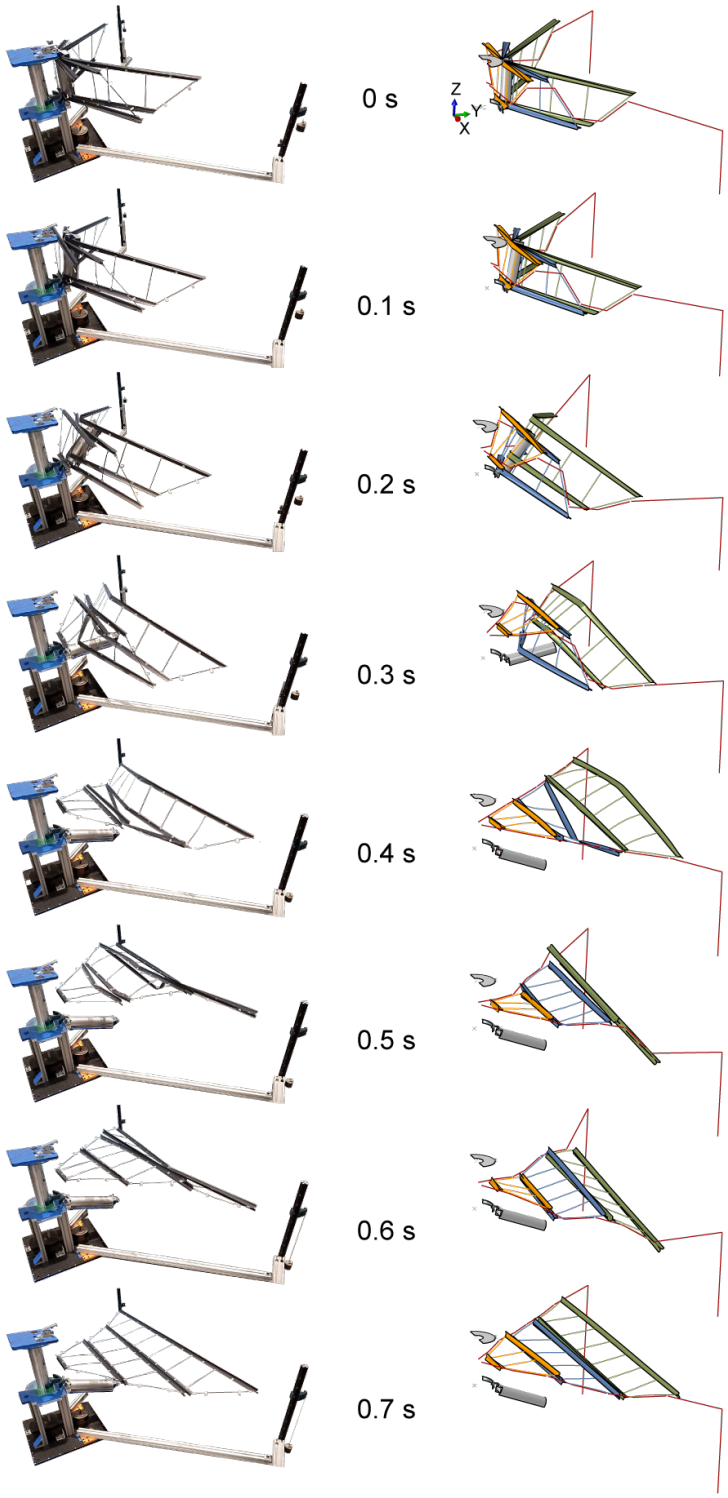

Figure 2.18: Qualitative comparison of the deformation profiles between experiment (left) and numerical simulation (right). Hanging masses are 300 g.

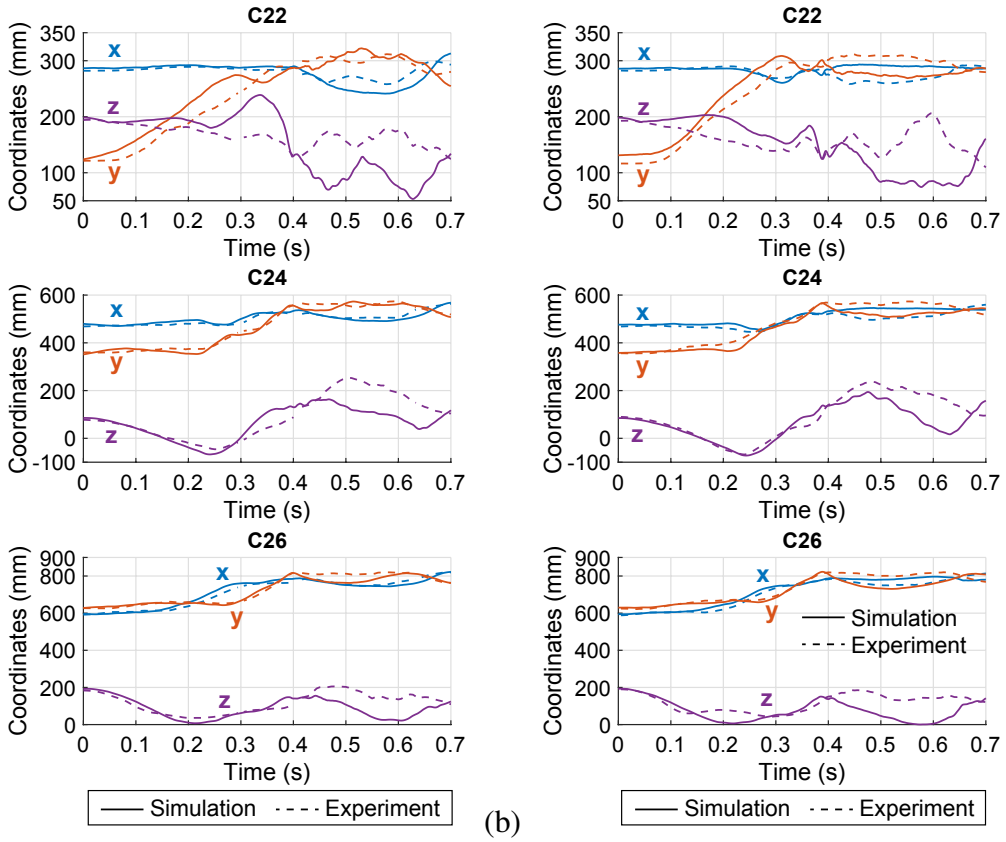

Figure 2.19: Simulation vs. experiment: comparison of the x, y, z coordinates of three strip-cord connectors (defined in Figure 2.13(a)) during the first 0.7 s of deployment. The hanging masses are 300 g in (a) and 400 g in (b).

Table 2.4: Percentage of absolute deviation from experiments in distances from origin of the strip-cord connectors before 0.4 s. Hanging masses are 400 g.

Location	Mean	Standard deviation	Maximum
C22	4.27	2.39	7.57
C24	0.75	0.42	1.41
C26	0.51	0.34	1.08

s of the deployment is considered for the comparisons. The hanging masses reach their lowest vertical positions at approximately 0.4 s. In other words, the structure reaches its maximum radial position at this instant. After this instant, deployment characteristics are dominated by the oscillations of the masses (and hence the oscillations in the structure). Moreover, the deployment mechanism offers structural damping which was not modeled in the simulations.

The outermost strip-cord connectors C16 and C26 (defined in Figure 2.13(a)) are directly driven by the hanging masses and their motion should be the easiest to predict, followed by the motion of the interior connectors. As an example, a comparison of the Cartesian coordinates of three strip-cord connectors is shown in Figure 2.19. The corresponding deviations in the absolute positions of the strip-cord connectors are presented in Tables 2.3 and 2.4. Position of a connector is the square root of the sum of squares of its x, y, and z coordinates.

Relative error is defined as the ratio of the absolute difference between the values from experiment and simulation to the value from experiment.

It can be seen that the initial positions (at 0 s) of the connectors in simulation are in excellent agreement with the experiment. The simulations estimate the motion of C26 with maximum error less than 2% until the hanging weights reach the bottom of their motion range (0.4 s). At this time, the tension forces in the suspension cords rise significantly for a short time duration to oppose the momentum of the weights. After this time, the x and y coordinates are estimated with better agreement with experiments than the vertical z coordinates.

Although in case of the innermost strip-cord connector C22, the simulations deviate further from the experiments (Figure 2.19), the mean deviation from experiments is less than approximately 5% in both cases (Tables 2.3 and 2.4). The maximum error in each case is less than 10% until the end of deployment.

Table 2.5: Percentage of absolute deviation from experiments in the fold angles before 0.4 s. Hanging masses are 300 g.

Longeron	Mean	Standard deviation	Maximum
3	2.85	2.23	7.31
4	2.29	1.38	5.63
5	2.79	2.07	8.29
6	3.49	2.93	9.92

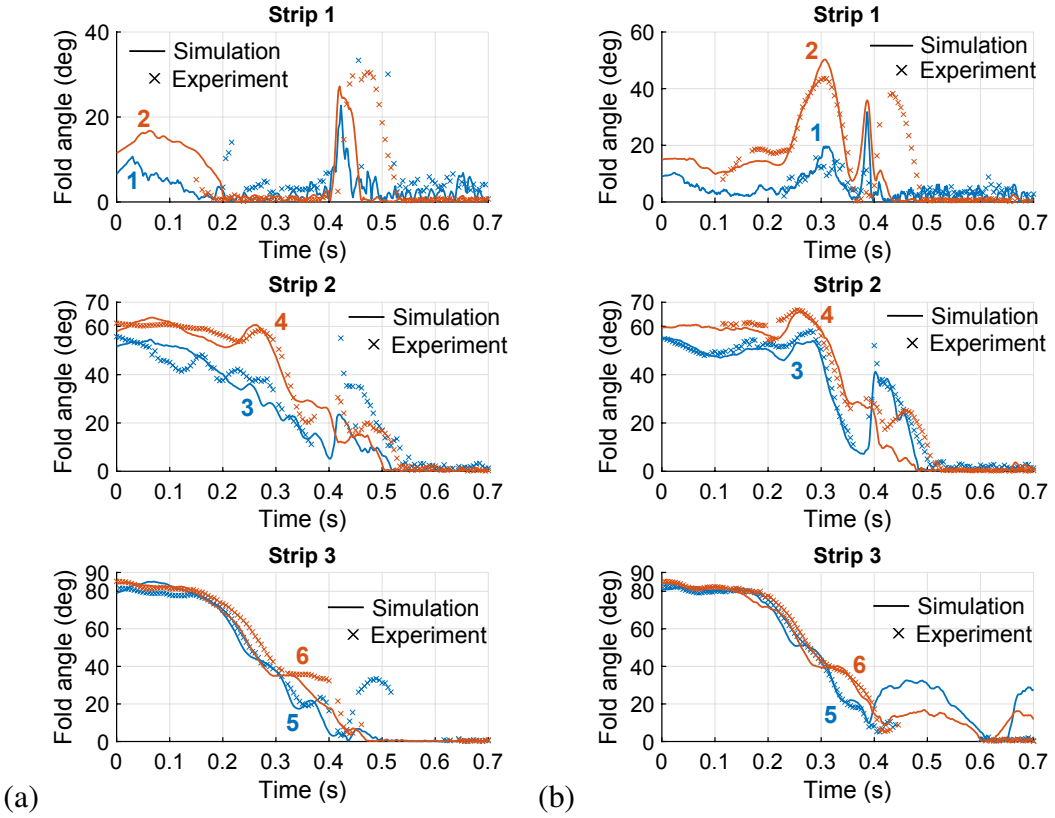

Figure 2.20: Simulation vs. experiment: comparison of the fold angles in the longerons. Longeron IDs as defined in Figure 2.2 are marked against the corresponding curves. Hanging masses are 300 g in (a), and 400 g in (b).

Table 2.6: Percentage of absolute deviation from experiments in the fold angles before 0.4 s. Hanging masses are 400 g.

Longeron	Mean	Standard deviation	Maximum
3	1.94	1.25	4.51
4	2.20	1.41	6.31
5	1.63	1.47	6.50
6	2.36	2.08	7.66

Going a step further in verifying the simulations, we compare the fold angles in all the longerons (Figure 2.20). It was observed in the experiments and simulations that the elastic folds remain in the middle of the longerons at least until the end of deployment or until the hanging masses reach their lowest positions (at approx. 0.4 s). Hence, two markers (in experiment) or two nodes (in simulation) at the longeron-batten intersections on either side of the middle of a longeron are used to define the fold angle (Figure 2.11). The two vectors connecting these two pairs of markers or nodes define the fold angle. In the few instances (after approx. 0.4 s of deployment) where the fold is not in the middle of a longeron or where there are multiple folds, the angle between the two vectors does not represent the true fold angles. However, the comparison is still valid since the parameter being compared is the same in both experiment and simulation.

Note that the experimental data for the fold angles of Longerons 5 and 6 is missing in between 0.4 s and 0.6 s of deployment time because of the rotation of Strip 3 away from the central shaft as shown in Figure 2.18. Because the six motion capture cameras used to track the reflective markers on the structure were placed behind as well as on either sides of the central shaft, the reflective markers on Strip 3 were not tracked by the cameras during the aforementioned time frame.

As explained in Section 2.5, the innermost smallest strip begins at fold angles closest to 0°. This is also the first strip to latch into the fully flat state during deployment (Figure 2.20). In the experiments, not all the reflective markers on the innermost strip are in the field of view of the motion capture cameras in the folded configuration. Since the locations of at least four markers on a longeron are needed to compute the fold angle, experimental data for the fold angles in the innermost Strip 1 is not available at the beginning of the deployment. Hence, the fold angles in the two outermost Strips 2 and 3 are considered for quantitative comparisons (Tables 2.5 and 2.6). The absolute deviation in fold angles from experiment is defined as $|\theta^{sim} - \theta^{exp}|/(\pi - \theta^{exp})$, where θ^{sim} and θ^{exp} are fold angles from simulation and experiment, respectively.

In both the cases (hanging masses 300 g or 400 g), among the four outermost longerons, the maximum deviations in fold angles are less than 10% with mean errors less than 3.5%.

The time for latching is defined as the time taken for all the longerons to first latch into their deployed configuration. The deployment times for the two test cases are listed in Table 2.7 and differ by approximately 10%.

Table 2.7: Simulation vs. experiment: comparison of time for latching.

Hanging masses	Simulation	Experiment
300 g	0.503 s	0.56 s
400 g	0.508 s	0.56 s

Although we expected that the deployment would be faster when hanging masses are increased, the results show practically no change. Although the initial dynamics of the deployment are different with different hanging masses, the time taken for all the longerons to latch into their unfolded state is almost identical. The key factor affecting this behavior is the effective deploying force, i.e., the tension in the suspension cord. Due to the inertia of the hanging masses, the tensions in the suspension cords are of comparable magnitudes and have similar time histories (Figure 2.17) before the masses reach their lowest vertical positions.

Furthermore, the tension forces in the diagonal cords rise significantly when the hanging masses reach their lowest vertical positions. The deployment dynamics from this instant are dominated by the oscillations of the masses and the structural damping provided by the mechanism. Hence, a comparison between the simulations and experiments was not viable after this instant. Using the hanging masses to guide the deployment is not ideal and the deployment tests will be conducted using constant force spring retractors for further comparisons in Chapter 4.

2.6 Conclusions

Unconstrained dynamic deployment of the ultralight deployable space structures developed by the Caltech Space Solar Power Project (SSPP) was studied using experiments and numerical simulations. For the purpose of verifying the numerical simulations, deployment tests of the structure triggered by hanging weights were conducted, and the motion of the structure was tracked using motion capture cameras.

To provide input to the numerical simulations, the components involved in the deployment mechanism were quantified using experiments. In the process, a novel technique to characterize friction in a pulley was designed and implemented. The numerical simulations of folding and deployment of the structure were implemented in the commercial finite element software Abaqus using the explicit solver. Before verifying with experiments, the finite element solutions were validated using the energy histories.

To metrics used to compare the simulations with experiments were the positions of the strip-cord connectors, fold angles in the two outer strips, and the time taken for the entire structure to latch into its flat state or the first instant where all the fold angles are 0°. In all the comparisons, the max deviation, over time, was less than approximately 10% with respect to the experiments. Therefore the developed simulation techniques are accepted and will be used to understand the structure-mechanism interaction and sensitivity of deployment to design parameters in the next chapter.

The numerical modeling techniques presented here will not only benefit the Caltech project but can also be applied to the design of future lightweight deployable space structures that undergo dynamic deployment.

Chapter 3

STRUCTURE-MECHANISM INTERACTION AND SENSITIVITY OF DEPLOYMENT TO DESIGN PARAMETERS

3.1 Introduction

The effectiveness of the numerical simulations in predicting the dynamic deployment of the thin-shell Caltech SSPP structures has been established in the previous chapter. In this chapter, we use the developed simulation techniques to understand the structure-mechanism interaction, and make the deployment predictable and robust. We will demonstrate that by tailoring the initial conditions, the desired deployment can be achieved. The deployment desired here is the one where each longeron has maximum one stationary elastic fold during the deployment. In addition, a deployment with smaller envelope or lower maximum heights is preferred.

Once the design is optimized to achieve the desired deployment behavior, we will investigate the sensitivity of the deployment to various design parameters. The outcomes can be used to improve the design of the current prototype as well as to assist the designs of the next generation SSPP structures and deployment mechanisms.

In the previous chapter, we used hanging masses to assist the deployment for the sole reason that the masses are easy to quantify and model in numerical simulations. However, the structure is intended for space applications and will be deployed using spring retractors in the absence of gravity forces. Therefore, in this chapter, we study deployment using constant force spring retractors. Schematic of the structure and deployment mechanism in stowed and deployed configurations is shown in Figure 3.1.

Figure 3.2 shows the model considered in the numerical simulations. The same thin-shell composite structure introduced in Chapter 4 will be studied (see Figure 3.4). The structure is made of three ladder-like components called strips. Each strip comprises of two composite longerons of TRAC cross-section. The three strips are connected by two cords at the strip-cord connectors (SCC for short).

To make the deployment possible, each cord is rigidly bonded to the strips only at half the number of SCCs. As shown in Figure 3.2, each cord is rigidly bonded to the outermost SCCs of every strip, i.e., SCCs closest to the even-numbered longeron of

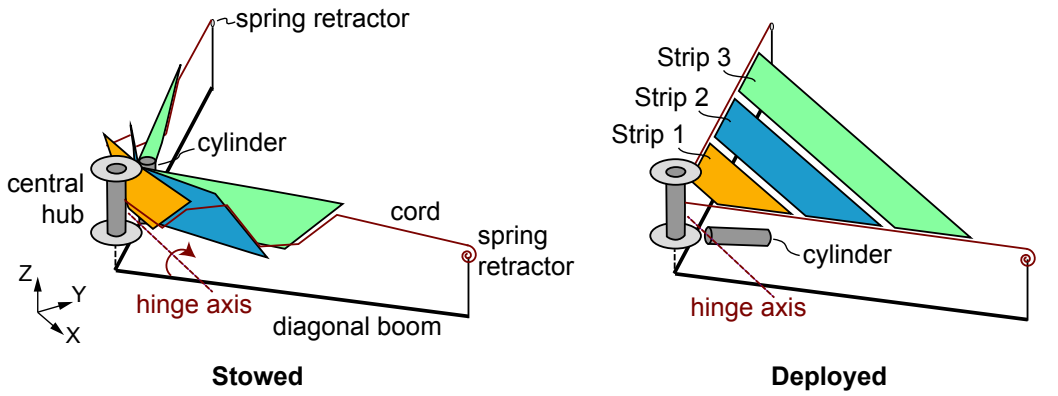

Figure 3.1: Schematic of the deployment mechanism and structure in folded and deployed configurations. Spring retractors at the ends of diagonal booms assist the deployment.

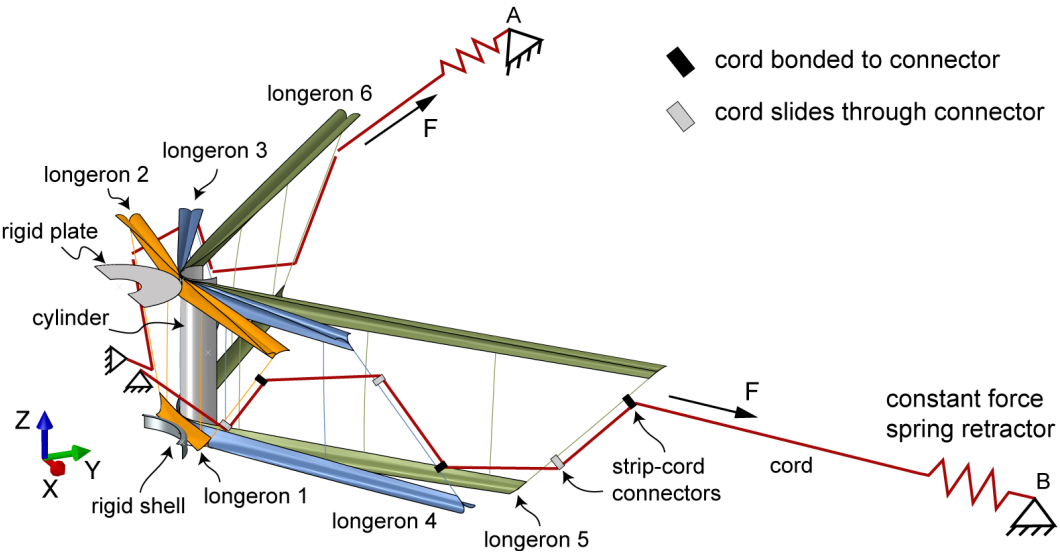

Figure 3.2: Model used in numerical simulations.

that strip. The cords can freely slide through the innermost connectors of each strip.

One end of each strip is fixed in space simulating the rigid connection to the central shaft depicted in Figure 3.3. The other end of the cord is connected to a constant force spring retractor.

In the numerical simulations, only those components of the deployment mechanism that are in contact with the folded structure or those that might come in contact with the deploying structure are modeled. Such components are the rigid plate, rigid shell, and cylinder shown in Figure 3.2.

The structure in folded configuration is sandwiched among the rigid components. The rigid shell at the bottom of the mechanism and a rectangular protrusion at the

tip the top plate (see Figure 3.3) assist in holding the folded structure in place as well as in ensuring the repeatability of the folded configuration. The cylinder when stowed prevents the structure from deploying.

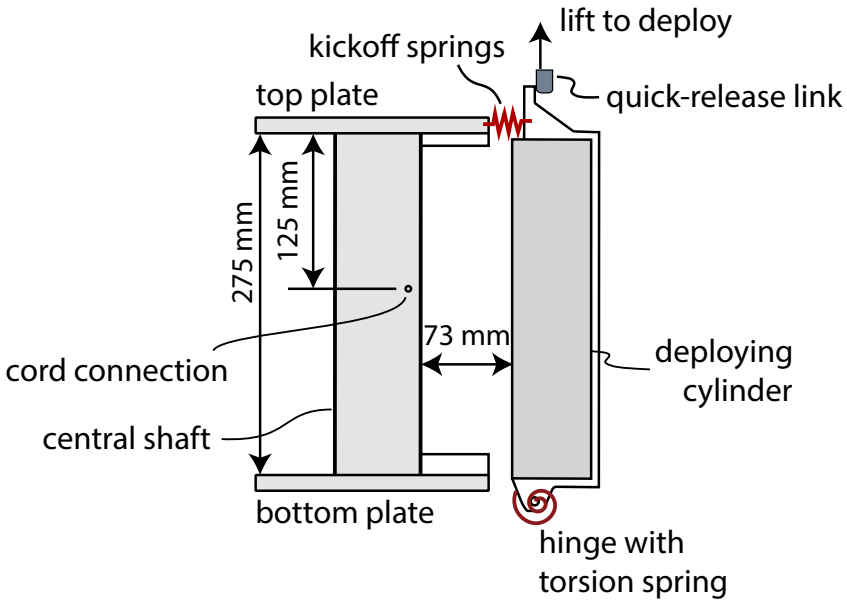

Figure 3.3: Schematic showing the center of the deployment mechanism. Two kickoff springs in parallel provide an impulse to the cylinder upon release.

The deployment of the structure is triggered by the release of the cylinder and is affected by the following.

1. **Gravity:** While the structure and deployment mechanism are designed for space applications, away from the influence of Earth's gravity, preliminary tests are conducted on the ground, i.e., in the presence of gravity. Hence, it is essential to know how reliable on-the-ground deployment tests are in gaining insights into in-space deployments.

2. **Spring retractors:** While the folded structure deploys and unfolds solely due to its own stored strain energy, the outer ends of the structure as guided by the constant force spring retractors. Hence, the stiffness of these springs or equivalently, retraction force offered by the spring retractors affects the dynamics of the deployment.

3. **Cylinder:** The cylinder, upon release, takes a finite time to reach its final state and interacts with the structure during deployment. While the spring

retractors assist the unfolding of the structure, the cylinder provides an obstacle to the deployment of the structure. The speed of rotation of the structure can be controlled through the choice of torsion springs at the hinge and kickoff springs at the top of the structure (Figure 3.3). Note that kickoff springs were utilized in the flight prototype of Caltech SSPP [21] to ensure separation between the central hub and the cylinder upon release. Here, the kickoff springs are intended to increase the rotation speed of the cylinder.

4. **Membrane and functional elements:** The structure is intended to host functional elements such as photovoltaic cells and RF antennas in space. These elements would be mounted on a Kapton membrane that fills all the gaps among the longerons and battens of every strip. The membrane would be rigidly bonded to a strip at the longeron-batten intersections [34]. Inertia of these components affects the deployment dynamics.

5. **Orientation of the structure in folded state:** Before installing the structure in the deployment mechanism, it is first Z-folded (alternating mountain and valley folds), inserted into the gap between the central shaft and the cylinder, and then the cords are attached to the central shaft and the retractors. Two orientations of the structure are possible (as shown in Figure 3.21) and will lead to different deployment paths.

6. **Locations of strip-cord connectors (SCC):** The placement of the SCCs affects the kinematics and dynamics of the deployment. It determines the locations of centers of mass of the strips, locations of application of retractor forces (through tensions in cords) on the strips, and the lengths of cord available between strips during deployment. Moreover, the locations of the SCCs are of particular interest since they are decided at the final stage of assembling the structure and can be altered without damaging the strips.

This chapter is dedicated to studying the effect of the above parameters on the deployment of the SSPP structures using numerical simulations. The structure used along with the approximation of the mass of membrane with functional elements (hereafter, simply referred to as membrane) is shown in Figure 3.4. While the mass of the membrane is approximated, the membrane itself is not modeled and neither are the resulting effects such as wrinkling and air drag.

In all the simulations presented in this chapter, the torsion spring stiffness is 100 Nmm/rad and the friction in the hinge of the cylinder is ignored (Figure 3.3).

To analyze the resulting deformation profiles from the numerical simulations quantitatively, the following quantities are used: radial motion of the structure R and rotation of a strip α as defined in Figure 3.5, fold angles in the longerons, and the maximum and minimum heights reached by the structure during deployment.

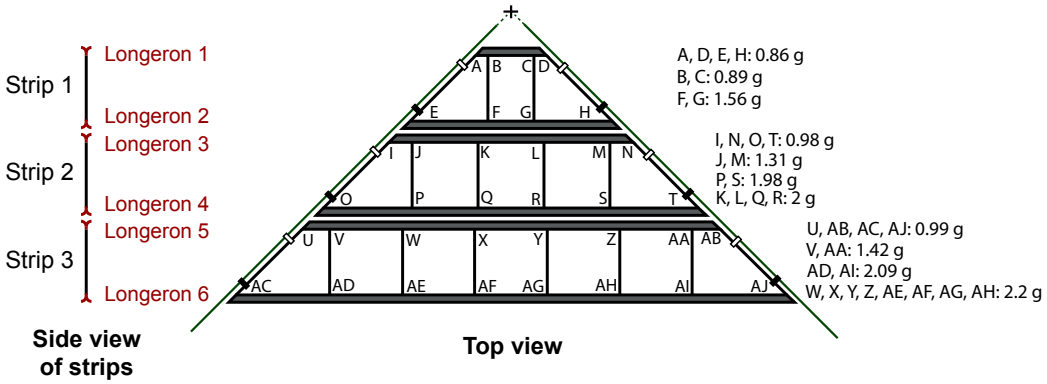

Figure 3.4: Schematic of the structure: Mass of membrane and functional elements is approximated by placing point masses at the intersections of longerons and battens. The values shown correspond to areal density of membrane $\rho = 100\ \mathrm{g/m^2}$. Mass of the structure was 65.3 gram. Total mass of the added point masses is 55.43 gram.

3.2 Effect of cylinder rotation

The deployment begins at the instant the cylinder is released by the quick-release mechanism. During the initial part of the deployment, the cylinder could interact with the structure and sometimes lead to undesirable effects. For example, it can be seen in Figure 3.8 that in the absence of kickoff springs ($K = 0$), the cylinder provides a ramp to the structure thereby raising the maximum height reached by the structure during deployment. An example of a more adverse effect is the deployment of the structure with constant force $F = 5$ N shown in Figure 3.14. The structure-cylinder interaction in this case lead to a chaotic behavior of the strips. Hence, it is essential to minimize this interaction between the structure and the mechanism.

In other words, the cylinder must be out of the way of the deploying structure as soon as possible. This can achieved by pushing the cylinder with a large force at the beginning of the deployment. Helical springs between the top plate and the cylinder fulfill this objective and hence are called kickoff springs (Figure 3.3).

The current model employs two kickoff springs of stiffness K each. Each of these springs is precompressed by 5 mm in the stowed configuration. The force applied by these springs on the cylinder linearly reduces to zero as the cylinder rotates by approximately 0.9°. from the stowed position. This short-lived kickoff spring force

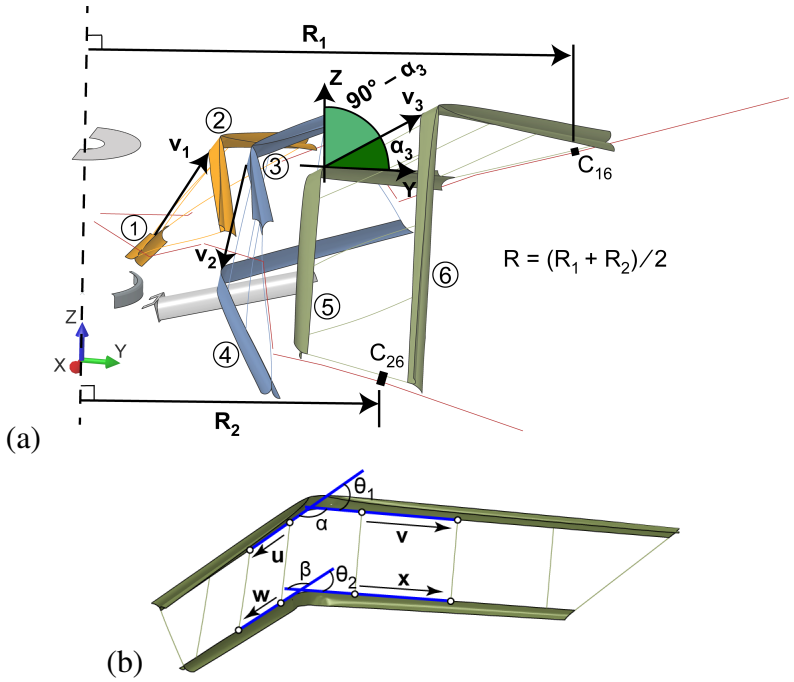

Figure 3.5: Definitions of (a) radial motion of the structure R and strip rotation α, and (b) fold angle in a longeron. R_1 and R_2 are the radial distances from Z-axis, on X-Y plane, of the outermost strip-cord connectors of the structure. Vector v_i in a strip i points from midpoint of the smallest longeron to the midpoint of the longest longeron of the strip. Fold angles $\theta_1 = \pi - \alpha$ and $\theta_2 = \pi - \beta$ are estimated from the positions of the reflective markers (shown as white dots). α and β are angles between the vectors $(\mathbf{u}, \mathbf{v})$, and $(\mathbf{w}, \mathbf{x})$, respectively.

can have a significant impact on the angular velocity of the cylinder. Figure 3.6 shows the impact of a few kickoff spring stiffnesses on the motion of the cylinder. For this comparison, only the cylinder was deployed, without a structure.

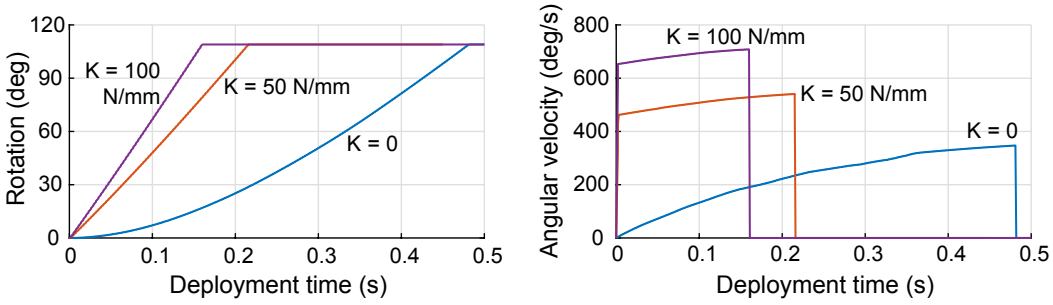

Figure 3.6: Effect of kickoff spring stiffness K on the rotation and angular velocity of the cylinder. Since two kickoff springs are used, total stiffness is $2K$. Cylinder locks at a rotation of 109° in the simulations.

The effect of the kickoff springs on the deployment of the structure is studied using

numerical simulations. The extreme cases of no kickoff spring or $K = 0$, and $K \to \infty$ where the cylinder reaches its final position instantaneously also were simulated. In all cases, the same retractor force $F = 2$ N and the same membrane density $\rho = 100$ g/m^2 were used.

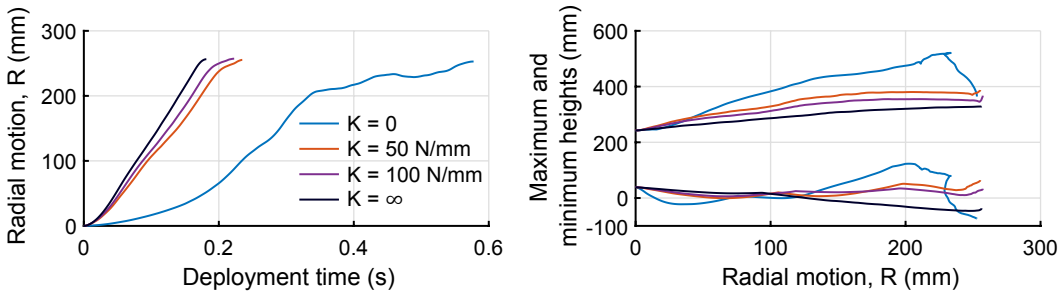

Figure 3.7: Radial motion of the structure with time, and deployment envelopes with radial motion for varying kickoff spring stiffness, K. Since two kickoff springs are used, total stiffness is $2K$. Gravity is absent. retractor force $F = 2$ N. Membrane density $\rho = 100$ g/m^2.

As expected, the deployment is the slowest when there is no kickoff spring and the fastest when the cylinder instantly clears the structure upon release (Figure 3.7). While there is a significant jump in the time taken for deployment when the kickoff spring stiffness is increased from $K = 0$ to $K = 50$ N/mm, the difference is minute for further increase in K.

The maximum and minimum heights the structure reaches during the deployment are also presented in Figure 3.7. Vertical (z-) positions of the nodes along the edges of the webs of all the six TRAC longerons were considered in this search. As noted earlier, the cylinder acts as a ramp causing the structure to reach higher vertical positions. This effect reduces with increasing kickoff spring stiffness K.

Since the only role of the cylinder is to maintain the structure in its folded configuration, it must be moved away from the structure as soon as possible after deployment begins. This is supported by the findings presented here. For the simulations performed hereafter, two kickoff springs with stiffness $K = 100$ N/mm each will be used.

3.3 Effect of gravity

While the structure and deployment mechanism are designed for space applications, away from the influence of Earth's gravity, preliminary tests are conducted on the ground, i.e., in the presence of gravity. Hence, it is essential to know how reliable on-the-ground deployment tests are in gaining insights into in-space deployments.

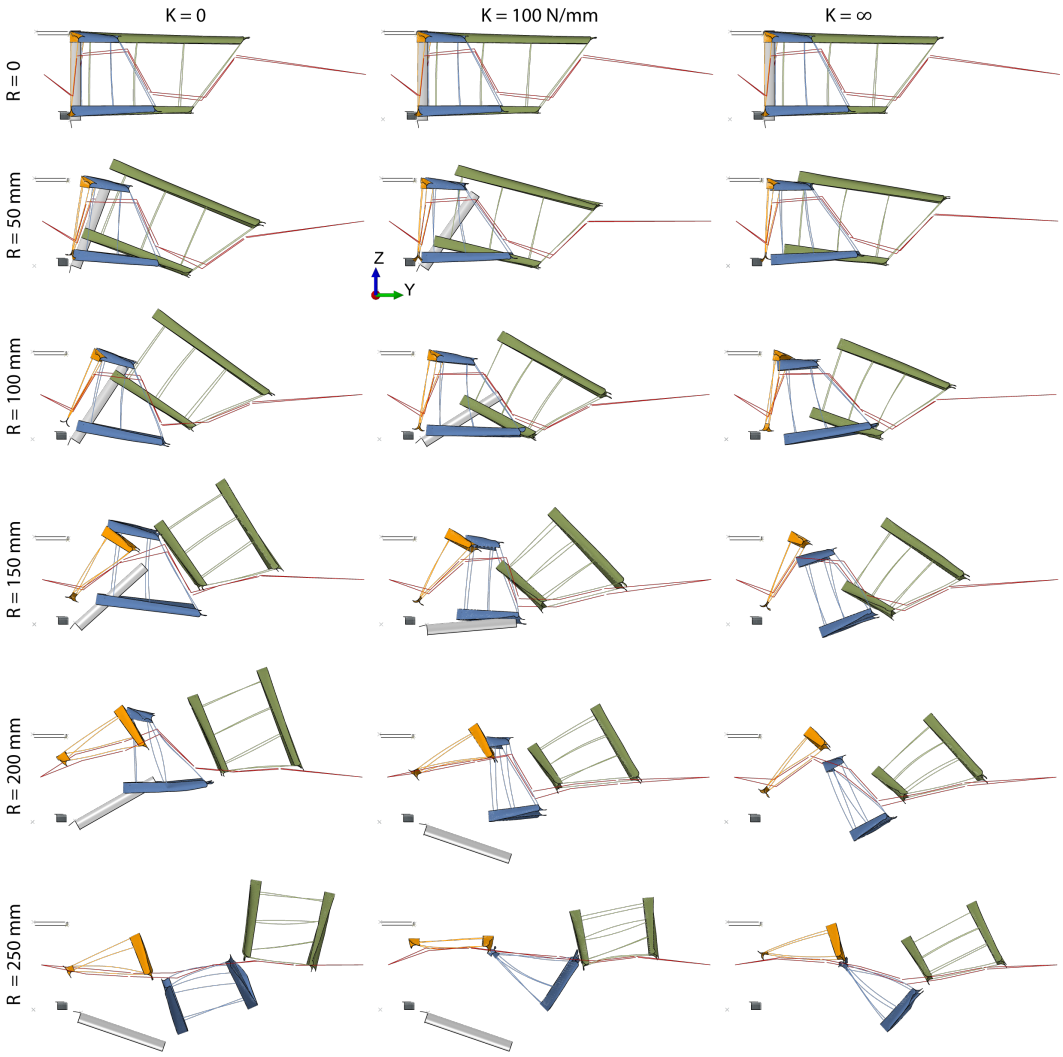

Figure 3.8: Deformed profiles of the structure at various levels of radial motion with kickoff spring stiffness, $K = 0$, 100 N/mm, or ∞. Since two kickoff springs are used, total stiffness is $2K$. In all cases, retractor force $F = 2$ N and membrane density $\rho = 100$ g/m^2. Gravity is absent.

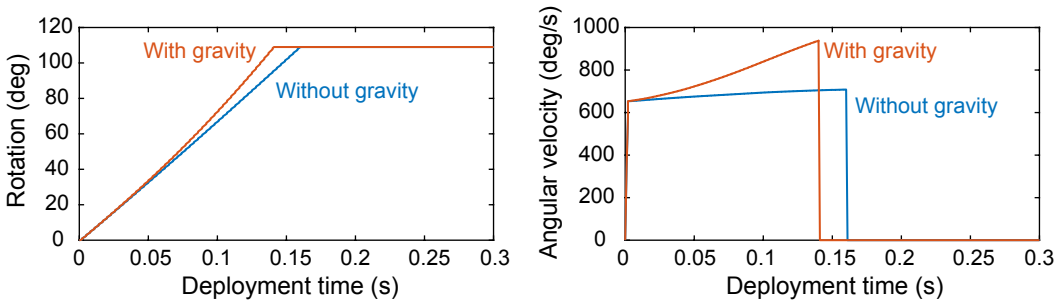

Figure 3.9: Effect of gravity on the rotation and angular velocity of the cylinder. Kickoff spring stiffness $K = 100$ N/mm. Cylinder locks at a rotation of 109° in the simulations.

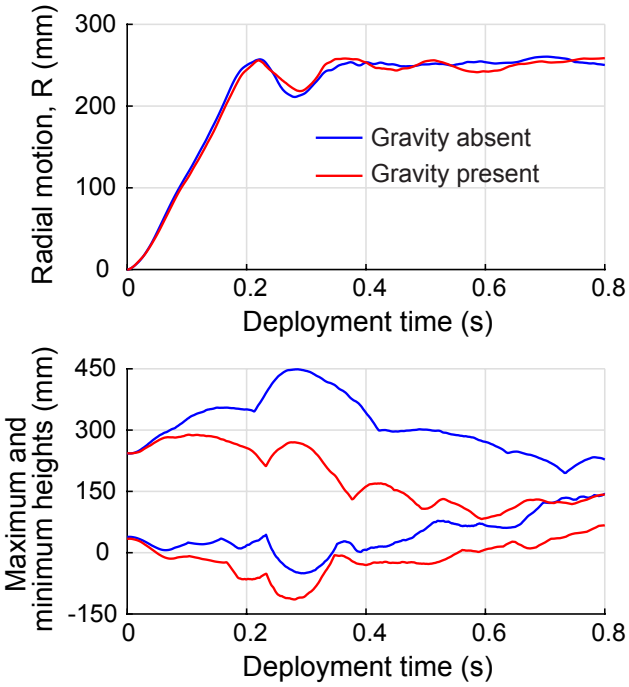

Figure 3.10: Effect of gravity on the radial motion and maximum and minimum heights of the structure. Kickoff spring stiffness $K = 100$ N/mm. Constant retractor force $F = 2$ N, and membrane density $\rho = 100$ g/m^2.

We performed numerical simulations of the deployment both with and without simulating the influence of Earth's gravity. In the presence of gravity, the cylinder rotates faster and reaches its final state sooner. However, this does not affect the time taken for the structure to reach its maximum radial position (Figure 3.10). This is because the cylinder ceases to interact with the structure soon after its release (Section 3.2).

While the rotations of the individual strips, α remain almost the same before the structure reaches maximum radial position (approximately 0.22 s), differences can be seen afterwards. For example, the strips take longer to latch into their fully deployed states (or 180° fold angles) in the absence of gravity. In addition, once the structure reaches the maximum radial position, the amplitude of oscillations of the outermost Strip 3 is greater in the absence of gravity while that of Strip 2 remains almost the same (Figure 3.11).

While the overall shapes of the evolution of the maximum heights reached by the structure during deployment appear similar, a significant difference is seen in their magnitudes. The whole deployment envelope shifts upward and the structure can reach significantly higher vertical positions in the absence of gravity.

Therefore, despite the differences in the deployment behavior, ground tests can still be used to reasonably predict the radial motion and the orientations of the strips during deployment in space, and the design choices must allow more vertical clearance for a successful deployment.

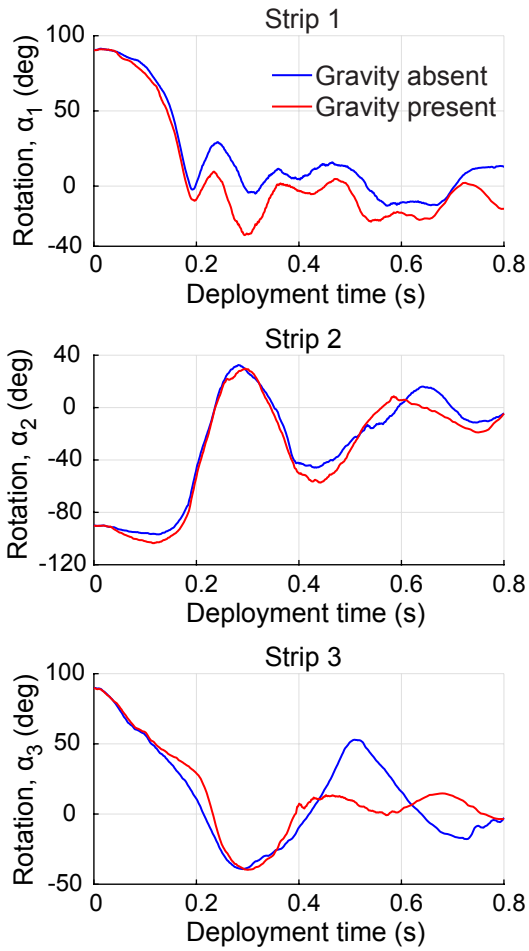

Figure 3.11: Effect of gravity on the strip rotations. Kickoff spring stiffness $K = 100$ N/mm. Constant retractor force $F = 2$ N, and membrane density $\rho = 100$ g/m^2.

3.4 Effect of constant retractor force

While the folded structure deploys and unfolds solely due to its own stored strain energy, the outer ends of the structure are guided by the constant force spring retractors. Hence, the retraction force offered by the spring retractors affects the dynamics of the deployment.

The time taken for the deployment is not of primary concern and the amount of retractor force that promises a successful deployment must be chosen. Since the deploying (or retracting) force and the rotation of the cylinder have opposite effects

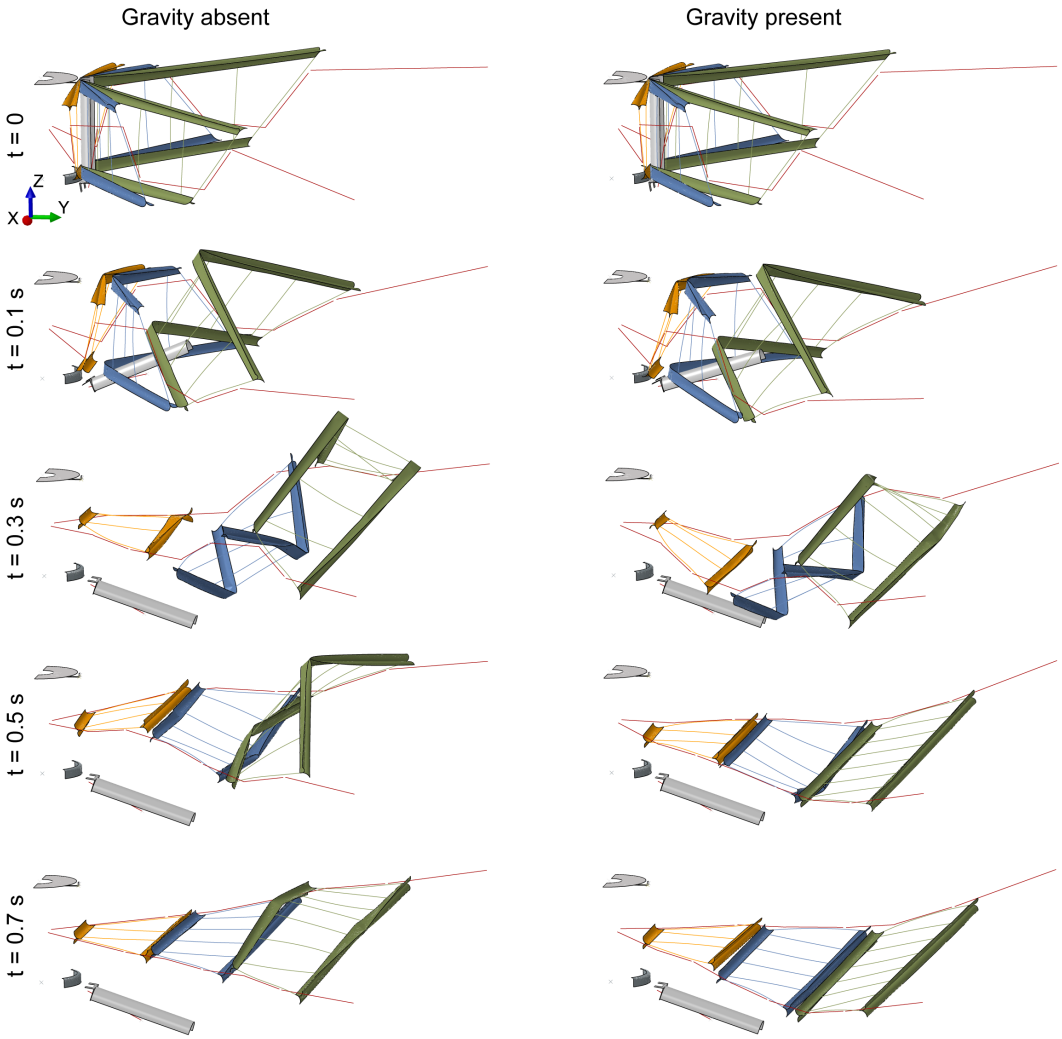

Figure 3.12: Effect of gravity on the deployment. Kickoff spring stiffness $K = 100$ N/mm. Constant retractor force $F = 2$ N, and membrane density $\rho = 100$ g/m^2.

on the motion of the structure, the optimal force depends on the chosen stiffness of the kickoff springs.

Deployment of the structure with various values for the retractor force was simulated. In all cases, kickoff spring stiffness $K = 100$ N/mm, and areal density of the membrane $\rho = 100$ g/m^2.

As the retractor force in the diagonal cords increases, the maximum height reached by the structure also increases (Figure 3.13). Significant increase in the maximum height happens before the structure reaches its maximum radial position. Further rise in maximum height happens because of the rotation of the outermost strip about the position of maximum radial distance.

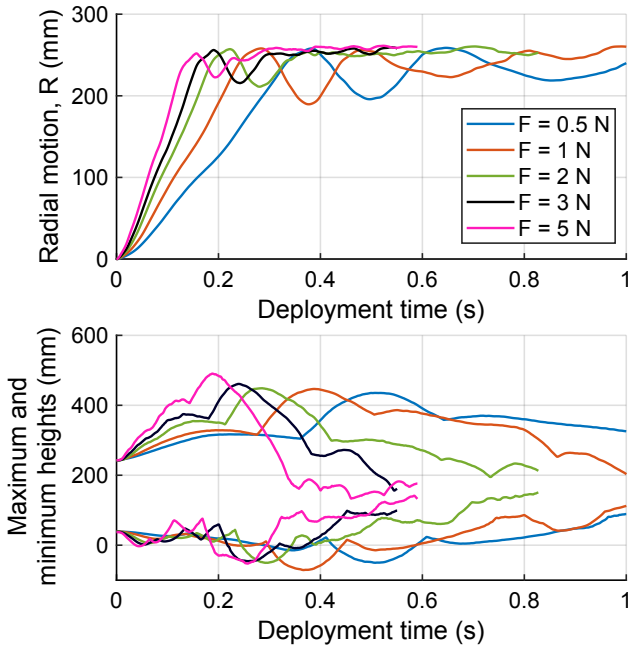

Figure 3.13: Radial motion of the structure and deployment envelopes for different pulling forces in the diagonal cords. Kickoff spring stiffness $K = 100$ N/mm. Membrane density $\rho = 100$ g/m^2. Gravity is absent.

Deformation profiles for three of the cases $F = 1$ N, 2 N, 5 N are presented in Figure 3.14. When $F = 5$ N, the structure is pulled outward significantly faster than the cylinder can clear the structure. Hence the outermost Strip 3 (in green) slides along the cylinder and reaches higher vertical positions than in the other two cases. In addition, the outermost longeron of Strip 2 (in blue) also is pulled against the cylinder leading to multiple folds. Note that in the initial part of the deployment before the structure reaches its maximum radial position, Strip 3 needs to rotate in the same sense as the cylinder while Strip 2 needs to rotate in the opposite sense. Hence, the cylinder has an adverse effect (inducing multiple folds) on Strip 2 and not on Strip 3. This is evident from the deformation profiles in Figure 3.14. For example, in case of $F = 2$, two elastic folds can be seen in Longeron 4 of Strip 2 at $t = 0.2$ s.

Deployment with $F = 1$ N or less when $K = 100$ N/mm has maximum one fold in each longeron and the fold remains approximately in the same location of the longeron.

Therefore, a smaller pulling force leads to a smaller and lower deployment envelope and the deployment is less prone to the formation of additional folds.

In the simulations presented hereafter, a constant retractor force of 1 N will be used.

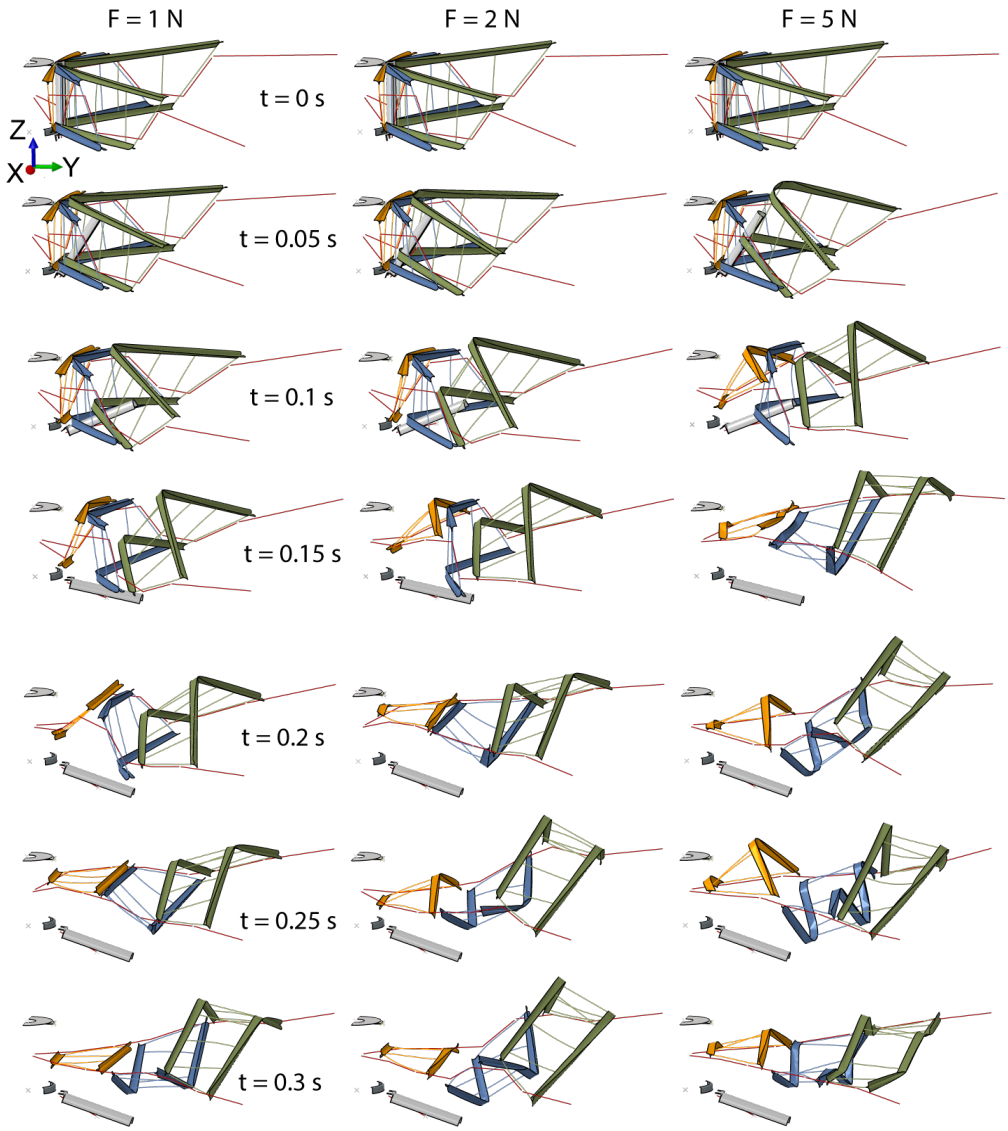

Figure 3.14: Deformation profiles of the structure during deployment with constant retractor forces $F = 1$ N, 2 N, or 5 N. Kickoff spring stiffness $K = 100$ N/mm. Membrane density $\rho = 100$ g/m^2. Gravity is absent.

Analyzing the deployment with $F = 1$ N, $K = 100$ N/mm, $\rho = 100$ g/m^2

We analyze the deployment of the structure further using the optimal combination of parameters: retractor force $F = 1$ N, kickoff spring stiffness $K = 100$ N/mm, and membrane density $\rho = 100$ g/m^2.

The validity of the solution from an explicit finite element analysis must be established using the energy histories. Figure 3.15 shows the energy output by Abaqus for the simulation of interest. Time is chosen to be zero at the beginning of deployment and is negative during the folding processes. The kinetic energy is negligible at the

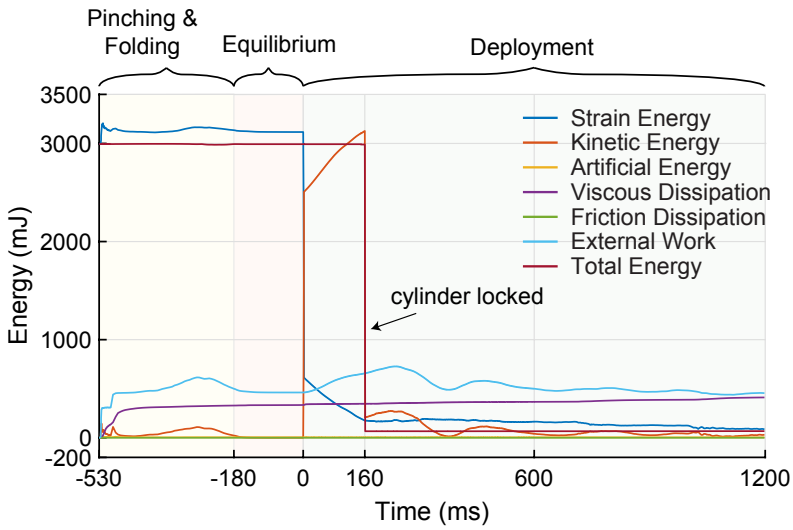

Figure 3.15: Energy history in the simulation with a constant retractor force of 1 N.

beginning of deployment ($t = 0$). Since the kickoff springs provide an impulse over a rotation of 0.9° of the cylinder, the kinetic energy rises almost instantaneously at $t = 0$. Beyond this, the kinetic energy results from contributions of the cylinder as well as the deploying structure.

Since the rotation of the cylinder was arrested at 109° (Figure 3.6), the kinetic energy of the cylinder was removed from the system and hence, the kinetic energy and the total energy dropped instantly. This fall in total energy is equal to the amount of kinetic energy removed. Before this instant and after, the total energy remains constant. At the end of deployment, the kinetic energy becomes negligible as the structure gets close to its fully deployed state.

The strain energy starts from a non-zero value at the beginning of the folding process as it includes the strain energy stored in the torsion spring (of stiffness 100 Nmm/rad and precompressed by 180°) in the cylinder hinge as well as that stored in the kickoff springs. As mentioned in Section 2.4, the longerons were pinched over a short duration to assist folding. This lead to a sharp rise in the strain energy near $t = -530$ ms.

The total strain energy remains constant throughout the equilibrium step and starts to decrease when the cylinder is released. Since the two kickoff springs were precompressed by 5 mm, the strain energy stored in them (2500 mJ) is released almost instantaneously. Towards the end of deployment, the strain energy reaches a non-zero steady state value equal to the strain energy remaining in the torsion springs that are still compressed by 81°.

In addition, the artificial energy is negligible throughout the simulation.

Friction dissipation is zero everywhere since the cylinder hinge was assumed to be frictionless.

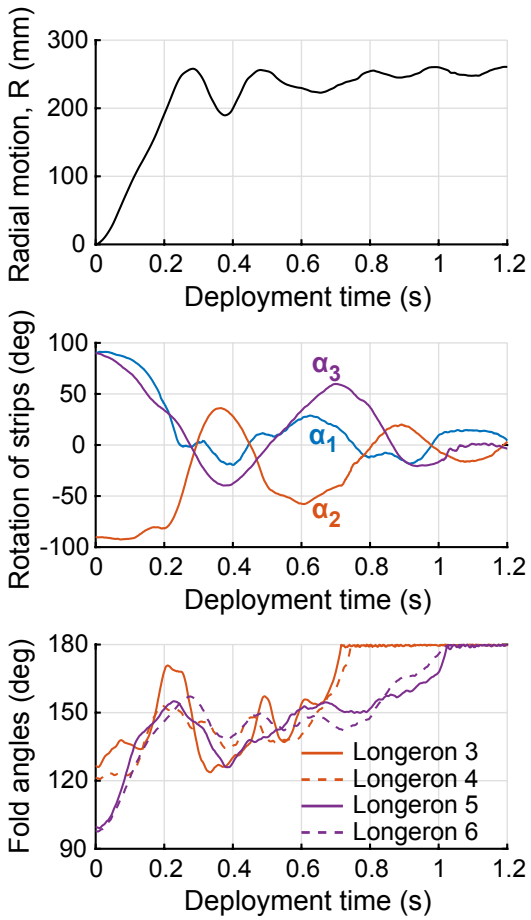

Figure 3.16: Constant retractor force = 1 N. Kickoff spring stiffness $K = 100\,\mathrm{N/mm}$. Membrane density $\rho = 100\,\mathrm{g/m^2}$. Gravity is absent.

The behavior of the structure during deployment is quantified by the radial motion of the outermost strip-cord connectors R, rotations of the strips α, and fold angles in the longerons presented in Figure 3.16. The structure reaches its maximum radial distance of $R = 258$ mm within 0.3 s and the strips rotate about this point until all the longerons fully unfold. Since there is no damping in the deployment steps of the simulation, the structure continues to oscillate about its fully deployed state.

Strip rotation α is defined as the angle the vector connecting the midpoints of the longerons makes with the Y- axis on the YZ plane (Figure 3.5). We noticed that, throughout the deployment, the midpoints of all the six longerons remain within 10 mm from the YZ plane. Hence the strip rotations defined here, along with the fold

angles, provide complete information on the shapes and orientations of the strips. Because the structure is Z-folded (Figure 3.21), strips 1 and 3 begin at $\alpha_1 = \alpha_3 = 90°$ at $t = 0$ while Strip 2 begins at $\alpha_2 = -90°$.

Since the retractor force acts directly on the outermost Strip 3 and since this strip needs to rotate in the same sense as the cylinder, α_3 begins to change as soon as the cylinder is released. This is evident from the non-zero slope of the curve corresponding to α_3 at $t = 0$ in Figure 3.16.

On Strip 2, the retractor force acts at the strip-cord connectors closest to Longeron 4. Since this longeron is closer to the hinge of the cylinder and since Strip 2 needs to rotate in a sense opposite to that of the cylinder, α_2 remains almost constant until the cylinder rotates by a certain amount making space for Strip 2 to deploy. Therefore, the curve corresponding to α_2 begins with zero slope.

The innermost Strip 1 is restricted by the interior Strip 2 and hence α_1 changes slowly upon deployment and starts with a zero slope. This behavior is also evident from the deformed profiles in Figure 3.14.

The longerons 5 and 6 (of Strip 3) have fold angles of approximately 100° in the folded configuration while the longerons 3 and 4 (of Strip 2) begin at fold angles close to 120°. The complex evolution of these fold angles through the deployment is shown in Figure 3.16. The longerons 1 and 2 of Strip 1 start with fold angles slightly smaller than 180°. They latch into their flat states within 0.2 s and remain that way for the rest of the deployment (not shown here). The reason for the difference in the initial fold angles among the three strips was explained in Section 2.5.

3.5 Effect of membrane mass

The structure is intended to host functional elements such as photovoltaic cells and RF antennas. These elements would be mounted on a Kapton membrane that fills all the gaps among the longerons and battens of every strip. Since the membrane would be rigidly bonded to the strips at the longeron-batten intersections [34], the mass of the membrane and functional elements (all together referred to as membrane for simplicity) is approximated through point masses at the longeron-batten intersections. For example, for an areal density of the membrane $\rho = 100$ g/m^2, Figure 3.4 shows the point masses needed at all the longeron-batten intersections. Only the mass of the membrane is approximated and other effects of the membrane such as air drag and wrinkling are not modeled in this study.

We simulated the deployment of the structure for three different values of membrane

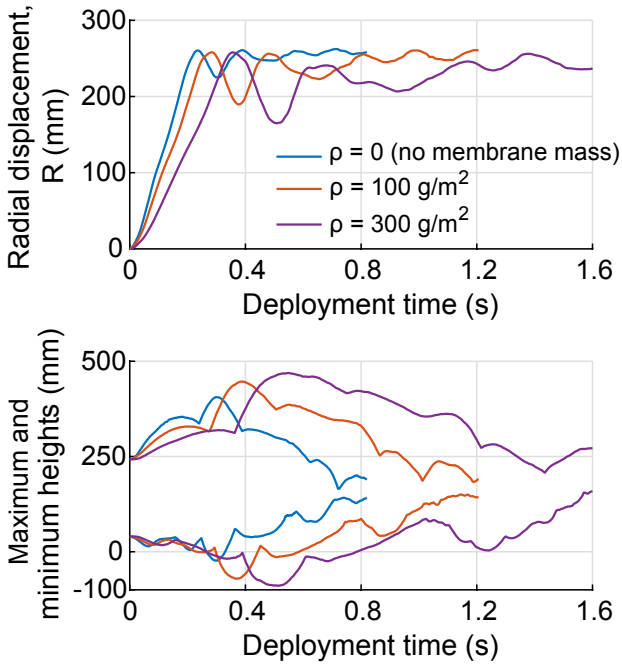

Figure 3.17: Effect of membrane density on the radial motion and deployment envelope. Constant retractor force $F = 1$ N. Kickoff spring stiffness $K = 100$ N/mm.

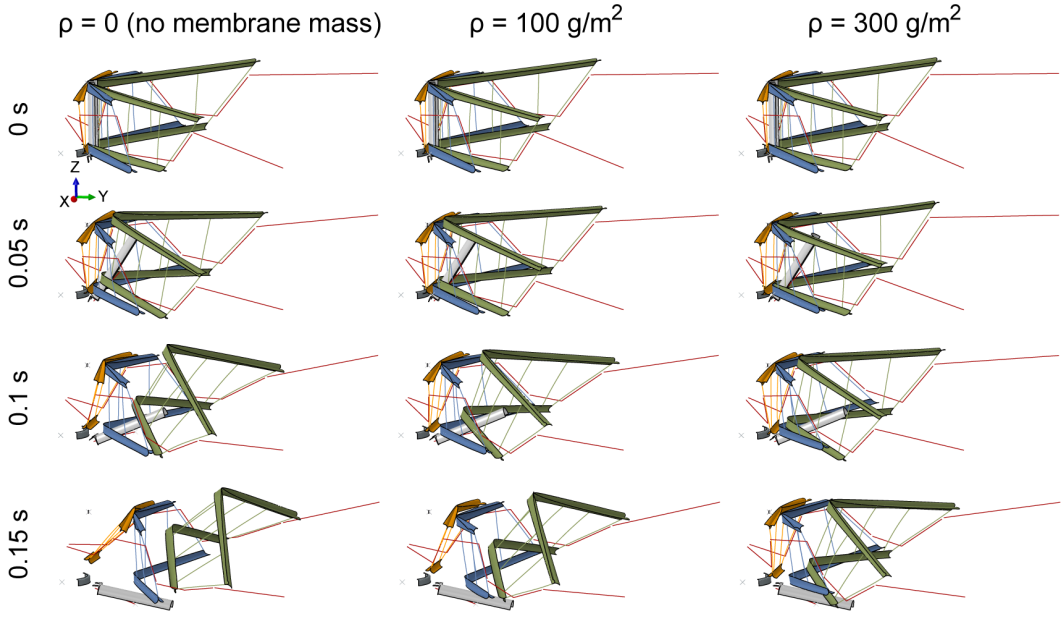

Figure 3.18: Effect of membrane density on the deformation profiles in the first 0.15 s. With increase in mass, the structure moves slower at the beginning of the deployment thus interacting less with the cylinder. Constant retractor force $F = 1$ N. Kickoff spring stiffness $K = 100$ N/mm.

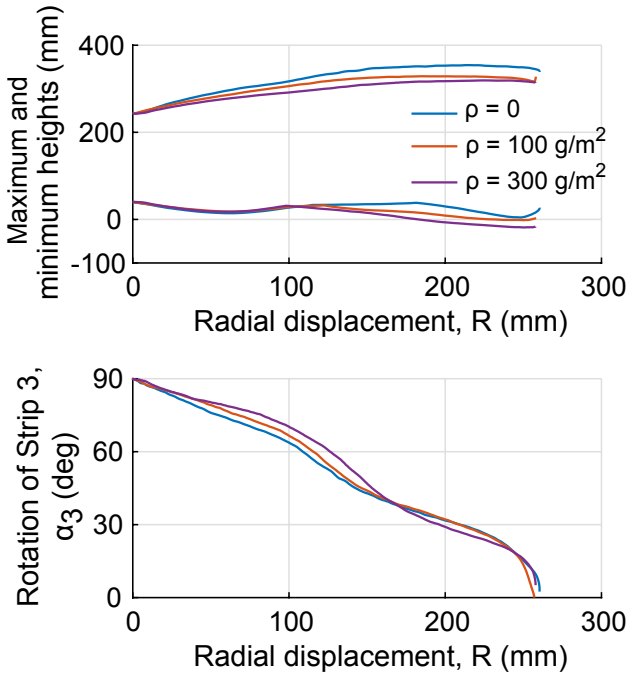

Figure 3.19: Evolution of maximum and minimum heights, and rotation of Strip 3 until the first instant structure reaches its maximum radial position. Constant retractor force $F = 1$ N. Kickoff spring stiffness $K = 100$ N/mm.

density $\rho = 0$ (no membrane), $\rho = 100$ g/m^2, and $\rho = 300$ g/m^2. In all these cases, constant retractor force $F = 1$ N, and kickoff spring stiffness $K = 100$ N/mm.

Before the structure reaches the maximum radial position, increasing the density of the membrane results in a decrease in the maximum heights reached by the structure (Figures 3.17 and 3.19). This is because with increase in inertia, the structure starts slower and the structure-mechanism interaction is reduced (Figure 3.18).

The deployment behavior is opposite after the structure reaches its maximum radial position. Due to the increase in inertia with increasing membrane density, after the structure reaches its final radial position, amplitude and time period of the rotation of the outermost strip increases (Figure 3.20). This results in an increase in the maximum heights reached by the structure (Figure 3.17).

Nevertheless, in all the three cases, it was observed that no additional folds were created in the longerons during the deployment and the existing folds were stationary as desired.

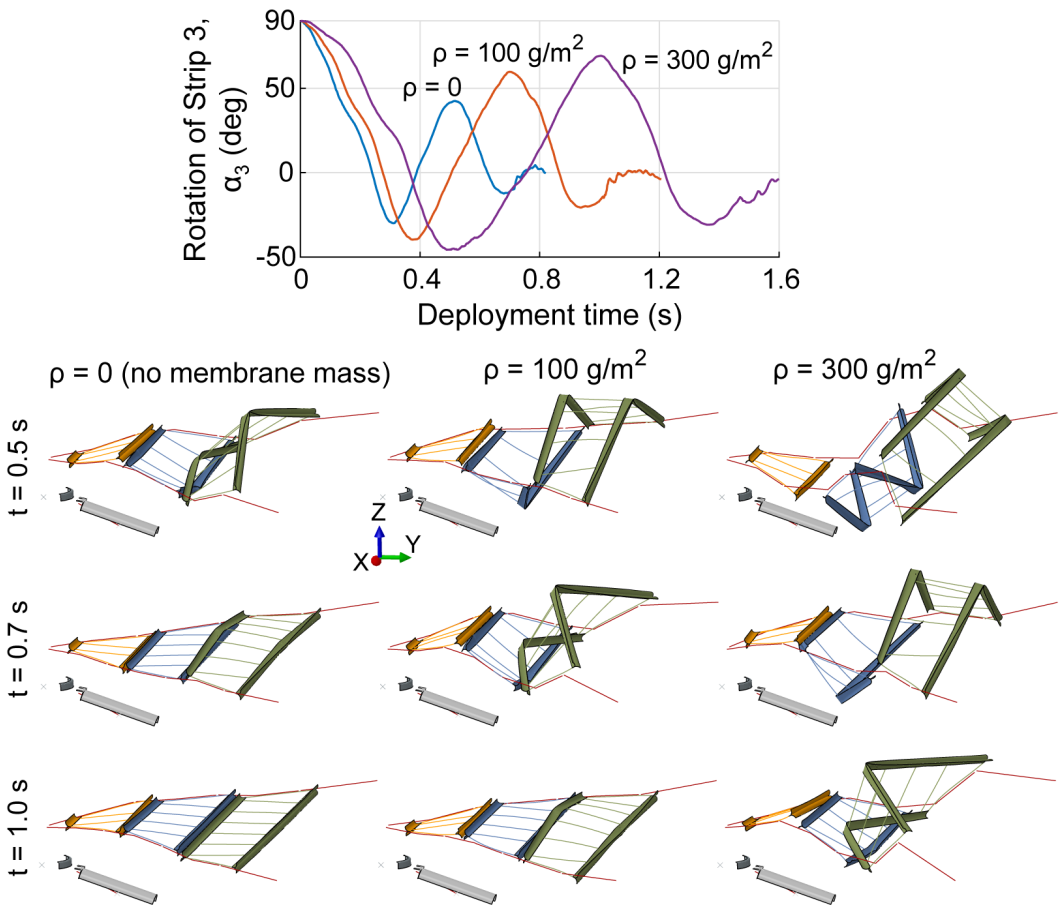

Figure 3.20: Effect of membrane mass on deployment dynamics. Constant retractor force $F = 1$ N. Kickoff spring stiffness $K = 100$ N/mm.

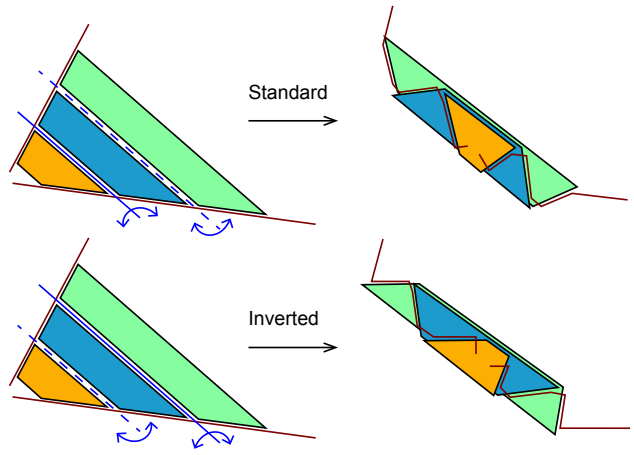

Figure 3.21: Two possible orientations of the Z-folded structure. Solid blue line represents a mountain fold and dashed line represents a valley fold.

3.6 Effect of structure orientation

The structure is Z-folded before folding and installing it in the deployment mechanism. There are two possible ways of Z-folding the structure (Figure 3.21) and both the folded states lead to the same fully deployed configuration. Thus far, only one orientation of the structure has been studied and the deployment path from the inverted orientation to the identical final state is unknown.

When the structure is stowed in the standard orientation (Figure 3.21), Longeron 6 is close to the top of the cylinder and when it is stowed the inverted orientation, Longeron 6 is close to the hinge of the cylinder. Since the force applied by the cords acts directly on the outermost strip-cord connectors that are closest to Longeron 6, the interaction between Strip 3 and the cylinder depends on the initial orientation. For example, with the inverted initial orientation, Longeron 6 stays in contact with the cylinder longer resulting in a slow start of the deployment. This is evident from the smaller slope of radial motion, R with time in Figure 3.22. In addition, Strip 3 remains vertical ($\alpha_3 = -90°$) for a longer duration (Figure 3.23) and hence the zero slope of rotation α_3 at $t = 0$ in Figure 3.22. These initial differences in the deployment dynamics result in only a small difference in the time taken to reach the maximum radial position.

A major deviation from the standard deployment behavior is seen in the maximum and minimum heights reached by the structure after it reaches its maximum radial position (approximately 0.3 s). This is because of the difference in sense of rotation of Strip 3. With the standard initial orientation, Strip 3 rotates forward (away from the central hub) and reaches higher vertical positions whereas with the inverted initial orientation, Strip 3 rotates backward and reaches lower vertical positions.

Therefore the initial orientation of the structure can be chosen based on the limitation on the vertical clearance available for the structure, and the allowable amount of structure-mechanism interaction which in turn depends on the speed of cylinder rotation (Section 3.2) and the retractor force (Section 3.4).

3.7 Effect of strip-cord connectors locations

As mentioned earlier, each strip is connected to two diagonal cords through four strip-cord connectors (SCCs). The outermost SCCs on each strip, i.e., those closest to the longest longeron of the strip are rigidly bonded to the cords while the cords can freely slide through the innermost SCCs. Due to this arrangement, the tension forces in the cords act directly on the outermost SCCs. Hence, the choice of locations of

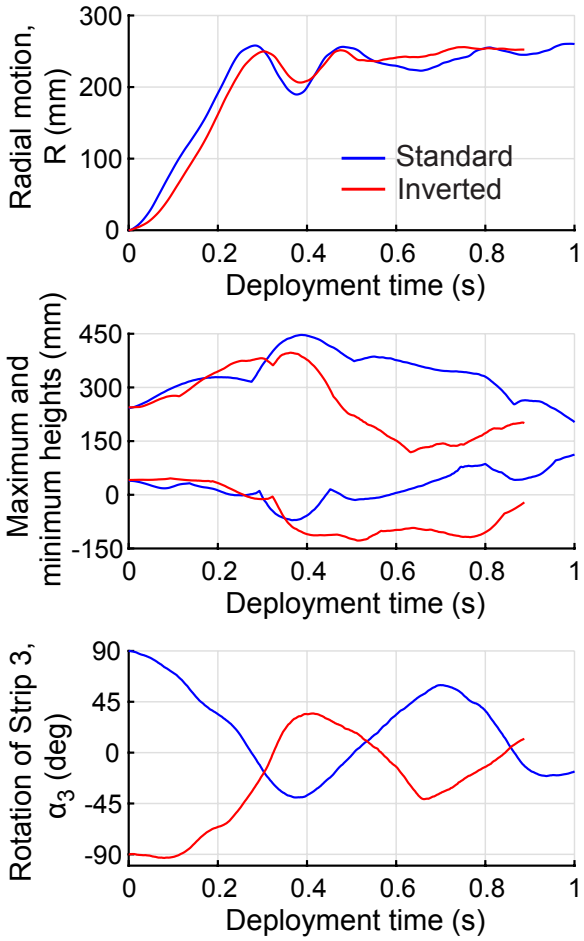

Figure 3.22: Comparison of the orientation of the structure. Constant retractor force = 1 N.

SCCs affects the kinematics and dynamics of the deployment. Since the length of a cord available between adjacent strips determines how the adjacent longerons interact with each other during deployment, the locations of the SCCs also affects the success of the deployment. Moreover, the locations of the SCCs are of particular interest since they are decided at the final stage of assembling the structure and can be altered without damaging the strips.

In the structure studied thus far, the SCCs were placed asymmetrically on the diagonal battens (Figure 3.24). However, to reduce the number of variables, we place the SCCs at equal distances from the ends of the diagonal battens in this particular analysis (Figure 3.25). We simulate three scenarios with the distances of an SCC from an end of a diagonal batten $x = 0.1d$, $0.2d$, $0.3d$, where d is the length of a diagonal batten. $x = 0$ is not possible because of the conflict between the

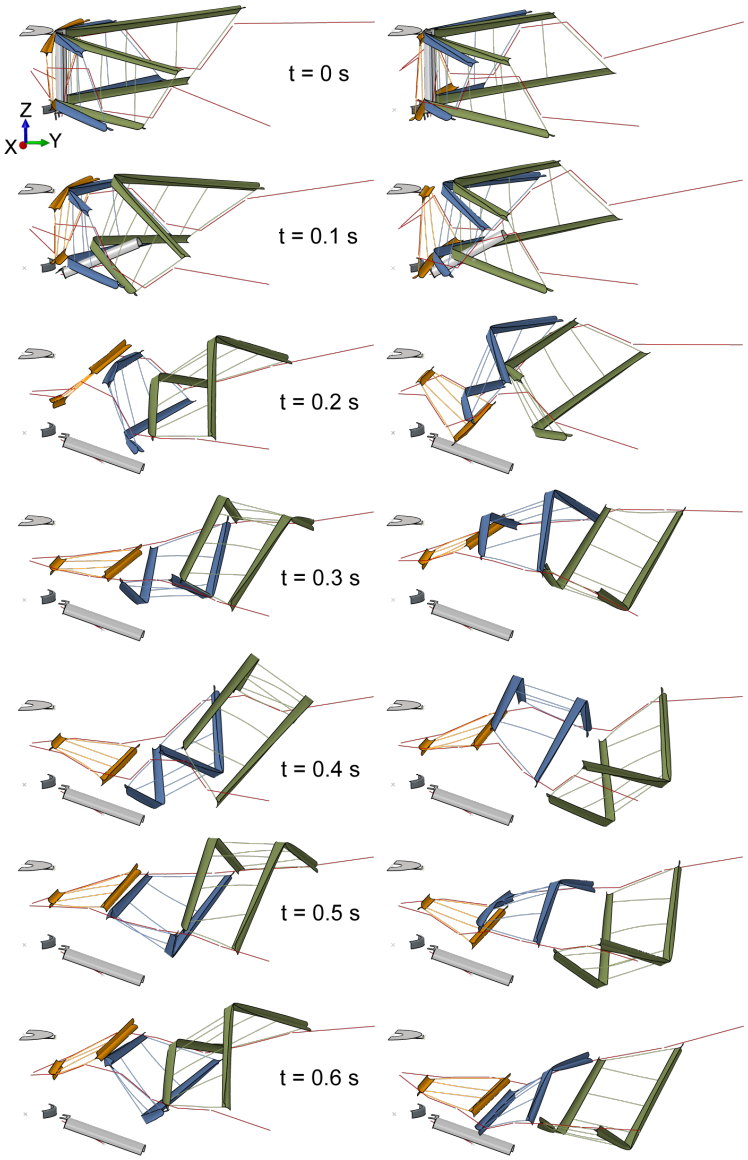

Figure 3.23: Comparison of the orientation of the structure – deformation profiles. Constant retractor force = 1 N. Kickoff spring stiffness $K = 100$ N/mm. Membrane density $\rho = 100$ g/m^2.

required length of the cord between Strip 1 and central shaft and the gap between the central shaft and the deploying cylinder.

The cord tension of $F = 1$ N acts directly on the outermost SCCs of Strip 3. Tension forces in the interior portions of the cords are determined by the moments needed to maintain the fold angles in the strips which in turn depend on the lengths of the

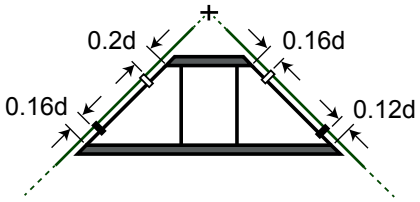

Figure 3.24: Locations of the strip-cord connectors in the structure studied thus far. Strip 1 is shown as an example and the same placement is true for all the strips of the structure. d is the length of a diagonal batten.

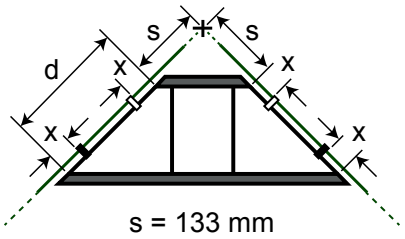

Figure 3.25: Strip-cord connectors are placed at equal distances, x from the ends of the diagonal battens. Strip 1 is shown as an example and the same placement is true for all the strips of the structure. d is the length of a diagonal batten.

cords between adjacent strips.

Since the length of a cord from the central shaft to the point of attachment to a spring retractor (Figure 3.2) must be the same in any scenario, the amount of cord between any two adjacent strips decreases with decreasing x. Therefore, the strips are much closer to each other when $x = 0.1d$ than in the other two cases which resulted in snagging between Strips 1 and 2 (for example, at $t = 0.2$ s in Figure 3.30).

For the same reason, the smallest Strip 1 is more folded (smaller initial fold angle) when $x = 0.1d$ compared to the other cases (Figures 3.26 and 3.28).

In addition, due to the chosen gap between the central shaft and the cylinder in the mechanism (Figure 3.3), the interior portions of the cords, i.e, those attached directly to the central shaft, are significantly taut resulting in larger bending curvatures in all the diagonal battens. On the other extreme, for $x = 0.3d$, all the interior portions of the cords have negligible tension and the innermost Strip 1 is the least folded compared to the other two cases.

The evolution of fold angles in the longerons is unique to each case (Figure 3.28). However, the shapes of the curves for $x = 0.2d$ and $x = 0.3d$ are closer to each other and differ significantly from those for $x = 0.1d$. One unique feature of the deployment path in case of $x = 0.1d$ is that for the first 20% of the radial motion,

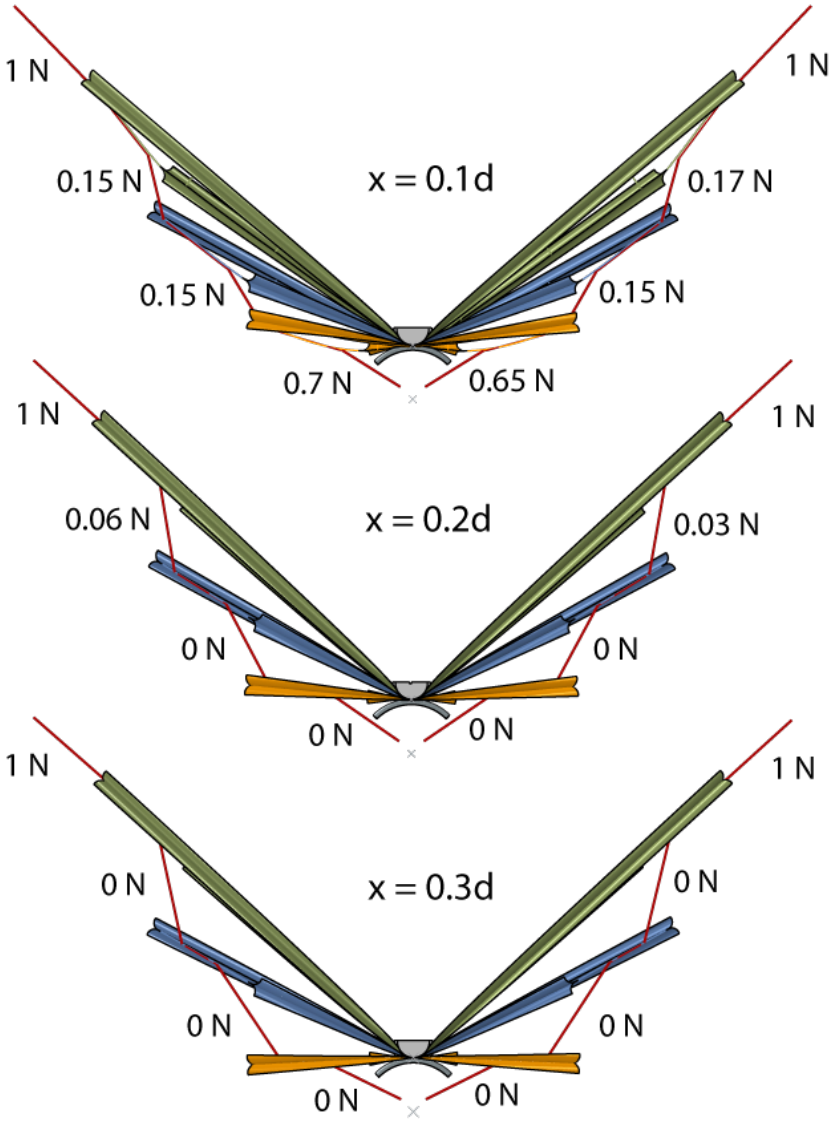

Figure 3.26: Top views of the folded structure with $x = 0.1d, 0.2d, 0.3d$.

Longeron 2 occupies the highest vertical position followed by Longeron 6 for the rest of the deployment (Figures 3.29 and 3.30). Whereas, for $x = 0.2d$ or $0.3d$, only Longeron 6 contributes to the maximum heights until the maximum radial position is reached. This means that the smallest Longeron 1 might come in contact with the top of the central hub and has implications on the design of the central hub when the SCCs are placed too close to the ends of diagonal battens.

Despite the differences, the time taken for the structure to reach maximum radial position is almost the same in all the three scenarios (not shown here). Also, no significant differences in the evolution of strip rotations α were noticed at least until the structure reaches the maximum radial position (at approximately 0.3 s).

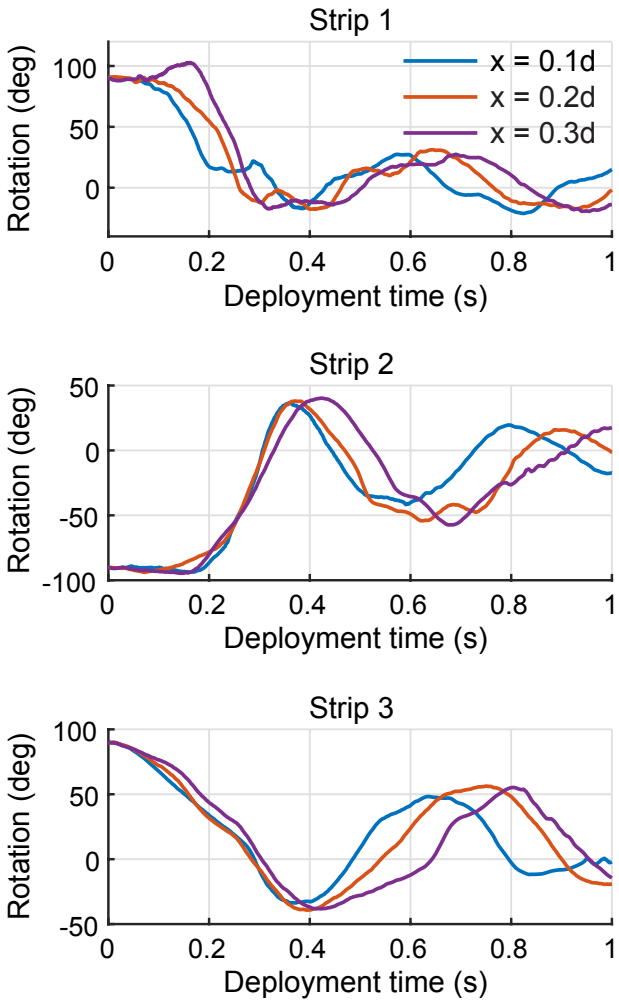

Figure 3.27: Rotations of the strips during deployment for different locations of the strip-cord connectors x. Constant retractor force $F = 1$ N. Kickoff spring stiffness $K = 100$ N/mm. Membrane density $\rho = 100$ g/m^2.

3.8 Conclusions

The numerical simulation techniques developed in the previous chapter have been used to study the effects of various influences on the deployment path of the Caltech SSPP structure. Important findings of this study are as follows.

1. **Cylinder:** Interaction between the structure and the deploying cylinder can significantly affect the deployment dynamics. The cylinder assists in maintaining the structure in its folded state and the deployment begins once the cylinder is released. Since the cylinder has no role to play during the deployment, it is crucial to eliminate any interaction between the cylinder and the structure. Ideally, the cylinder must be ejected out of the deployment path as

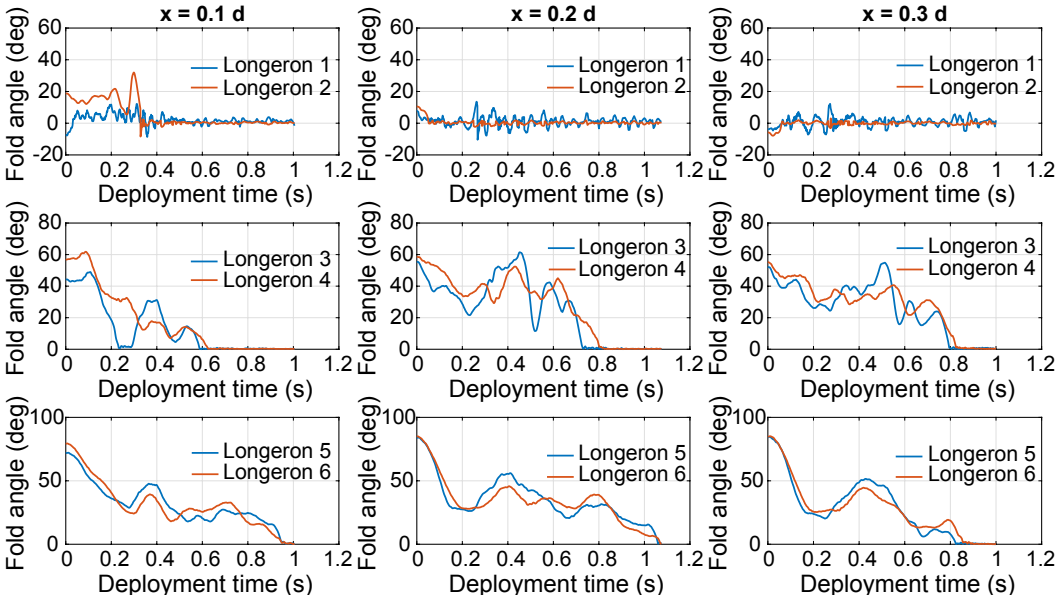

Figure 3.28: Fold angles in the longerons during deployment for different locations of the strip-cord connectors x. Constant retractor force $F = 1$ N. Kickoff spring stiffness $K = 100$ N/mm. Membrane density $\rho = 100$ g/m^2.

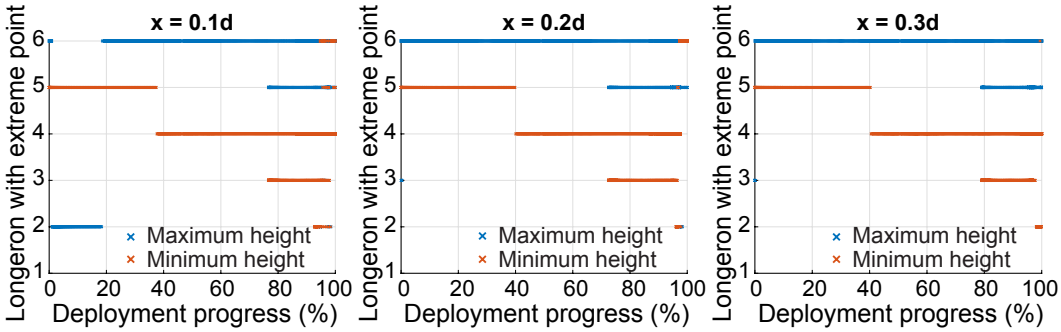

Figure 3.29: Longerons responsible for the maximum and minimum heights of the structure during the deployment. Deployment progress at an instant is the ratio of the current radial position of the structure (R) to the maximum radial position. Constant retractor force = 1 N. Kickoff spring stiffness $K = 100$ N/mm. Membrane density $\rho = 100$ g/m^2.

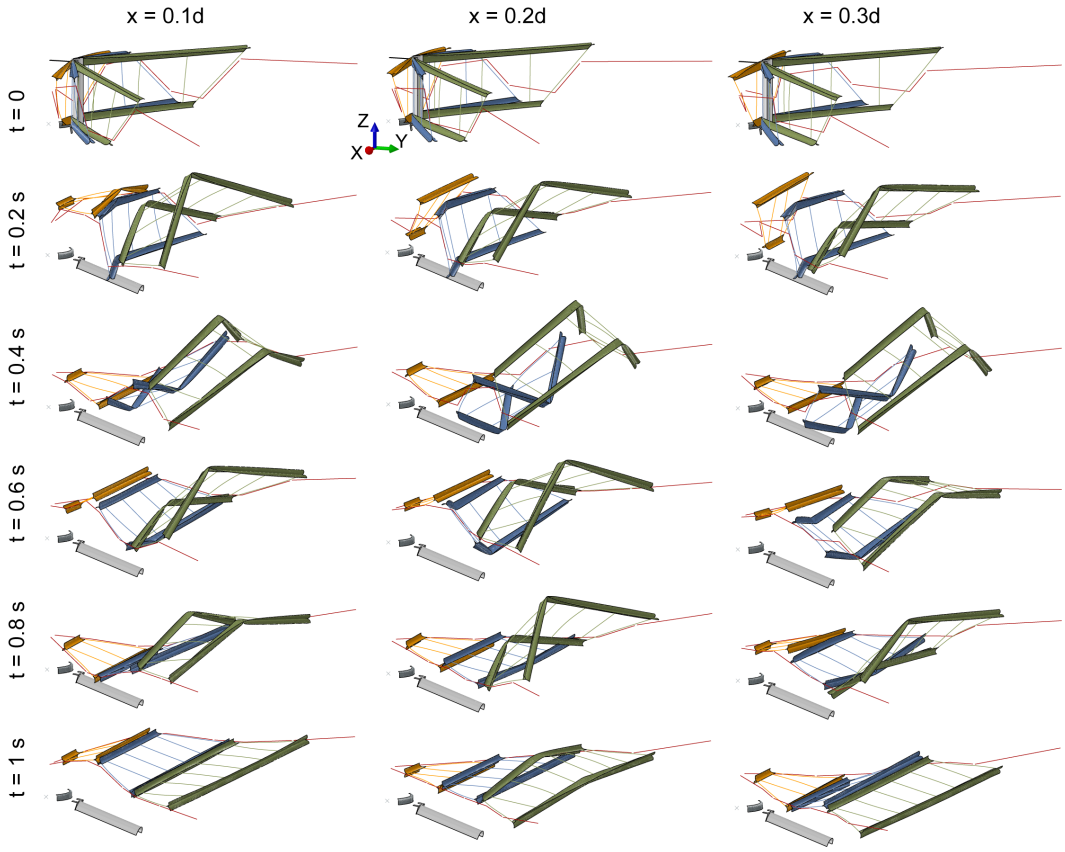

Figure 3.30: Fold angles in the longerons for $x = 0.1d, 0.2d, 0.3d$. Constant retractor force = 1 N. Kickoff spring stiffness $K = 100$ N/mm. Membrane density $\rho = 100$ g/m^2.

soon as it is released.

2. **Retractor force:** Upon release, the folded structure unfurls and latches into its original flat state due to the stored strain energy. Time taken for this process is unimportant as long as the deployment is predictable, damage-free and successful. Therefore, the tension forces in the diagonal cords need to be only large enough to guide the strips to their final radial positions and to stabilize the entire structure once it reaches it fully deployed state. A smaller retractor force also reduces the interaction between the cylinder and the structure resulting in a predictable deployment with lower maximum heights and constant number of stationary elastic folds.

3. **Gravity:** The radial motion of the structure is nearly identical with and without gravity. And, the orientations of the strips with respect to the ground plane are identical until the structure reaches its maximum radial position. The most significant difference is that in the absence of gravity, the structure

reaches significantly higher vertical positions. Therefore, the design choices must allow more vertical clearance for on-orbit deployment than needed in ground tests. However, the overall shape of the deployment envelope is similar in both cases, and together with the aforementioned observations, ground tests can still be used to reasonably predict the deployment path in space.

4. **Membrane mass:** Increasing the density of the membrane attached to the structure makes the deployment slower thus reducing the structure-mechanism interaction. This results in a decrease in the maximum height of the structure before it reaches its maximum radial position. Beyond this point, amplitude and time period of the oscillations increase resulting in an increase in the maximum height reached by the structure. However, the overall shape of the evolution of these quantities with time remains the same. In all the three cases simulated, no additional fodls were formed and the exiisting folds remained stationary, in the middle of the longerons.

5. **Initial orientation of folded structure:** The initial orientation determines which longerons interact with the cylinder, and significantly affects the maximum and minimum heights after the structure reaches its maximum radial distance. Therefore the initial orientation of the structure can be chosen based on the limitation on the vertical clearance available for the structure, and the allowable amount of structure-mechanism interaction which in turn depends on the speed of rotation of the cylinder and the retractor force.

6. **Locations of the strip-cord connectors:** This design choice affects the initial folded state and in turn, the initial fold angles and the tensions in various segments of the cords. Three different locations of the SCCs were studied. The time taken for the structure to reach maximum radial position is almost the same in all the three cases. Also, no significant differences in the evolution of strip rotations were noticed at least until the structure reaches the maximum radial position. However, when the SCCs are placed too close to the ends of diagonal battens, snagging can occur between adjacent strips causing material damage. This also has noticeable affect on the deployment path of the innermost strip and necessitates more vertical clearance within the central hub.

Chapter 4

DEPLOYMENT USING CONSTANT-FORCE SPRING RETRACTORS

4.1 Introduction

The prototype of the Caltech SSPP structure studied so far has a maximum length of approximately 1.7 m. The in-house manufacturing of the TRAC longerons uses an autoclave for curing the composite laminates [16] and the maximum length of a longeron was limited by the size of the autoclave. However, Caltech SSPP envisages a structure with a maximum length of 60 m and hence, out-of-autoclave manufacturing methods are needed to build bigger structures.

In Chapter 3, it was demonstrated that by choosing optimal initial conditions for deployment (rotation speed of cylinder and retractor force in diagonal cords), no additional folds will be created during the deployment. Moreover, the existing folds remain stationary, in the middle of the longerons. Therefore, multiple TRAC longerons can be bonded together to form a longer longeron as long as the location of the bond region is away from the middle of the resulting longeron where folds will be induced.

The objectives of this work are as follows.

- To develop an out-of-autoclave bonding technique for joining two TRAC longerons.
- To investigate the robustness of the bonding technique by manufacturing a larger structure and conducting deployment tests on the same.
- To implement kickoff springs and constant force spring retractors in the experiment setup. Kickoff springs increase the speed of rotation of the cylinder thus reducing its interaction with the structure during deployment. In addition, constant force spring retractors will be employed to guide the structure. As noticed in Chapter 2, hanging masses create undesired oscillations in the structure. This is due to the steep rise in the tensions in the cords needed to arrest the momentum of the masses when they reach their lowest vertical positions.

- To further test the fidelity of the numerical models (developed in Chapter 2) by simulating, and verifying against experiments, the deployment of a three-strip structure and a four-strip structure using kickoff springs and spring retractors.

4.2 Bonding two TRAC longerons

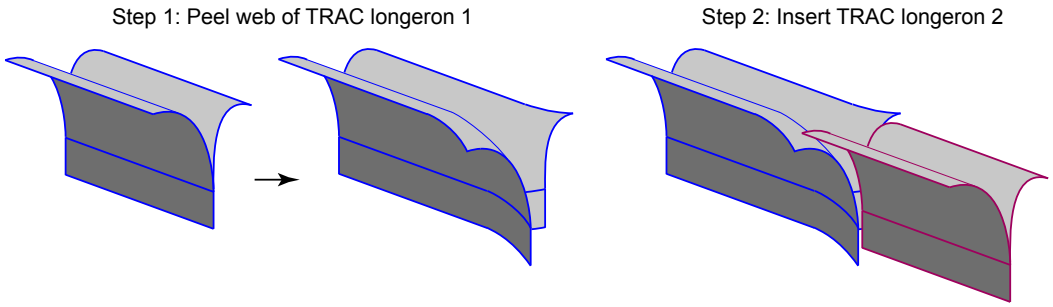

Figure 4.1: Illustration of the technique followed to bond two TRAC longerons.

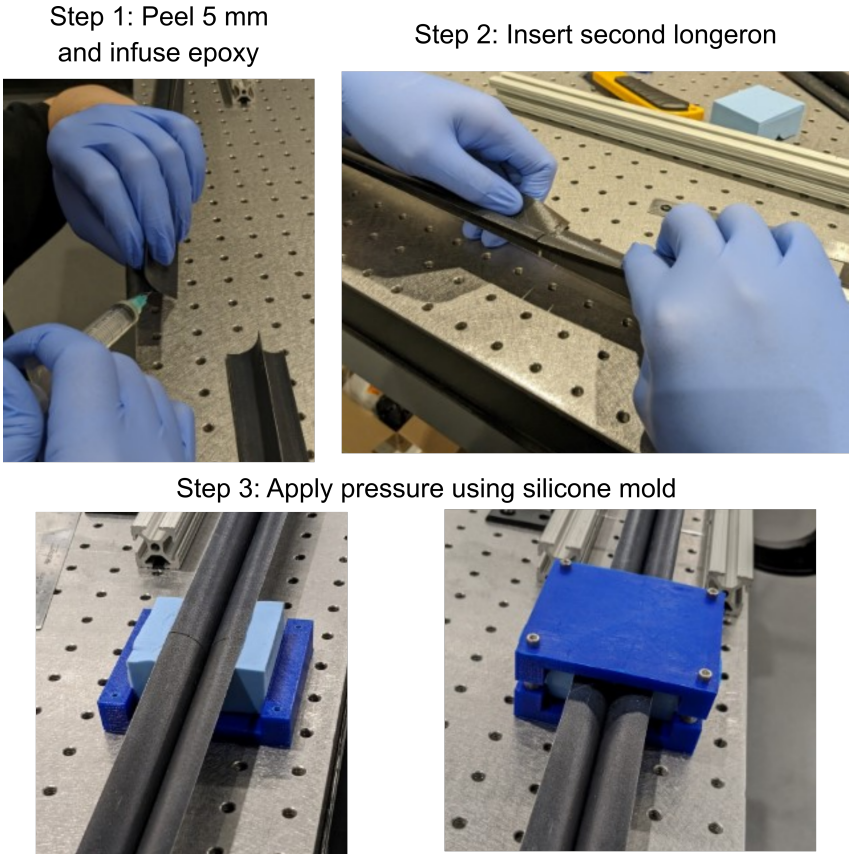

Figure 4.2: Procedure to bond two TRAC longerons with epoxy.

As specified in [18], the TRAC longerons are manufactured in an autoclave using a two-cure process. Each flange has the stacking sequence $[\pm 45_{GFPW}/0_{CF}/\pm 45_{GFPW}]$ and a thickness of 80 μm. CF represents a thin ply with unidirectional carbon

fibers and GFPW represents plain weave scrim glass (25 gsm). For the second cure, an additional glass fiber ply is inserted in between the flat regions of the two halves. This step results in a 7-ply web region with the stacking sequence $[\pm 45_{GFPW}/0_{CF}/\pm 45_{3,GFPW}/0_{CF}/\pm 45_{GFPW}]$ and web thickness of 185 μm.

After manufacturing two individual longerons in the autoclave, they can be bonded together as shown in Figure 4.1. The two flanges at the web region of a longeron are first delaminated over a range of 5 mm. This will result in two flaps one with three plies and the other with four plies. The second longeron is inserted into this gap and the overlapping regions are bonded with epoxy. Pressure is applied on the overlapped region by inserting it into a silicone mold and is maintained for 24 hours (Figure 4.2).

This bonding technique introduces a localized increase of stiffness at the location of the overlap. To mask this effect, the bonding locations are chosen to coincide with the locations of longeron-batten intersections. Battens and longerons were anyway connected together with epoxy leading to a local increase in stiffness [20]. Moreover, as observed in Chapter 3, the elastic folds in the longerons remain stationary, in the middle of the longerons, when the structure-mechanism interaction is minimized. Hence, an increase in stiffness away from the fold locations is not expected to affect the deployment. A schematic of the resulting four-strip structure is presented in Figure 4.3.

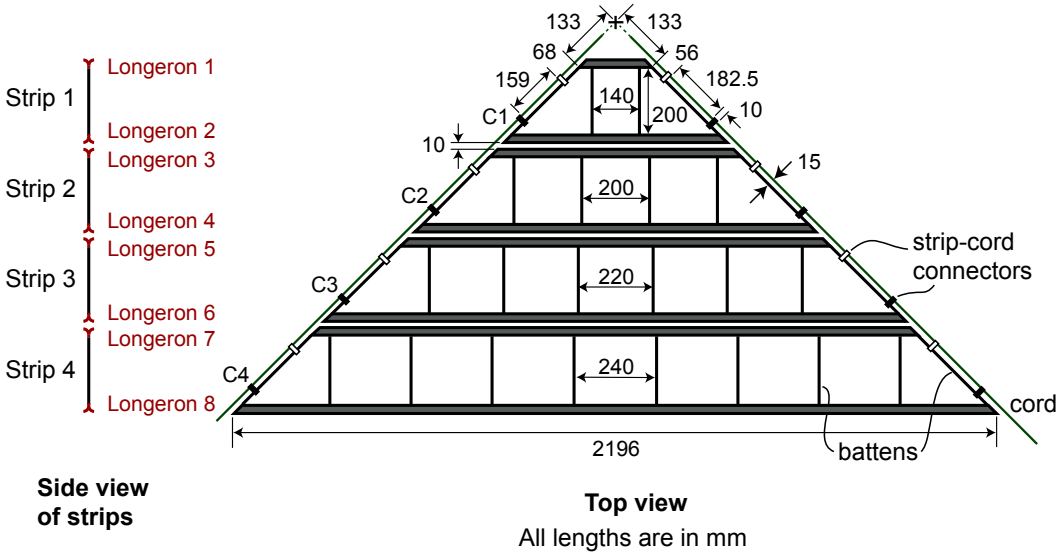

Figure 4.3: Schematic of the structure with four strips.

4.3 Improvements to deployment mechanism

Kickoff springs

It was demonstrated in the previous Chapter 3 that the rotation speed of the cylinder can be increased by utilizing kickoff springs. Two kickoff springs with stiffness of 15 N/mm each were installed on the top frame of the mechanism (Figure 3.3). This was the maximum stiffness possible with the existing deployment mechanism due to the limitations on the electromagnet used to hold the cylinder in stowed configuration. If each kickoff spring were precompressed by 4 mm in the stowed configuration, initial force applied by these springs at the top of the cylinder in stowed configuration would be 120 N.

Spring retractors

To avoid the undesired oscillations or the inertia effects associated with hanging masses in Chapter 2, spring retractors were instead used to drive the deployment. The retractors marketed as *Negators*, with part number ML-1448 and a cable tension rating of 1.67 N, by Hunter Spring were used. Four such retractors were tested on an Instron universal testing machine and the best two retractors that showed the least variation in the cable tensions were used in the deployment tests (Figure 4.4). The maximum displacement rate possible on the Instron machine, 8.5 mm/s was used in the tests.

4.4 Deployment of three-strip structure

To verify the numerical simulations against the deployment tests using spring retractors and kickoff springs, deployment test was first conducted on the three-strip structure introduced in Chapter 2. Positions of the strip-cord connectors C1, C2 and C3 denoted in Figure 4.3, fold angles in the longerons, deployment envelopes from the experiment and numerical simulations are compared (Figures 4.5, 4.6, and 4.7). The deviations in these predicted quantities from experiments were computed at all the time instants where the experimental data is available and are listed in Tables 4.1, 4.2 and 4.3. The motion capture data of certain reflective markers becomes unavailable when they are not visible to the cameras.

The outermost strip-cord connectors, including C3 defined in Figure 4.3, are directly driven by the diagonal cords and their motion should be the easiest to predict, followed by the motion of the interior connectors. As an example, a comparison of the Cartesian coordinates of three strip-cord connectors is shown in Figure 4.5. The corresponding deviations in the absolute positions of the strip-cord connectors

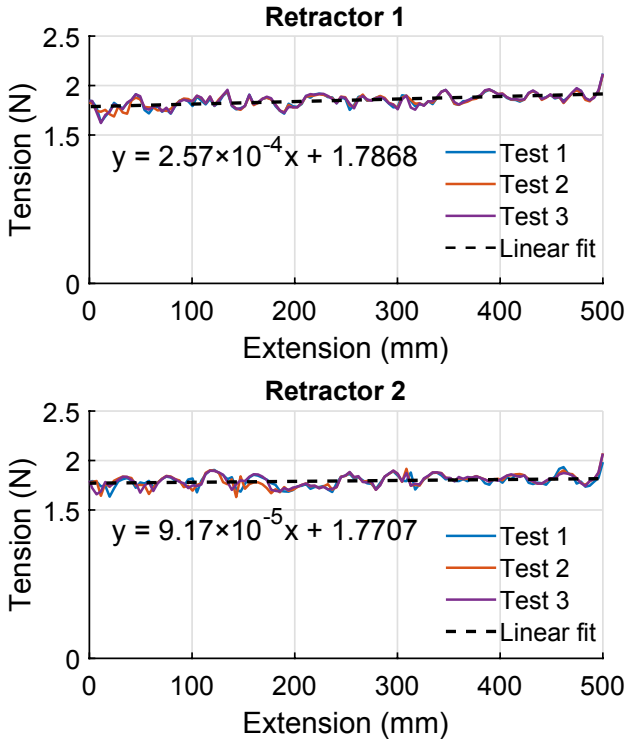

Figure 4.4: Tension forces in the cords of the two chosen retractors during retraction. Using linear approximation, constant force applied by the retractors are 1.79 N and 1.77 N. The mean value is used in the numerical simulations.

are presented in Tables 4.1. Position of a connector is the square root of the sum of squares of its x, y, and z coordinates. Relative error is defined as the ratio of the absolute difference between the values from experiment and simulation to the value from experiment.

It can be seen that the initial positions (at 0 s) of the connectors in the simulation are in good agreement with the experiment. The simulations estimate the motion of C3 with maximum error less than 3%. Although in the case of the innermost strip-cord connector C1, the simulations deviate further from the experiments, the mean deviation from the experiments is less than approximately 3% and the maximum error is less than 6%.

Table 4.1: Percentage of absolute deviation from experiments in distances from origin of the strip-cord connectors of the three-strip structure before 0.6 s.

Location	Mean (%)	Standard deviation (%)	Maximum (%)
C1	2.61	1.86	6.37
C2	1.40	0.90	3.23
C3	1.14	0.93	3.53

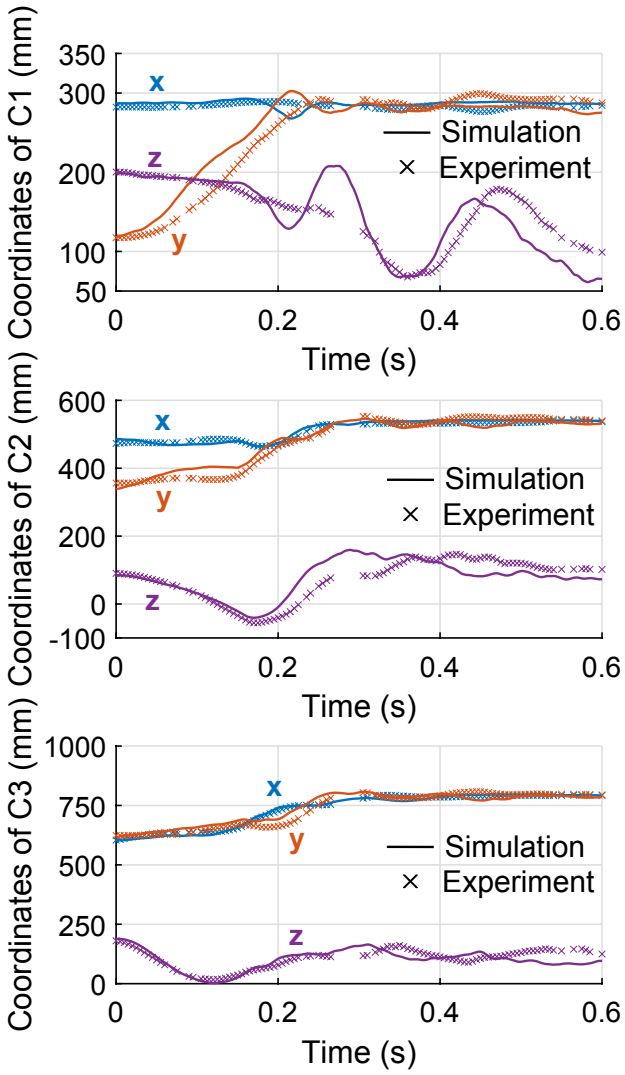

Figure 4.5: Simulation vs. experiment: comparison of the positions of the strip-cord connectors C1, C2, C3 from Strips 1, 2, 3, respectively.

Table 4.2: Percentage of absolute deviation from experiments in the fold angles of the three-strip structure before 0.6 s.

Longeron	Mean (%)	Standard deviation (%)	Maximum (%)
3	3.69	4.39	15.87
4	2.94	3.19	10.97
5	4.70	5.67	19.35
6	2.79	3.64	13.64

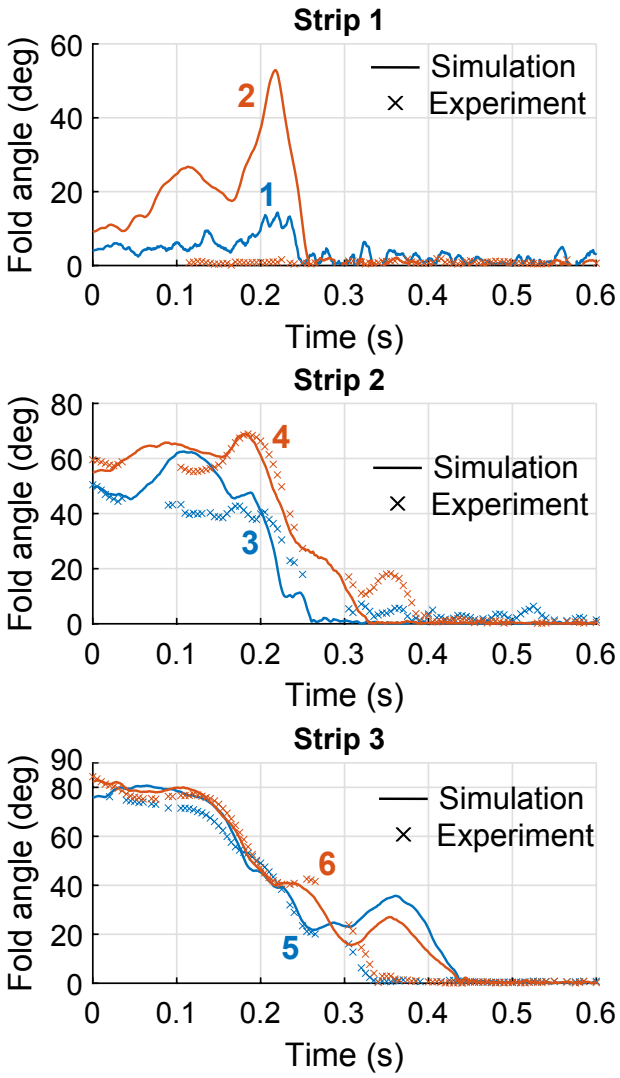

Figure 4.6: Simulation vs. experiment: comparison of the fold angles in the longerons. Longeron IDs as defined in Figure 4.3 are marked against the corresponding curves.

A significant deviation is observed in the prediction of maximum heights reached by the structure during deployment (Figure 4.7). Structure in simulation reaches higher vertical positions than that in experiment. This is because the interaction between the structure and the cylinder was not accurately captured in the simulation.The cylinder used in experiments has accessories at the top to allow it to be stowed and acted upon by the kickoff springs (as illustrated in Figure 3.3). These appendages protrude beyond the cylindrical surface and stop the structure from sliding off the cylinder for the first approximately 0.15 s of deployment. Hence the structure travels with the cylinder and does not reach higher vertical positions as expected. Although we attempted to model the protruding appendage on the cylinder in simulations, the structure-cylinder interaction was not captured entirely.

Although the lower deployment envelope observed in the experiment (as shown in Figure 4.7) may seem advantageous, it is important to note that the structure-cylinder interaction responsible for this result is not desirable. This interaction is not repeatable and may potentially cause material damage or result in a deployment failure.

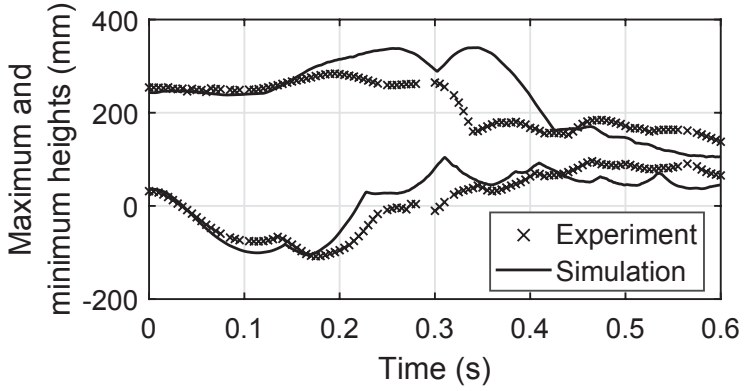

Figure 4.7: Simulation vs. experiment: comparison of deployment envelopes of the three-strip structure.

Table 4.3: Absolute deviation from experiments in the maximum and minimum heights reached by the three-strip structure before 0.6 s.

Quantity	Mean (mm)	Standard deviation (mm)	Maximum (mm)
Maximum height	42.30	46.22	181.78
Minimum height	25.61	19.52	100.97

4.5 Deployment of four-strip structure

To test the efficacy of the bonding technique proposed to build longer longerons (Figure 4.2), a deployment test was performed on a four-strip structure with the

maximum length of 2.2 m. Constant-force spring retractors (Figure 4.4) were used to guide the deployment, and two kickoff springs with stiffness approximately 15 N/mm each were used to increase the rotation speed of the cylinder.

The resulting deployment is depicted in Figure 4.8. It was noticed that no additional folds were created during the deployment, and the existing folds remain stationary in the middle of the respective longerons. This proves the efficacy of the proposed bonding technique, and demonstrates how the high-fidelity numerical simulations developed in Chapter 2 and the sensitivity studies explained in Chapter 3 helped improve the deployment mechanism.

To further test the simulation techniques developed in Chapter 4, the deployment of the four-strip structure was simulated in the commercial finite element software: Abaqus. A qualitative comparison of the deformation profiles between the experiment and the simulation are presented in Figure 4.8, and the quantitative comparisons are presented in Figures 4.9 and 4.10 and in Tables 4.4 and 4.5. The deviations in the predicted quantities from experiments were computed at all the time instants where the experimental data is available. The motion capture data of certain reflective markers becomes unavailable when they are not visible to the cameras.

The comparison metrics used to verify the numerical simulation against the experiment are the positions of the strip-cord connectors C1, C2, C3, and C4 defined in Figure 4.3, and the fold angles in the Strips 2, 3, and 4.

Position of a connector is the square root of the sum of squares of its x, y, and z coordinates. Relative error is defined as the ratio of the absolute difference between the values from experiment and simulation to the value from experiment. The absolute deviation in a fold angle from the experiment is defined as $|\theta^{sim} - \theta^{exp}|/(\pi - \theta^{exp})$, where θ^{sim} and θ^{exp} are fold angles from simulation and experiment, respectively.

The initial positions, at time $t = 0$, of the strip-cord connectors were predicted with an absolute error less than 4%, and the initial fold angles strips were predicted with absolute error less than 2%.

The simulation estimated the motion of C2, C3 and C4 with maximum error less than 5%. Although in the case of the innermost strip-cord connector C1, the simulation deviated further from the experiment, the mean deviation is less than 3.5% and the maximum error is less than 8% (Table 4.4).

Figure 4.8: Qualitative comparison of the deformation profiles of the four-strip structure during the deployment.

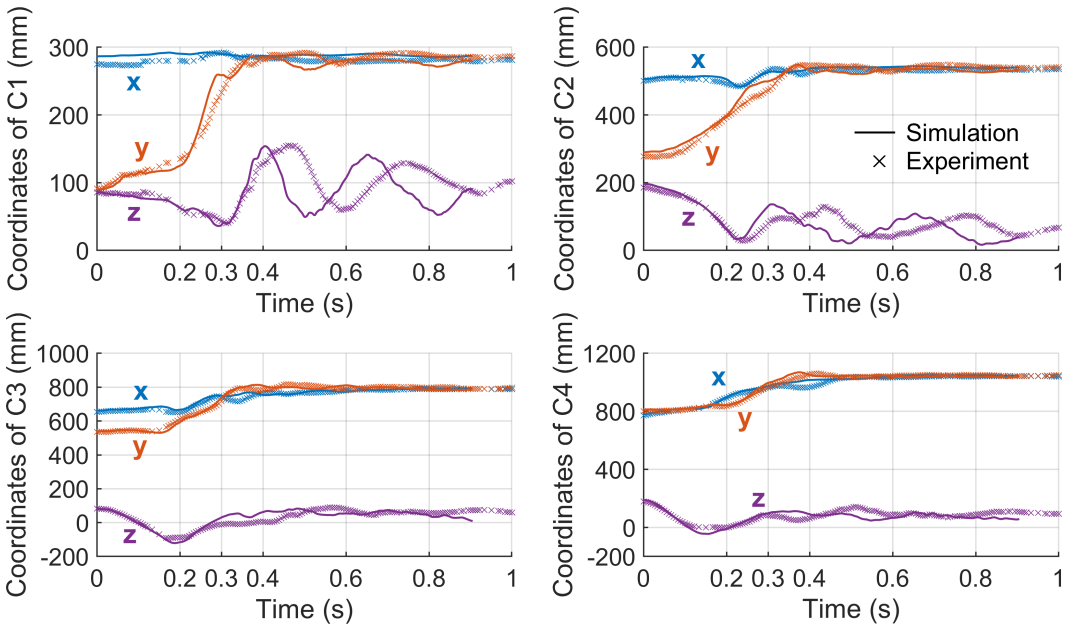

Figure 4.9: Simulation vs. experiment: comparison of the positions of the strip-cord connectors C1, C2, C3, and C4 from Strips 1, 2, 3, and 4 respectively.

Table 4.4: Percentage of absolute deviation from experiments in distances from origin of the strip-cord connectors of the four-strip structure before 0.9 s.

Location	Mean (%)	Standard deviation (%)	Maximum (%)
C1	3.33	1.85	7.19
C2	1.65	0.89	4.01
C3	0.88	0.73	3.11
C4	0.88	0.95	4.04

The deformation profiles predicted by the simulation look similar to those from the experiment until 0.3 s of the deployment (Figure 4.8). The deviation is larger after this instant because, in the experiment, Longeron 6 of Strip 3 snagged against the cylinder which had reached its final position. The consequences of this interaction are reflected in the differences in the time periods of the oscillations of the z-coordinates of the strip-cord connectors (Figure 4.9) as well as the differences in the evolution of the fold angles (Figure 4.10 and Table 4.5).

Another major difference between the simulation and the experiment is the time taken for the longerons to latch into their flat configurations (where fold angle $\theta \approx 0°$). While in the experiment, the longerons of Strips 3 and 4 latch at approximately the same time, the same is not true in the simulation (Figure 4.10). This could be a consequence of the structure-cylinder interaction not being predicted accurately in the simulation.

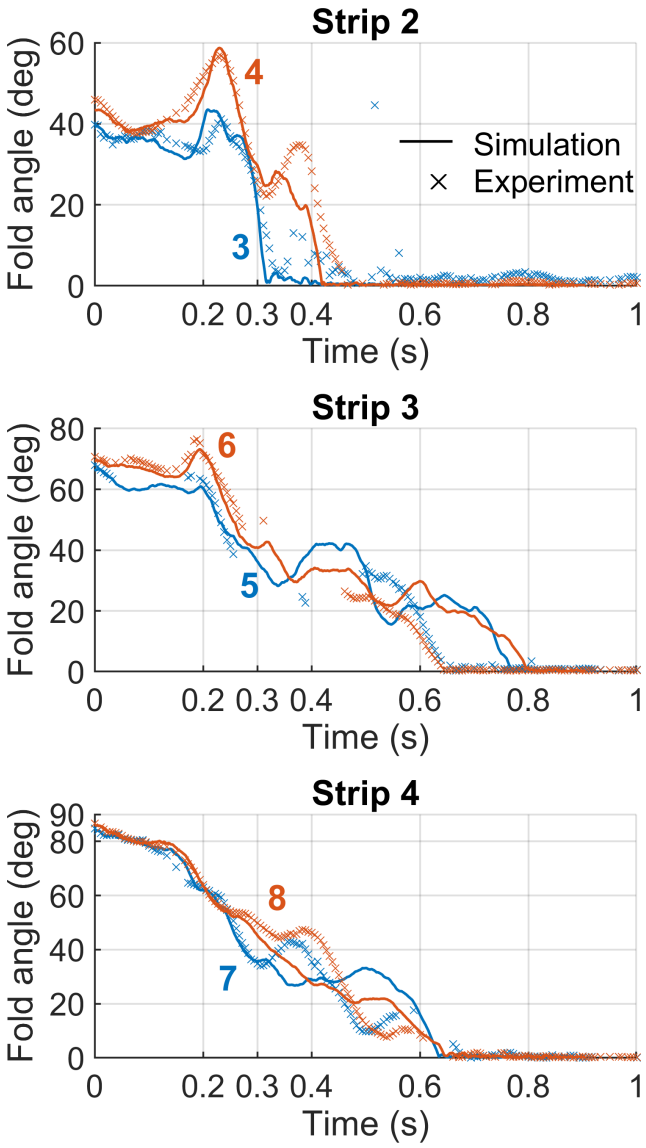

Figure 4.10: Simulation vs. experiment: comparison of the fold angles in the longerons of the four-strip structure. Longeron IDs as defined in Figure 4.3 are marked against the corresponding curves.

Table 4.5: Percentage of absolute deviation from experiments in the fold angles of the four-strip structure.

	Before 0.9 s			Before 0.3 s		
Longeron	Mean (%)	Standard deviation (%)	Maximum (%)	Mean (%)	Standard deviation (%)	Maximum (%)
3	1.45	1.39	6.89	1.44	1.31	6.08
4	1.68	2.59	10.80	1.29	1.14	4.24
5	4.24	4.24	13.58	1.77	1.42	4.76
6	4.06	3.73	11.43	2.19	1.26	4.72
7	3.01	4.12	13.75	1.14	1.03	4.12
8	2.80	3.64	14.01	0.96	0.79	3.48

4.6 Conclusions

In the previous chapter, it was established that by choosing appropriate initial conditions, no additional elastic folds will be formed in the longerons during the deployment and the existing folds remaining stationary in the middle of the respective longerons. In this chapter, this property was exploited to build longer longerons by bonding multiple TRAC longerons together using epoxy. The efficacy of this method was verified by performing deployment tests using a four-strip SSPP structure. The deployment proceeded as desired (no additional folds and existing folds remain stationary) implying that the proposed method can be used to build SSPP structures of any desired size.

The efficiency of the high-fidelity numerical simulation techniques laid out in Chapter 2 were further put to test by simulating the deployments of a three-strip and a four-strip structure and comparing the behaviors against the experiments. Constant-force spring retractors were employed to guide the deployment, and kickoff springs were utilized to increase the rotation speed of the cylinder. In both cases, positions of the strip-cord connectors were predicted with maximum absolute errors less than 7.2%. The larger deviations in the fold angles from the experiments were primarily due to the inaccurate estimation of the interaction between the structure and the cylinder appendages. This implies a need for a better design of the cylinder assembly.

Chapter 5

ISOGEOMETRIC ANALYSIS FOR QUASI-STATIC GEOMETRICALLY NONLINEAR PROBLEMS

This chapter was modified from the following publication.

N. H. Reddy and S. Pellegrino, "Time-efficient geometrically non-linear finite element simulations of thin shell deployable structures," in *AIAA SciTech 2021 Forum*. 2021, p. 1795. DOI: 10.2514/6.2021-1795,

5.1 Introduction

Thin-shell structures have unique properties and are widely used in many fields, including architecture and aerospace [30]. They have been studied extensively over many years [36], with much emphasis placed on studies of their initial buckling and post-buckling. Recently, there has been an increasing number of studies and engineering applications in which the post-buckling behavior of thin shells is the key to achieving certain specific features [37], [38]. Examples include energy dissipating dampers [39], [40], actuators [41], [42], deployable [43]–[45] and morphing structures [46], [47]. These applications require extensive, highly geometrically non-linear simulations and the computational effort for design optimization is currently beyond reach. Enabling further developments in these areas requires new, faster computational tools and hence this study assesses the performance of one of the latest developments in computational structural mechanics, NURBS-based thin-shell finite elements, for deployable structures.

For background, it should be noted that the properties of thin-shell structures are very sensitive to geometric imperfections [48] and the standard finite element approximation of a curved shell geometry introduces geometric imperfections because the spatial discretization is inherently inaccurate unless mid-side nodes are placed on the shell surface. Standard thin-shell finite elements are based on Reissner-Mindlin kinematics and use Lagrange polynomial shape functions [49]. They provide C^0-continuous displacement fields (with slope discontinuities along the element boundaries) and make discretization errors inevitable. Finer meshes are needed to reduce the effects of these errors, which leads to higher computational costs.

The recently developed isogeometric analysis [50] has been shown to provide a better

approximation for the analysis of shell structures, as it uses the same functions to approximate both the geometry of the shell and its deformation. Irrespective of the size of the mesh, the initial geometry of the shell can be defined accurately, even for sparsely defined nodal variables, thus greatly reducing the errors related to shape discretization. The shape functions—B-Splines, Non-Uniform Rational B-Splines (NURBS) or other parametrizations used in CAD—naturally span across multiple knot intervals (or 'elements') maintaining inter-element continuity which can be easily extended to slope (C^1-) and curvature (C^2-) continuous shape functions. An early development of a shell element formulation based on isogeometric analysis was [51], followed by many additional studies [52]–[57]. Despite the use of smooth, high-order shape functions, NURBS-based shell elements are not free from locking, although there have been successful attempts to avoid geometrical locking effects at the theory level [58], [59].

Previous authors have noted the advantages of isogeometric analysis to analyze the buckling of plates and shells [60]–[63]. These studies have shown that NURBS-based analysis achieves convergence with fewer degrees of freedom, however so far there has been no comparison of the computational effort that is required when NURBS-based elements are used for geometrically nonlinear problems such as folding simulations. This research fills this gap by studying the quasi-static nonlinear bending of a tape spring—a longitudinally straight and transversely curved strip of uniform thickness—that is the prototypical thin-shell deployable structure, capable of elastic folding, self-deployment and latching [64]–[66].

Tape springs can be bent longitudinally to form localized elastic folds. If the bending is in the sense opposite to the original transverse curvature, the tape spring undergoes a sudden snap-through buckling that results in the formation of a localized fold. When the bending is in the same sense as the transverse curvature, the fold formation occurs gradually, through a combination of bending and torsional deformation [67]. In both cases, the elastic fold is bounded on either sides by relatively undeformed regions of the tape spring. When it is released from a folded configuration, the tape spring returns to its straight, undeformed configuration. Owing to the simplicity of their geometry, repeatable self-actuation, and ease of manufacturing, tape springs have found several applications in aerospace engineering [43], [64], [65], [67]–[70].

The present study focuses on the simulation of the opposite sense bending of an isotropic tape spring whose cross-section forms a circular arc, using both NURBS-based and bilinear shape functions finite elements. Convergence analyses are per-

formed for both types of elements and the CPU times required for an accurate simulation of the nonlinear moment-rotation relationship are compared. In an additional comparison, high aspect ratio meshes are used to model the less deformed regions of the tape spring, on either side of the elastic fold. This targeted meshing significantly reduces the number of variables and computational resources required to achieve convergence. Both of these comparisons show that NURBS-based isogeometric analysis converges with fewer variables but is computationally more expensive.

The chapter is organized as follows. Section 5.2 provides a brief outline of the two formulations for thin shells, and discusses the commercial finite element software used for the study along with the elements and solvers used. Section 5.3 presents the specific tape spring chosen for the present study and discusses the applied boundary conditions. Sections 5.4 and 5.5 present the results obtained from simulations carried out with uniformly-sized bilinear and NURBS-based elements, respectively. Section 5.6 presents the results obtained with high aspect ratio meshes in the less deformed regions of the tape spring. Section 5.7 concludes the chapter.

5.2 Background

This section presents a short introduction to the thin-shell finite elements and solvers in the commercial finite element package LS-DYNA that were used for the present study.

Bilinear finite elements versus higher-order NURBS elements

Isogeometric analysis derives its name from the use of the same shape functions to approximate the initial geometry of the model and also for the finite element discretization. NURBS, the most commonly used shape functions, allow an exact description of conical sections irrespective of the size of the finite element mesh. On the other hand, bilinear finite elements provide a faceted representation of the actual geometry.

This difference is shown in Figure 5.1 for the case of a cylindrical surface. Figure 5.1(a) shows the finite element discretization of the surface using C^0-continuous bilinear elements and Figure 5.1(b) shows the exact representation of the surface using biquadratic, C^1-continuous NURBS elements. In both of these meshes, four elements are used in the longitudinal and circumferential directions, although one NURBS element would be sufficient in Figure 5.1(b). The corresponding linear polynomial shape functions and the quadratic B-Spline polynomials in one of the parametric directions for one of the internal elements are shown in Figure 5.1(c)

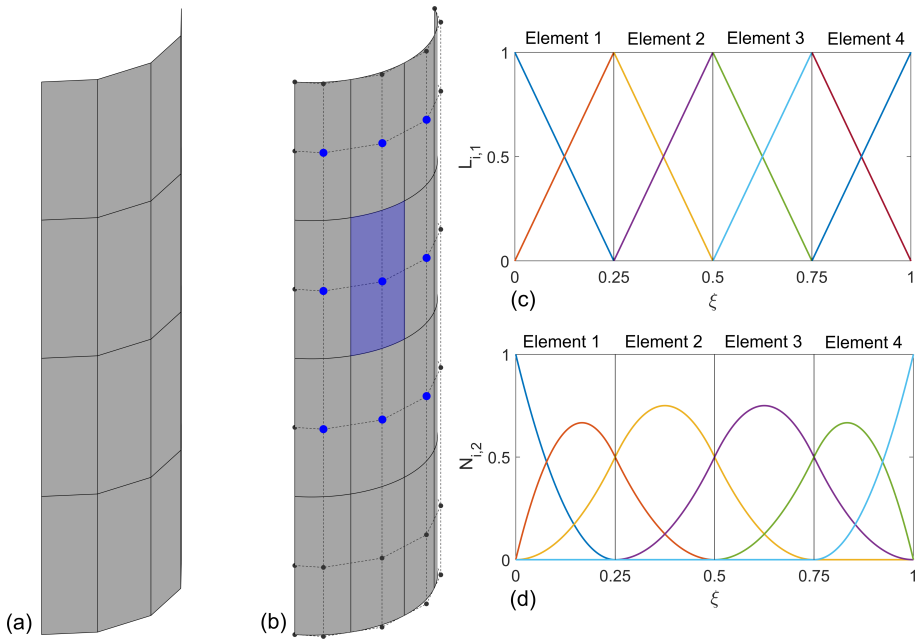

Figure 5.1: Finite element discretizations of a cylindrical surface using a 4×4 mesh of (a) bilinear elements and (b) biquadratic NURBS elements. The dots represent the control points; the element shaded in blue has support from nine control points, shown as blue dots. (c) Bilinear basis functions and (d) quadratic B-Spline basis functions with the knot vector $\Xi = \{0, 0, 0, 0.25, 0.5, 0.75, 1, 1, 1\}$, in one of the parametric directions ξ.

and 5.1(d), respectively.

Notice that the B-Spline polynomials span across more than one element, ensuring higher-order inter-element continuity as opposed to the linear polynomials that offer only C^0-continuity. Each bilinear element is supported by two basis functions in each direction, and hence needs four nodes in total. In contrast, each biquadratic element is supported by three basis functions in each of the parametric directions, see Figure 5.1(d), and hence there are nine control points in total. Also note that all of the nodes supporting the bilinear element lie on the element boundaries whereas the control points supporting the NURBS element do not lie on the surface.

It must also be noted that, despite the mentioned differences in the kinematic formulation of these elements, the rest of the finite element formulation can be essentially the same.

Isoparametric finite element analysis

In isoparametric formulation, the same interpolating functions are used to define the element geometry as well as the unknown field (e.g., displacements). For example,

the position of a point within a 2D element e is defined as

$$\mathbf{x}^e(\xi,\eta) = \sum_{a=1}^{n_{en}} L_a^e(\xi,\eta)\mathbf{P}_a^e, \tag{5.1}$$

where L_a^e is the Lagrange polynomial shape function and $\mathbf{P}_a^e$ is the position of the node associated with the basis function index a. ξ and η represent the natural coordinates of the point, and n_{en} is the number of basis functions supporting the element. For example, a 4-node quadrilateral element is supported by 4 basis functions (n_{en}= 4). The unknown variable at this point $u(\xi,\eta)$ is approximated in a similar fashion as

$$\mathbf{u}^e(\xi,\eta) = \sum_{a=1}^{n_{en}} L_a^e(\xi,\eta)\mathbf{d}_a^e, \tag{5.2}$$

where $\mathbf{d}_a^e$ are the nodal variables. Linearization of the equilibrium equations over the element gives the following system of equations.

$$\mathbf{K}^e\mathbf{u} = \mathbf{f}^e, \tag{5.3}$$

where $\mathbf{K}^e$ is the element stiffness matrix of size $n_{en}n_{dof} \times n_{en}n_{dof}$, $\mathbf{u}$ is the vector of nodal variables of size $n_{en}n_{dof} \times 1$, and $\mathbf{f}^e$ is the nodal force vector. n_{dof} is the number of degrees of freedom per node.

Isogeometric analysis uses this isoparametric concept but with different basis functions—those used in CAD modeling to generate the geometry. A brief introduction to NURBS-based analysis is presented in the following.

Important details about NURBS-based elements

Given a set of control points $\mathbf{P}_i$ (i = 1 to n) and corresponding weights w_i, an approximating NURBS curve is defined as

$$\mathbf{C}(\xi) = \sum_{i=1}^{n} R_{i,p}(\xi)\mathbf{P}_i, \tag{5.4}$$

where the rational polynomial basis functions are defined as

$$R_{i,p}(\xi) = \frac{w_i N_{i,p}(\xi)}{\sum_{i=1}^{n} w_i N_{i,p}(\xi)}, \tag{5.5}$$

and the B-Splines $N_{i,p}$ of polynomial degree p are constructed from the Cox de Boor formula [71] for a given knot vector $\Xi = \{\xi_1 = 0, \ldots, \xi_i, \ldots, \xi_{n+p+1} = 1\}$ (with $\xi_i \leq \xi_{i+1}$).

For example, rotation-free biquadratic elements ($p = q = 2$) with 3 degrees of freedom are supported by $(p + 1) \times (q + 1) = 9$ basis functions and the size of the element stiffness matrix is 27×27.

The knot vector Ξ is termed *open* or *clamped* if the first and last knots are repeated $p+1$ times. In such a situation, the approximating curve passes through the first and last control points as well as being tangent to the control polygon at these points. This facilitates the application of displacement and slope boundary conditions. The B-Spline basis functions are C^{p-k} continuous at a knot of multiplicity k ($k = 1$ at the interior knots, in the present study), and hence continuity at a knot can be easily controlled by repeating that knot.

The following aspects of NURBS-based isogeometric analysis are particularly relevant to the present study.

(i) The control points do not necessarily lie on the actual surface, but open knot vectors are used to ensure that the surface passes through the control points along the edges of the model.

(ii) Non-zero knot spans are defined as 'elements' and their control points are defined as 'nodes'.

(iii) The degrees of freedom of the model are defined at the control points, and the boundary conditions are applied at these points. Purely displacement-based or rotation-free shell elements are used in this study.

(iv) Gauss quadrature is employed for numerical integration at the element level. Full integration uses $(p+1)\times(q+1)$ integration points while uniformly reduced integration uses $p \times q$ integration points. Fully integrated shell elements are likely to suffer from geometrical locking effects such as shear and membrane locking.

Software description

Simulations of the end-rotation-controlled, opposite-sense bending of an isotropic tape spring were carried out with the commercial finite element software LS-DYNA.

*Control_Implicit_Auto					
IAUTO	ITEOPT	ITEWIN	DTMIN	DTMAX	
1	25	20	0.01	1.0	
*Control_Implicit_General					
IMFLAG	DT0	FORM			
1	0.05	0			
*Control_Implicit_Solution					
NSOLVR	ILIMIT	MAXREF	DCTOL	ECTOL	DNORM
12	21	25	0.0001	0.001	1

Table 5.1: Parameters used for the keyword *Control in the LS-DYNA implicit simulations. Default values were used for any parameters not listed here.

Quasi-static finite element simulations were performed using LS-DYNA (version R11.1) type-16 shell elements, recommended by the developers for implicit simulations. This element, also denoted as *ELFORM=16*, is a 2×2 integrated planar element with assumed strain interpolation to alleviate locking. It has five degrees of freedom per node in the local coordinates.

NURBS-based isogeometric analysis is available in LS-DYNA through the keyword *Element_Shell_Nurbs_Patch. A surface may be both modeled and meshed with NURBS-based elements, and there is the option of using the LS-DYNA user interface or to import a NURBS patch in .iges format. The latter was done in this study using an open source toolbox [72]. The elements are rotation-free and use a Reissner-Mindlin shell formulation with kinematics based on a degenerated solid approach developed by [73]. Both full and uniformly reduced Gauss integration were investigated.

For all of the simulations, the Broyden-Fletcher-Goldfarb-Shanno (BFGS) quasi-Newton solver with automatic incrementation and without arc-length control was used. LS-DYNA offers many control options for the solver and numerous control parameters must be chosen. The parameters that worked for all simulations presented in this study are listed in Table 5.1. The default values were used for any parameters not listed in the table. All solution control parameters and boundary conditions were unchanged throughout the study.

The keyword files were compiled in double precision (note that LS-DYNA implicit does not support single precision) in LS-Run on a 12-core, 24-thread Intel Xeon X5680 @3.33 GHz, using a single CPU.

5.3 Case study

A tape spring is a longitudinally straight cylindrical shell with a circular arc cross-section, as shown in Figure 5.2(a). The ends of the tape spring are assumed to be attached to rigid plates, which prevent any cross-sectional deformation. When the end plates are rotated about axes perpendicular to the plane of symmetry of the structure (shown in Figure 5.3(a)), such as to impose a relative rotation θ between the end sections, initially the tape spring exerts monotonically increasing bending moments M, as shown in Figure 5.2(b), until a dynamic snap occurs and the moments suddenly decrease. At this point, an elastic fold forms and the bending moment becomes constant for further increases of θ, as shown schematically in Figure 5.2(c). In effect, the tape spring behaves like a constant-moment elastic hinge. Note that the tape spring undergoes small strains although the rotations are large.

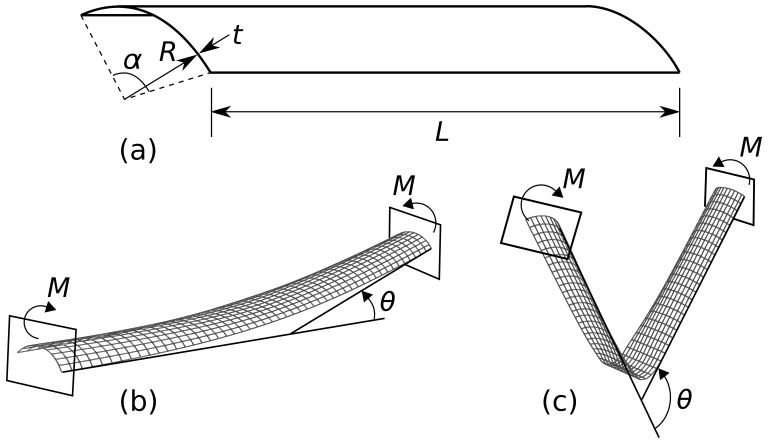

Figure 5.2: Case study. (a) Schematic of tape spring of length L, radius of cross-section R, thickness t and subtended angle α. (b) Tape spring under opposite sense bending, and (c) schematic of post-snap-through configuration with elastic fold in the middle.

The geometric properties (defined in Figure 5.2(a)) and the material properties (Young's modulus E and Poisson's ratio ν) of the specific tape spring that was studied are listed in Table 6.1.

L	R	t	α	E	ν
200 mm	10 mm	0.1 mm	110°	131 GPa	0.3

Table 5.2: Properties of tape spring chosen for the case study.

Instead of rotating both end plates, a set of simple and yet equivalent boundary conditions were chosen. The right-hand plate was fully clamped and the left-hand

plate was rotated through a clockwise rotation of magnitude θ, as indicated in Figure 5.3(a).

A reference point (massless node) RP (in Figure 5.3) was introduced at the intersection of the centroidal axis of the tape spring, in the initial configuration, and the end cross-sectional plane. All the nodes (or control points) at this cross-section were kinematically constrained to RP using the keywords *`Extra_Nodes_Set` or *`Constrained_Nodal_Rigid_Body`. Therefore, the rigid body translation and rotation of the left-end of the tape spring are controlled by RP.

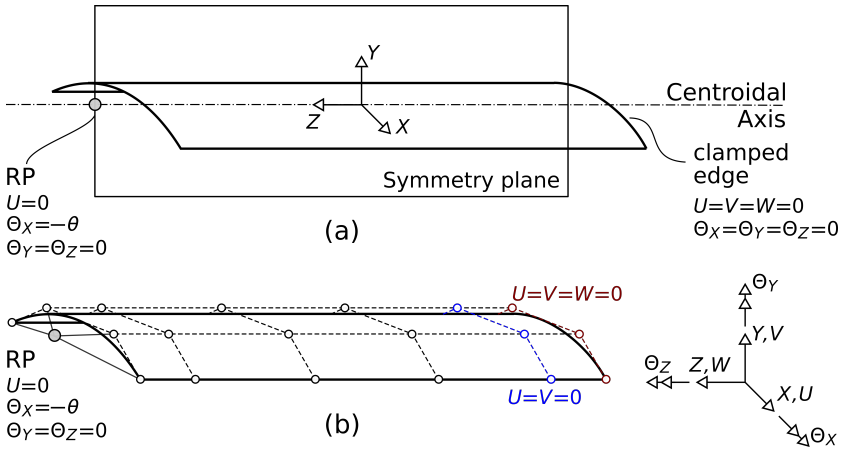

Figure 5.3: Boundary conditions for (a) bilinear finite elements, and (b) rotation-free NURBS-based elements. Nodes at the left end are kinematically constrained to the reference point RP.

Although only translational degrees of freedom are defined at the control points in isogeometric analysis, it should be noted that rotational degrees of freedom were defined at the reference point.

When an open knot vector is used in one of the parametric directions, the NURBS surface is tangent to the control net (matrix of control points, i.e., the faceted surface represented by dashed lines in Figure 5.3(b)) at both ends, in that direction [50]. This property was exploited in applying the fully clamped boundary condition shown in Figure 5.3. The reaction moment M around the X-axis, at the clamped end, was computed from the nodal reaction forces in the Z-direction.

Under static equilibrium conditions, the moments at the two ends are equal in magnitude and in opposite directions.

Mesh size	Degrees of freedom	CPU time (s)
30×15	2480	16
40×15	3280	**23**
50×15	4080	34
100×20	10605	187

Table 5.3: CPU times for LS-DYNA implicit simulations with shell type-16 elements. The best converging result is highlighted in bold.

5.4 Simulations with bilinear finite elements

This section presents the results obtained from the LS-DYNA simulations using uniform meshes of 4-node, bilinear type-16 shell elements described in Section 5.2.

Figure 5.4 presents the results of the convergence analysis that was performed. The resisting moment M increases with the applied rotation θ until a peak moment of about 300 Nmm is reached at a rotation $\theta \approx 12.5$ deg. After going past this limit point, the tape spring undergoes dynamic buckling, leading to the formation of an elastic fold, which offers a steady resistance of approx. 29 Nmm across the range $\theta = 12.5 - 50$ deg.

Figure 5.4(a) shows the M vs. θ relationship for four uniform meshes in which the number of longitudinal elements increases from 30 to 50 and the number of circumferential elements is equal to 15. A reference solution with 100 elements longitudinally and 20 elements circumferentially (labelled 100×20) is also presented. Note that these simulations do not track the unstable behavior after the limit point, and hence a sharp fall in the moment M is predicted. The full equilibrium curve can be traced with an arc-length solver, and further details can be found in [65]. Note that the results converge for a uniform mesh of 40×15 elements. Figure 5.4(b) examines the sensitivity of this result to the number of circumferential elements, and shows that 15 elements are sufficient for convergence.

The CPU times for the simulations presented in Figure 5.4(a) are listed in Table 5.3. A comparison of these results to those obtained from NURBS-based elements will be provided in the next section.

5.5 Simulations with NURBS-based elements

The NURBS-based elements were defined with open knot vectors, with the multiplicity of all interior knots set to 1. Therefore, the degrees of continuity at the interior knots were C^{p-1} and C^{q-1} in the directions with polynomial degrees p and q, respectively.

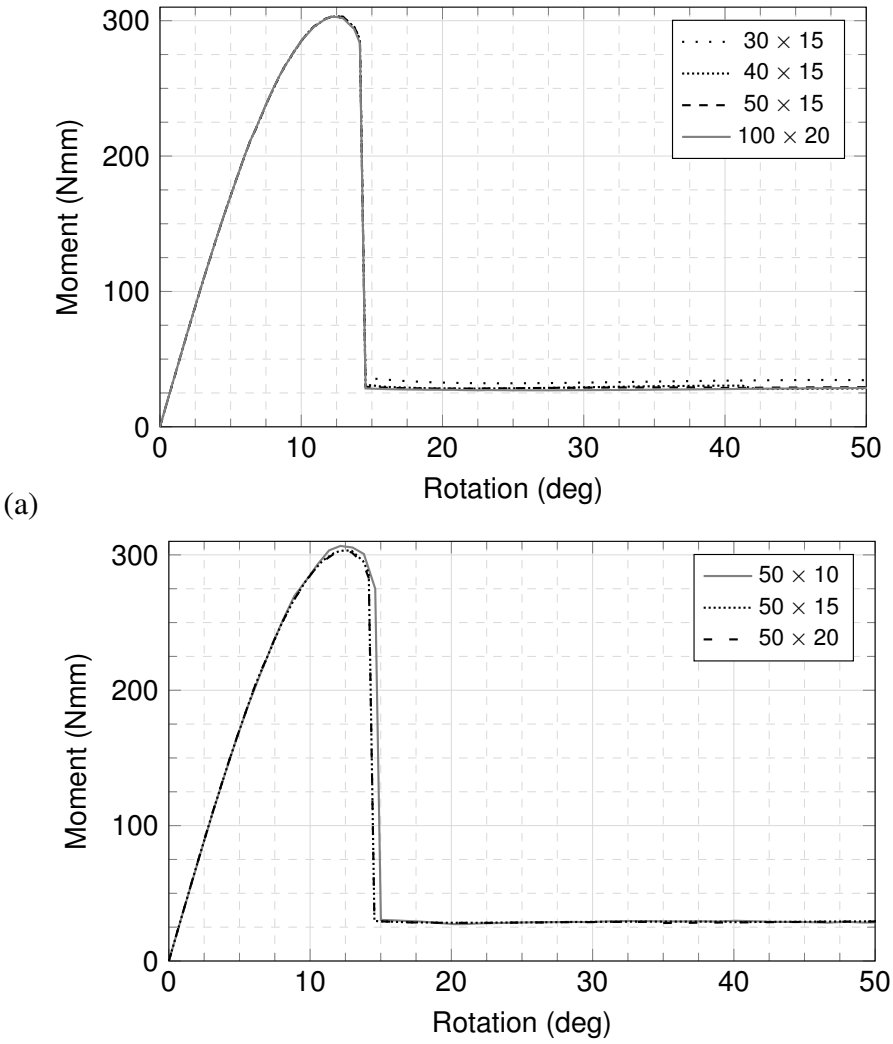

Figure 5.4: Convergence analysis using LS-DYNA type-16 shell elements. $m \times n$ refers to m and n uniformly distributed elements in the longitudinal and circumferential directions, respectively. Results for different numbers of elements in (a) longitudinal direction and (b) circumferential direction.

Note that if linear B-Splines had been used to construct the NURBS surface, the continuity at the interior knots would have been C^0 and the surface would have passed through all of the control points. In addition, all of the control points would have lied on the element boundaries, leading to a faceted model of the curved surface which would have not provided an exact geometric representation of the tape spring.

The tape spring was meshed with either biquadratic ($p = q = 2$) or bicubic ($p = q = 3$) elements, uniformly distributed over the surface. A fully integrated element has $(p+1) \times (q+1)$ integration points and uniformly reduced integration implies $p \times q$ integration points. Note that, while the elements are uniformly spaced, the control points are not, as shown in Figure 5.3(b). Also note that, although a single element would be sufficient to describe exactly the initial geometry of the tape spring, a larger number of elements is needed to accurately predict the complex deformed shapes, see Figure 5.5.

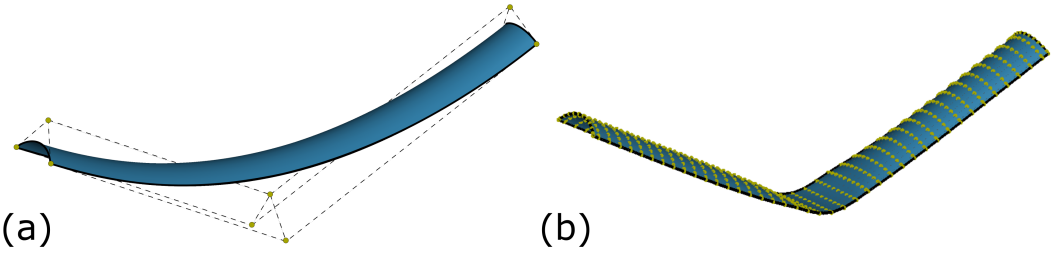

Figure 5.5: Deformed shapes of tape spring at a rotation of $\theta = 0.9$ rad, for the biquadratic NURBS mesh of size (a) 1×1 and (b) 40×10. The circles connected by dotted lines represent the control points (or nodes). While the 1×1 mesh can represent the undeformed geometry exactly, it would not predict buckling and fold formation.

Figure 5.6 presents the moment-rotation curves obtained with biquadratic NURBS-based elements. Discretizing the arc with only 10 quadratic elements independently of the number of elements along the length, Figure 5.6(a), leads to a stiffer response indicating membrane locking. This was eliminated by using a finer discretization in the circumferential direction or by reduced integration, Figure 5.6(b), or by using higher order splines, Figure 5.7.

Figure 5.6(b) shows that 10 elements along the arc and 100 elements along the length are sufficient for convergence, however, 50 elements in the length direction result in an oscillating response in the post-buckling regime (the reasons are not known). Since the maximum deviation from the reference steady-state moment with respect to the peak moment is only 2%, it can be assumed that convergence has

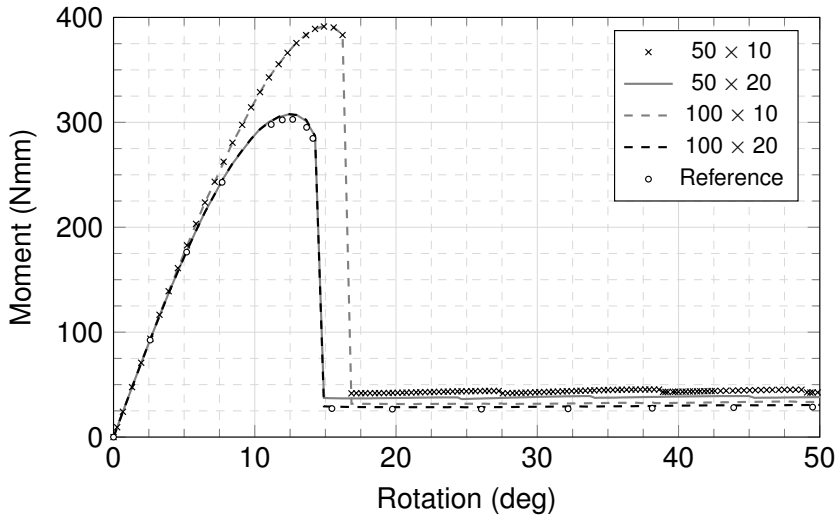

(a)

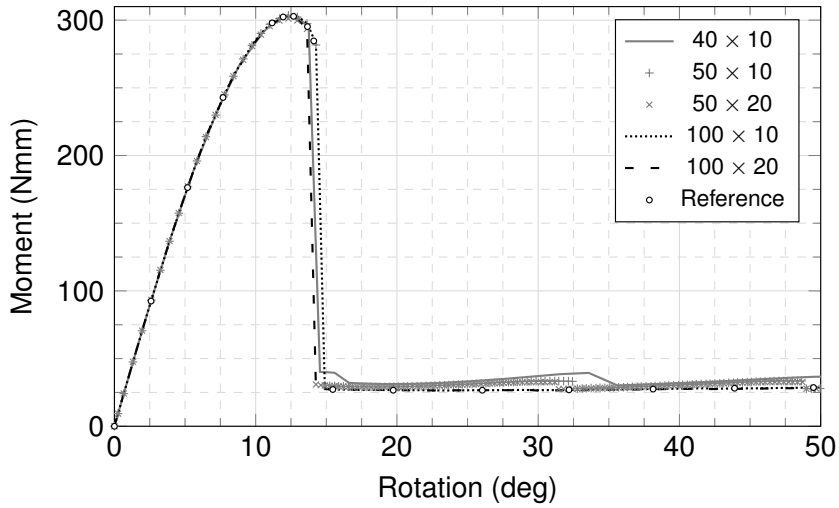

(b)

Figure 5.6: Convergence analysis using (a) fully integrated and (b) reduced integration biquadratic NURBS. $m \times n$ refers to m and n uniformly distributed elements($(m + 2)$ and $(n + 2)$ control points) in the longitudinal and circumferential directions, respectively.

been achieved with 50×10 meshes. The same oscillation is seen also in Figure 5.7 for the C^2-continuous bicubic elements, except for meshes with 100 elements along the length. For these elements, the maximum deviation from the reference is approx. 2.5% and hence it is assumed that convergence is achieved with a 50×10 mesh.

The CPU times for these analyses are presented in Table 5.4. Note that the reduced integrated elements are computationally less expensive in almost all cases and, therefore, the following discussion focuses only on the results obtained with reduced integration elements. Also note that the number of Gauss points is equal to 4 for both the type-16 shell elements and the reduced integration biquadratic NURBS elements.

Mesh size	Degrees of freedom	CPU, full integration	CPU, reduced integration
Biquadratic NURBS ($p = q = 2$)			
50×10	1873	81 s	**76 s**
50×20	3432	173 s	143 s
100×10	3672	250 s	200 s
100×20	6732	533 s	409 s
Bicubic NURBS ($p = q = 3$)			
50×10	2067	176 s	**147 s**
50×20	3657	379 s	301 s
100×10	4017	363 s	459 s
100×20	7107	1003 s	838 s

Table 5.4: CPU times for LS-DYNA simulations with NURBS meshes. The best converging results are highlighted in bold.

The CPU times for the converging solutions were 76 s and 147 s for reduced integration biquadratic and bicubic elements, respectively. Comparing these times with the CPU time of 23 s for the 40×15 mesh of type-16 shell elements, see Table 5.3, the NURBS-based simulations were, respectively, 3.3 and 6.4 times more expensive. Although the NURBS-based elements converged with fewer degrees of freedom, 1873 for biquadratic elements vs. 3280, they are computationally more expensive.

An explanation is that the global stiffness matrices in isogeometric analysis are less sparse than the stiffness matrices in standard finite element analysis because the element stiffness matrices are bigger. For example, a biquadratic NURBS-based element used here has a stiffness matrix of size 27×27 while the type-16 shell element has a local stiffness matrix of size 20×20.

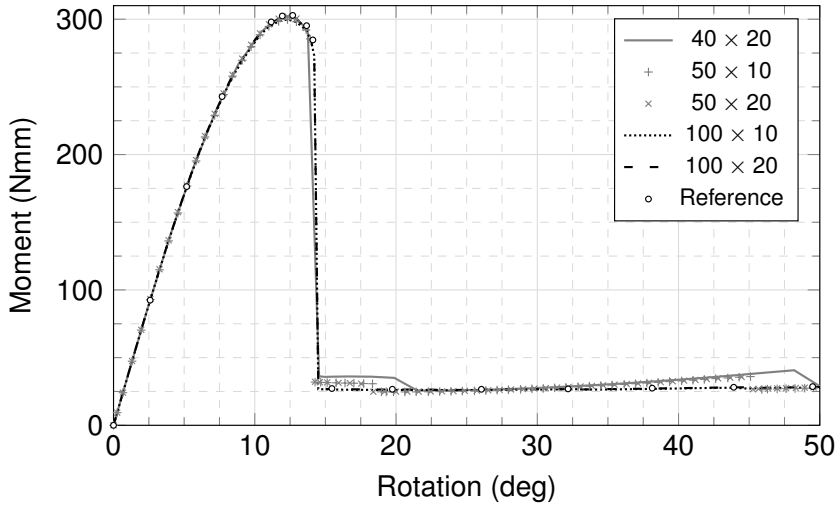

(a)

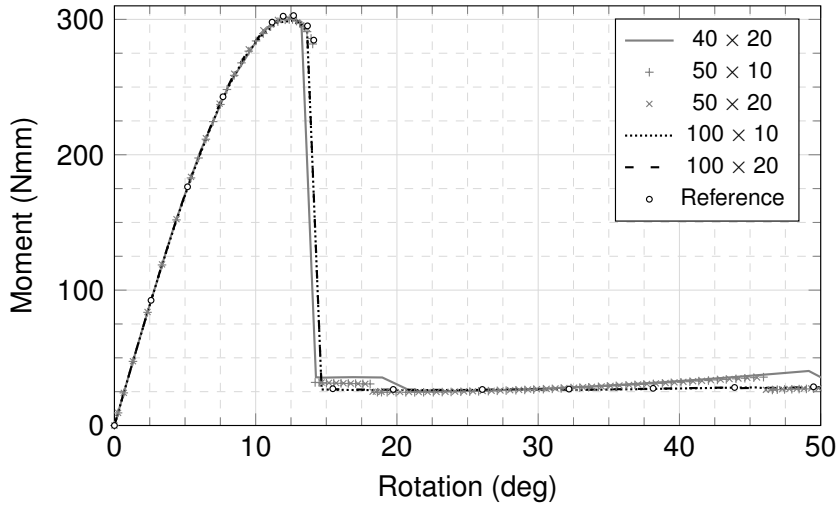

(b)

Figure 5.7: Convergence analysis using (a) fully integrated and (b) reduced integrated bicubic NURBS. In the legends, $m \times n$ refers to m and n uniformly distributed elements (($m+3$) and ($n+3$) control points) in the longitudinal and circumferential directions, respectively.

5.6 High aspect ratio elements

The mesh design can be targeted to the problem in hand by noticing that, because snap-through buckling occurs in the middle of the tape spring, a fine mesh is not necessary in the outer parts of the tape spring. Hence, computational resources can be saved by coarsening the mesh, i.e., using high aspect ratio elements in these regions. To quantify the improvement that can be achieved in this way, the tape spring was partitioned as shown in Figure 5.8. The two regions that span 80 mm from the end cross-sections are denoted as region 2 and the middle region, where the fold is expected to form, is denoted as region 1. Note that the length of 40 mm for the middle region is sufficient for a fully formed 180° fold to form without going beyond the finely meshed region 1, see Figure 5.9.

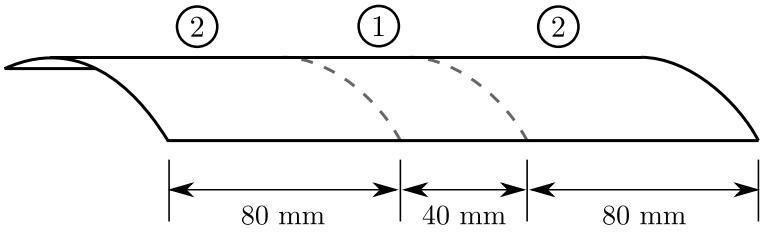

Figure 5.8: Partitioned tape spring. The number of elements along the arc is denoted by n, the numbers of elements along the length in regions 1 and 2 are denoted by m_1 and m_2, respectively.

The performance of meshes with highly elongated elements was studied with the number of elements in the circumferential direction, n, kept constant while varying the number of elements along the length. The number of elements in the longitudinal direction in region 1 is denoted by m_1 and the number in each region 2 is denoted by m_2. The total number of elements will then be $(m_1 + 2m_2) \times n$ and all elements within each region have uniform size.

Figure 5.10(a) presents the moment-rotation plots for NURBS meshes with polynomial degrees $p = q = 2$, $n = 10$, $m_1 = 10$ and varying m_2. This particular choice of n results from the observation made in Section 5.5, that 10 elements along the arc are sufficient to accurately predict the moment-rotation relationship. Setting $m_1 = 10$ means that each element in region 1 is 4 mm long, which matches the case in Section 5.5 where a 50×10 biquadratic NURBS mesh led to a converging solution (see Figure 5.6(b)). As the number of elements in region 2 is reduced, the predicted response tends to become stiffer. Note that m_2 can be as low as 5, corresponding to 16 mm long elements for a reasonably accurate solution. This particular simulation requires 28 s of CPU time, see Table 5.5.

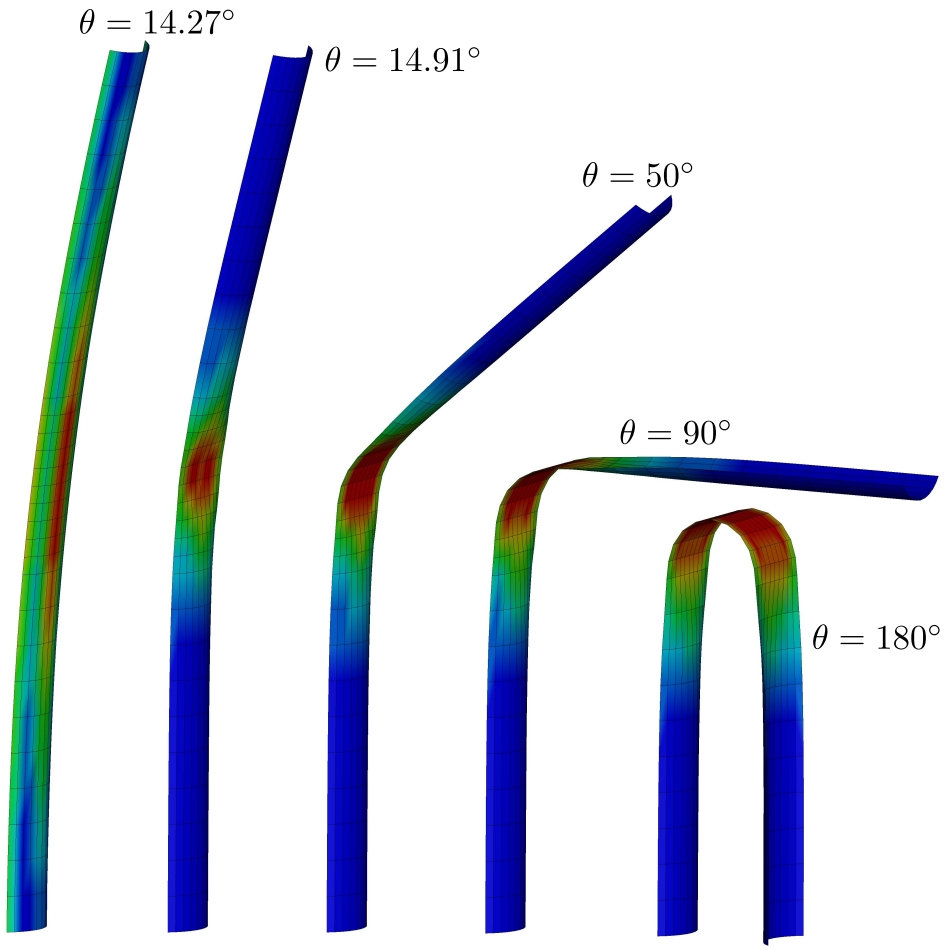

Figure 5.9: Deformed profiles of the tape spring for the rotations 14.27°, 14.91°, 50°, 90°, and 180°. The solid lines on the surface represent the biquadratic NURBS mesh with $n = 10$, $m_1 = 10$ and $m_2 = 10$. The fold remains within the finely meshed middle region.

For comparison, a similar study was done using type-16 shell elements, with $n = 15$, $m_1 = 10$ and varying m_2. The results are presented in Figure 5.10(c). The initial stiffness of the tape spring and the post-buckling response are accurately predicted, although the peak moment is over-estimated for $m_2 = 2$. The mesh with 40 mm long elements in regions 2 ($m_2 = 2$) also buckles at a slightly higher rotation than the others. The converging solution, obtained for $m_2 = 3$ provides an accurate solution with the smallest CPU time of 9 s.

With the hope of achieving better results with longer NURBS-based elements in region 2, higher order polynomials ($p = q = 3$) and a finer discretization of region 1 were chosen. It was found that the behavior of bicubic elements deviates from biquadratic elements and type-16 elements. As shown in Figure 5.10(b), the pre-

buckling response is the same in all three cases but when m_2 was decreased from 4 to 2 the peak moment decreased and the steady-state post-buckling moment increased significantly. In conclusion, the NURBS elements in region 2 can be up to 20 mm long, corresponding to $m_2 = 4$, for a reasonably accurate solution, and the corresponding CPU time is 105 s.

An overall comparison of CPU times is presented in Table 5.5, with the meshes that provide the best CPU time performance highlighted.

Comparing the best result obtained with the reduced integration biquadratic NURBS mesh ($m_2 = 5$) with the previously obtained CPU time for uniformly distributed elements of the same type (50×10, reduced integration), a 63.2% reduction was obtained, with a reduction of 57.7% in number of degrees of freedom. In case of type-16 elements, the CPU time reduction from uniformly distributed elements to high aspect ratio elements was slightly worse, 60.9% instead of 63.2%, as the number of variables was reduced by 58.5%.

Overall, these results show that significant performance improvements are achieved with non-uniform meshing, but NURBS-based elements are still much more expensive than the standard bilinear finite elements.

m_2	Degrees of freedom	CPU time (s)
Biquadratic NURBS, $n = 10$, $m_1 = 10$		
10	1152	44
5	**792**	**28**
3	648	24
Bicubic NURBS, $n = 10$, $m_1 = 20$		
5	1287	134
4	**1209**	**105**
2	1053	81
type-16 shell, $n = 15$, $m_1 = 10$		
5	1680	14
3	**1360**	**9**
2	1200	9

Table 5.5: CPU times for simulations presented in Figure 5.10. The best converging results are highlighted in bold.

5.7 Conclusion

Simulations of geometrically nonlinear deployable thin-shell structures have been carried out to compare the computational efficiency of two different finite ele-

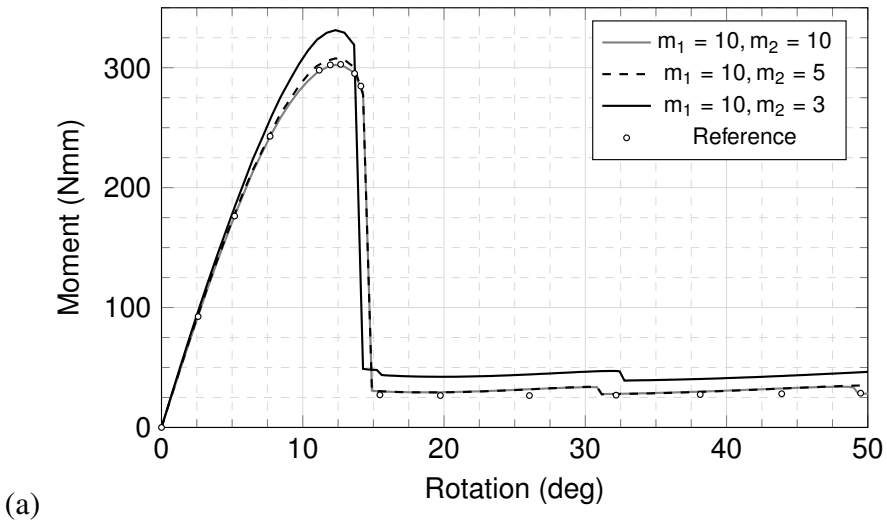

(a)

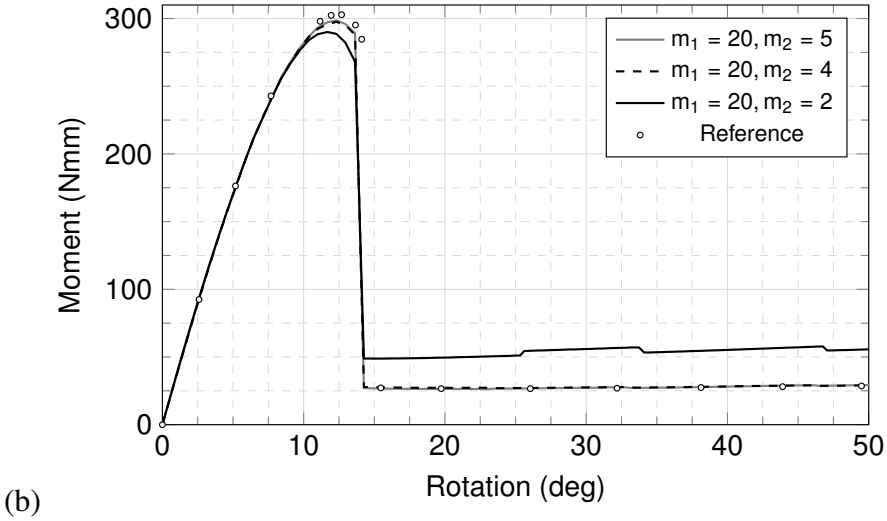

(b)

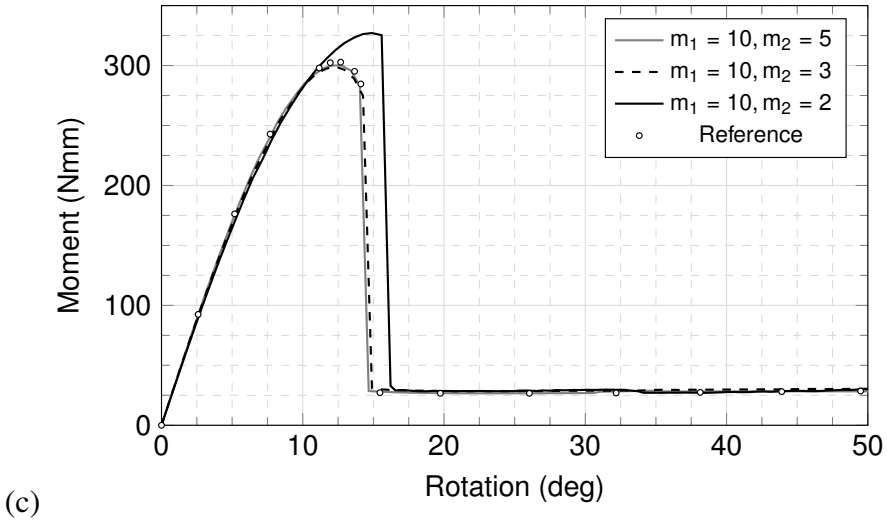

(c)

Figure 5.10: Convergence analysis using (a) reduced integration biquadratic NURBS with $n = 10$, (b) reduced integration bicubic NURBS with $n = 10$, and (c) type-16 shell elements with $n = 15$.

ment formulations, type-16 bilinear thin-shell elements vs. NURBS-based elements, available in version R11.1 of the LS-DYNA software. Specifically, the comparison was between fully-integrated bilinear quadrilateral (type-16) finite elements and C^1-continuous biquadratic and C^2-continuous bicubic NURBS-based elements, respectively. The NURBS elements are rotation-free and use a Reissner-Mindlin shell formulation with kinematics based on a degenerated solid approach.

The opposite sense folding of a tape spring was used as a case study that was divided into two parts. In the first part, the tape spring was discretized into a uniform mesh of identical elements. Comparing the coarsest meshes for which convergence was achieved, the bilinear elements were more than three times faster than the NURBS-based elements (23 s vs. 76 s). In the second part of the comparison, high aspect ratio elements were employed in the parts of the tape spring that deform less and a speed-up of around 40% was obtained for both types of elements. The higher-order and smooth NURBS-based elements converged with fewer degrees of freedom and the difference in simulation times decreased a bit, but they were still over three times computationally more expensive than the bilinear elements (9 s vs. 28 s).

It has been shown here that the currently available NURBS-based elements are considerably less efficient for the analysis of thin-shell deployable structures. It may be expected that the performance of the NURBS elements could be improved by using Kirchhoff-Love elements instead, however, this type of shell formulation was still under testing in LS-DYNA version 11.1 and could not be investigated in this study.

Chapter 6

H-ADAPTIVE FINITE ELEMENT ANALYSIS FOR QUASI-STATIC GEOMETRICALLY NONLINEAR PROBLEMS

6.1 Introduction

Thin-shell deployable structures, including booms and longerons, undergo complex deformations such as localized folding and buckling, and snap-through instabilities. These deformations are often accompanied by moving contact surfaces. Nonlinear finite analysis of such behaviors requires highly dense meshes in the regions of interest. Since most of the deployable structures such as booms are very long in one dimension compared to the others, mesh density must be high throughout the domain of the analysis leading to a high computation cost.

The computation cost can be reduced by adapting the mesh to the deformation throughout the geometrically nonlinear analysis. In other words, the finite element mesh can be refined in the regions of localized deformation or stress concentrations, and can be coarsened in the regions with small deformations.

While the adaptive finite element framework developed in this chapter will be valid for any thin-shell deployable structure, the Caltech Space-based Solar Power Project (SSPP) is chosen as a specific focus. The primary structural elements, the longerons, undergo local and global buckling and these buckles can elastically move along the length of the longerons. The two flanges of a longeron are longitudinally straight and transversely curved thin shells. The flanges, by themselves, would be called tape springs—the most fundamental and widely used deployable structures [30]. Hence, we use the widely studied quasi-static opposite-sense bending of a tape spring as a tool to develop and verify our adaptive finite element framework.

The geometric properties (defined in Figure 6.1(a)) and the material properties (Young's modulus E and Poisson's ratio ν) of the specific tape spring that was studied are listed in Table 6.1.

L	R	t	α	E	ν
200 mm	10 mm	0.1 mm	110°	131 GPa	0.3

Table 6.1: Properties of tape spring chosen for the case study.

Mesh adaptivity has three components: error estimation or refinement indication,

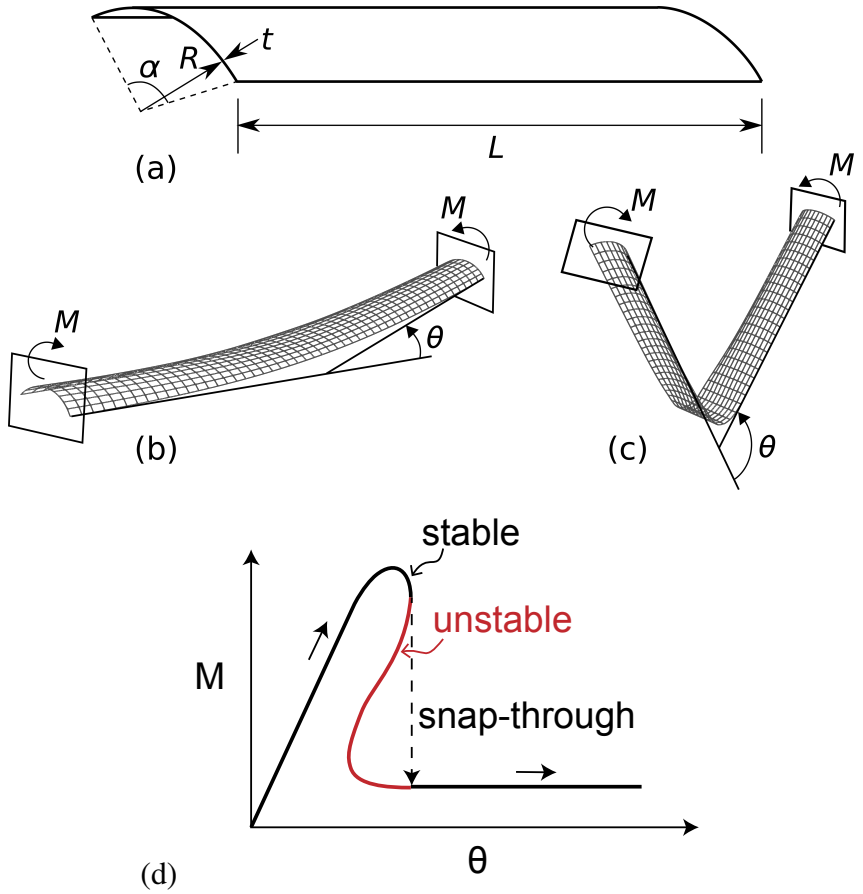

Figure 6.1: Case study. (a) Schematic of tape spring of length L, radius of cross-section R, thickness t and subtended angle α. (b) Tape spring under opposite sense bending, and (c) schematic of post-snap-through configuration with elastic fold in the middle. (d) A typical moment-rotation relationship for a tape spring under opposite-sense bending. Although non-physical, arclength solvers can trace the unstable path shown in red.

remeshing, and solution mapping. First step of adaptove meshing is to identify the regions of the domain that need refinement, coarsening or an improvement in the finite element mesh. The mesh in these regions is then altered (called remeshing) and the solution is transferred from the old mesh to the new mesh (called solution mapping or transfer of variables). Following is a brief description of these components for geometrically nonlinear finite element analyses.

6.2 Error estimators or refinement indicators

Error estimation or refinement indication is a crucial step in h-adaptive mesh refinement, as it determines which regions of the mesh require adjustments to accurately capture the solution. Broadly, there are two ways of assessing the error: error

estimators or refinement indicators [74]–[77]. An error estimator approximates a measure of the actual error in a given norm and is ideally close to the true error. Refinement indicators, on the other hand, are based on physical properties specific to the application [78], [79].

Majority of the literature on mesh adaption for linear elliptic problems uses a posteriori error estimation. This error estimation aims to compare the finite element solution with the actual solution. Since an actual solution is not available, the comparison is instead made with a 'recovered' solution which is obtained by using recovery techniques. The 'error' or the difference between the finite element solution and the recovered solution is then used to guide the mesh adaption. The most widely used a posteriori error estimator was proposed by Zienkiewicz and Zhu [80], which uses simple nodal averaging to improve the finite element solution. Some of the studies that use this error estimator are [81]–[89]. While there were many suggested improvements to their recovery techniques ([90], [91] for instance), the underlying idea remains the same.

Several contributions to stress recovery and error estimation for two-dimensional linear elliptic problems can be found, but there are relatively few applications to linear analyses of shell structures [76], [79], [92]–[96] and even fewer to nonlinear analysis of shells [81], [97], [98]. Moreover, most of the studies on nonlinear adaptive finite element analysis for shells are limited to standard patch tests and applications to real-world problems are quite rare. Especially, applications to thin-shell deployable structures are non-existent.

Studies of nonlinear analyses of shells use error estimators originally developed for linear problems. While the error estimators perform well for linear problems, rigorous error estimators for highly nonlinear problems are still missing [99]. Although many nonlinear generalizations have been made from the linear estimators, most of them lack the sound theoretical basis of their linear counterparts [98], [100], [101].

Therefore, we propose using strain energy itself as a refinement indicator. After all, every finite element analysis fundamentally rests upon minimization of energy [101]. Using the opposite-sense bending of a tape spring as a case study, we will compare the evolution of an energy norm error in the finite element solution [90] with that of bending strain energy and demonstrate that the latter is the right choice for a refinement indicator.

Error in energy norm

For the sake of completeness, we present here the error estimator by [90] that will be used for comparison against strain energy based refinement indicator.

The error in a finite element solution is defined as the difference between the actual solution and the finite element solution at the nodes.

$$\boldsymbol{e} := \boldsymbol{u} - \boldsymbol{u}^{\boldsymbol{h}} \tag{6.1}$$

For purely linear-elastic materials, energy norm of this error over an element becomes

$$\|\boldsymbol{e}\|_E^2 = \frac{1}{2}\int_V \left(\boldsymbol{\sigma} - \boldsymbol{\sigma}^h\right) : \mathbf{C}^{-1} : \left(\boldsymbol{\sigma} - \boldsymbol{\sigma}^h\right)\, \mathrm{d}V^h, \tag{6.2}$$

where $\boldsymbol{\sigma}$ is the actual stresses in the region of the element, $\boldsymbol{\sigma}^h$ is the stress from the finite element solution at the integration points of the element, $\mathbf{C}$ is the stiffness matrix of the material, and $\mathrm{d}V^h$ is the volume of the element.

In the case of shells, where the finite element domain is a 2D manifold, the energy norm error can be derived from the stress resultants instead.

$$\|\boldsymbol{e}\|_E^2 = \frac{1}{2}\int_{\Omega^h} \left(\boldsymbol{s} - \boldsymbol{s}^h\right)^T \mathbf{C}^{-1} \left(\boldsymbol{s} - \boldsymbol{s}^h\right)\, \mathrm{d}S^h, \tag{6.3}$$

where $\boldsymbol{s}$ is the actual stress resultants in the region of the element, $\boldsymbol{s}^h$ is the stress resultants from the finite element solution at the integration points of the element, and $\mathrm{d}S^h$ is the surface area of the element.

Using Voigt notation, the stress resultant tensor can be represent as a vector of the generalized forces $\boldsymbol{N}$, generalized moments $\boldsymbol{M}$, and generalized shear forces $\boldsymbol{Q}$ as follows.

$$\boldsymbol{s} = \begin{Bmatrix} \boldsymbol{N} \\ \boldsymbol{M} \\ \boldsymbol{Q} \end{Bmatrix}. \tag{6.4}$$

The corresponding stiffness matrix can be written as

$$\mathbf{C} = \begin{bmatrix} \mathbf{C_m} & \mathbf{0} & \mathbf{0} \\ \mathbf{0} & \mathbf{C_b} & \mathbf{0} \\ \mathbf{0} & \mathbf{0} & \mathbf{C_s} \end{bmatrix}, \tag{6.5}$$

with

$$\mathbf{C_m} = \frac{Et}{1-\nu^2}\begin{bmatrix} 1 & \nu & 0 \\ \nu & 1 & 0 \\ 0 & 0 & (1-\nu)/2 \end{bmatrix}, \quad \mathbf{C_b} = \frac{t^2}{12}\mathbf{C_m}, \quad \mathbf{C_s} = \frac{Et}{2(1+\nu)}\begin{bmatrix} 1 & 0 \\ 0 & 1 \end{bmatrix}. \tag{6.6}$$

However, the above definition of the error requires the actual solution which is unavailable. Therefore, this approach replaces the unknown actual solution $\boldsymbol{s}$ by a solution recovered from the finite element solution itself $\boldsymbol{s}^*$. Therefore, the energy norm error over an element now becomes

$$\epsilon^2 = \|\boldsymbol{e}\|_E^2 := \frac{1}{2}\int_{\Omega^p} \left(\boldsymbol{s}^* - \boldsymbol{s}^h\right)^T \mathbf{C}^{-1} \left(\boldsymbol{s}^* - \boldsymbol{s}^h\right) \det(\mathbf{J})\, \mathrm{d}\xi\, \mathrm{d}\eta, \tag{6.7}$$

where Ω^p is the domain of the master element and $\mathbf{J}$ is the Jacobian of the mapping between the reference and the actual domains.

For the above integration over the area of the master element (with area $\mathrm{d}\xi\, \mathrm{d}\eta$), the stress resultants over an element $\boldsymbol{s}^*(\xi, \eta)$ are computed using the weighted linear combination of the nodal recovered stresses and the weights are the values of the shape functions at that location.

Stress recovery at nodes

We recover the stress resultants at the nodes as follows.

The recovered stress resultant vector at a point in the reference domain $\boldsymbol{s}^*(\xi, \eta)$ has six components $s^{*i}(\xi, \eta)$, with $i = 1$ to 6. Value of each component s^{*i} at a point (ξ, η) can be defined as the weighted linear combination of the nodal values of that component as follows.

$$s_e^{*i}(\xi, \eta) := \sum_{a=1}^{n_N} N^a(\xi, \eta) s_{ae}^{*i} = \{N(\xi, \eta)\}^T \{s_e^{*i}\}, \tag{6.8}$$

where the subscript e represents an element, n_N is the number of nodes in the element, $\{N(\xi, \eta)\}$ is the vector of shape functions, a function of the position (ξ, η), and $\{s_e^{*i}\}$ is the vector of unknown nodal values at the element level (of size $n_N \times 1$) of the component s^{*i}.

The global vector of nodal values $\{s^{*i}\}$ are obtained by minimizing the below function over the domain of the whole finite element mesh.

$$F(\{s^{*i}\}) := \int_{\Omega} \left(s^{*i} - s^{hi}\right)^2 \mathrm{d}S^h, \tag{6.9}$$

where s^{hi} is the component of stress resultant s^i from the finite element analysis. This information is available at the integration points of the elements.

At an element level, the above function becomes

$$F(\{s_e^{*i}\}) := \int_{\Omega^h} \left(s_e^{*i}(\xi, \eta) - s_e^{hi}\right)^2 \mathrm{d}S^h. \tag{6.10}$$

Using Equations 6.8 and 6.10, and minimizing the above function at the element level with respect to the nodal vector $\{s_e^{*i}\}$,

$$[A_e]\{s_e^{*i}\} = \{b_e\}, \tag{6.11}$$

with

$$[A_e] = \int_{\Omega^h} \{N\}\{N\}^T \mathrm{d}S^h, \quad \{b_e\} = \int_{\Omega^h} \{N\} s_e^{hi} \mathrm{d}S^h. \tag{6.12}$$

A global linear system of equations for the global nodal values, $[A]\{s^{*i}\} = b$ can be assembled from the above equations at element level.

6.3 Remeshing

The most commonly used approaches for large deformation problems are the r-adaptivity where the nodes are merely relocated [102]–[105], or h-adaptivity which involves changing the number of nodes and/or elements [81], [106]–[108], or a combination of both. The structures of our interest are narrow and long booms such as the tape spring that undergo localized deformations. The use of mesh adaption should allow us to begin the analysis with as few elements as possible in both the directions—longitudinal and transverse. However, since r-adaptivity does not create new elements and only rearranges the nodes to alter the mesh density, only so much refinement is possible in transverse direction. Capturing the localized deformations with this method, for example immediately before snap-through buckling in tape springs, requires a large number of elements along the transverse direction to begin with.

On the contrary, the h-adaptive method adjusts the spatial discretization by continuously increasing the mesh density in zones where a more accurate response is

expected. This approach is particularly effective in improving the solution accuracy for problems involving large and localized deformations, and moving folds. Therefore, only h-adaptive refinement for quadrilateral elements will be used in this study.

When a quadrilateral element is split into two or more quadrilaterals, certain newly created nodes do not belong to the neighboring elements despite being placed on the common edges (Figure 6.2(a)); such nodes are called non-conformal or 'hanging' nodes and the mesh is termed non-conformal or irregular. This irregularity leads to a discontinuity in the mesh. Each irregular edge contains a new middle node that does not contain any new degree of freedom. In order to preserve continuity, degrees of freedom of a hanging node must be constrained with respect to those of its neighbors[109], [110]. For example, when using linear shape functions, degree of freedom at a hanging node is constrained to be the average of those at the two neighbors on that edge.

It is advantageous to 'regularize' the mesh by restricting the number of irregular vertices on each edge. Reasons for this are simplifying computations such as matrix assembly and mesh refinement, increasing approximation power by ensuring that neighboring elements are not of vastly differing sizes, and guaranteeing that each element is in the support of a bounded number of basis functions [111].

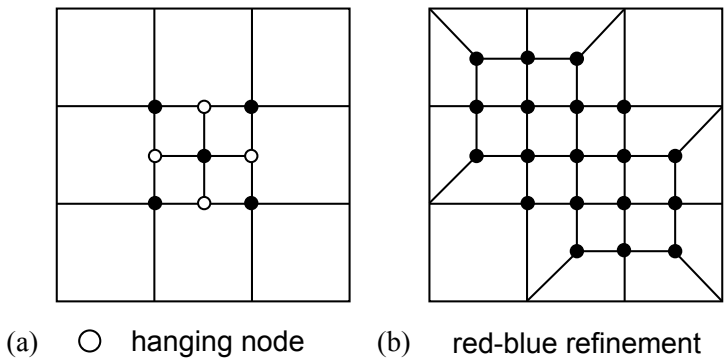

Figure 6.2: (a) Creation of hanging nodes when one element is refined. (b) Regularizing the mesh through red-blue refinement. The element marked for refinement is split into four new elements (red) and the neighbors are split into three new elements each (blue)

There are various techniques for regularizing an irregular mesh. The underlying idea of all is to further refine the elements around the hanging nodes with the aim of forming new edges and elements using the hanging nodes. This process continues

until no hanging node exists in the mesh or until a boundary is reached. The newly created elements in this process are often called transition elements. Many different regularization techniques that use quadrilateral or triangular transition elements or a combination of both were proposed in the literature [82], [112]–[118]. Typically, when refining a quadrilateral mesh, an element that is split into four new elements is nicknamed 'red' element; the element that is split into three is 'blue' and the one split into two new elements is 'green' [1]. In this study, we use the 'red-blue refinement' illustrated in Figure 6.2(b). To implement it, we will use the open-source Matlab package developed by [1] that combines several ideas from the literature, and propose an improvement to their technique.

6.4 Solution mapping or transfer of variables

Almost all the previous studies on adaptive meshing for shells used recovery techniques to transfer solution from the old integration points to the new [108], [119], [120]. This approach comprises of the following steps and is illustrated in Figure 6.3(a).

1. Transfer the solution such as stress and strain at the integration points of the old elements to the old nodes.

2. Assign solution variables to each node in the new mesh by interpolating values of the solution variables at that location based on the nodal values of the old mesh.

3. Evaluate the solution variables at the new integration points based on the nodal values of the new mesh.

4. Assign these solution variables as initial conditions to the following analysis. A few equilibrium iterations on the new mesh might be necessary to ensure that the transferred solution is in equilibrium with the external load.

We will investigate the efficiency of this solution mapping method for our case study and demonstrate that it fails to improve the result with mesh refinement. We propose a novel and seemingly obvious method where the solution variables at the new integration points are interpolated directly from the old integration points (Figure 6.3(b)). In this method, first the old element (parent element) that contains the location of the new integration point of interest is identified. Next, using the basis functions corresponding to the (old) integration points of the parent element,

the solution variable at the location of the new point is interpolated. This solution is then assigned to the new integration point.

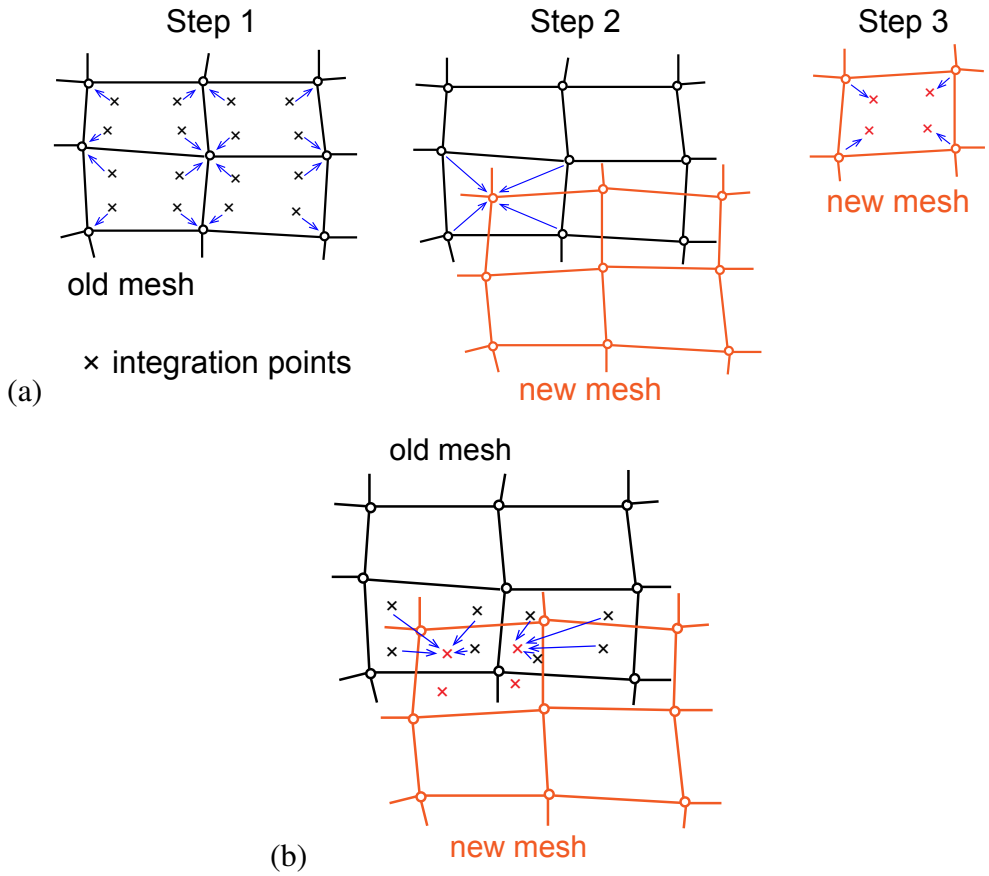

Figure 6.3: Two methods of transfer of variables: (a) Method 1 transfers recovered nodal stress resultants at the nodes of the old mesh to the nodes of the new mesh followed by another transfer to the new integration points. (b) Method 2 directly transfers the stress resultants from the old integration points to the new.

6.5 Software used

Simulations of the end-rotation-controlled, opposite-sense bending of an isotropic tape spring were carried out with the commercial finite element software Abaqus. Quasi-static finite element simulations were performed using the Riks arclength solver and the 4-noded reduced integrated shell elements called S4R. This is a planar element with only one integration point to avoid shear locking, and comes with default hourglass stabilization [29]. It has six degrees of freedom per node in the local coordinates. The solution from Abaqus was transferred to the programming platform Matlab for postprocessing using the open-source package called Abaqus2Matlab [121].

6.6 Results

Choosing a refinement indicator

To investigate the efficiency of the error estimator based on energy norm (Section 6.2), a non-adaptive finite element analysis of the opposite-sense bending of the tape spring with a uniform mesh of 30×10 (longitude×transverse) is considered (Figure 6.4). The distribution of energy norm error at different values of rotation (marked in Figure 6.4) are shown in Figure 6.5(a)–(d).

The bending behavior of a tape spring is well known and the localized fold is expected midway along the longitudinal direction. Hence, a refinement indicator must be able to predict the need for a finer mesh in the middle of the tape spring. However, until the peak moment is reached, maximum energy norm error is concentrated away from the region of an imminent fold.

At the same values of rotation, the distribution of the strain energy due to bending is shown in Figure 6.5(e)–(h). Maximum bending strain energy is always concentrated in the region of the imminent fold and hence this quantity is an appropriate refinement indicator for nonlinear analysis of the tape spring. Since every quasi-static finite element formulation is built upon minimization of the total potential energy, a refinement indicator based on strain energy must be appropriate for any nonlinear analysis [101].

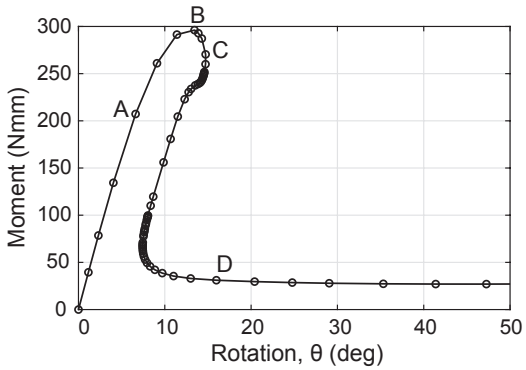

Figure 6.4: Moment vs rotation with the mesh size 30×10.

Choosing a method of transfer of variables

To investigate the efficiency of transfer of solution based on recovered nodal stresses (Section 6.4), we considered an adaptive analysis of the tape spring bending without making any changes to the mesh. a uniform mesh of 30×10 was used throughout the analysis. However, the finite element analysis was broken at arbitrary values of rotation and the solution mapping was performed using the two methods mentioned

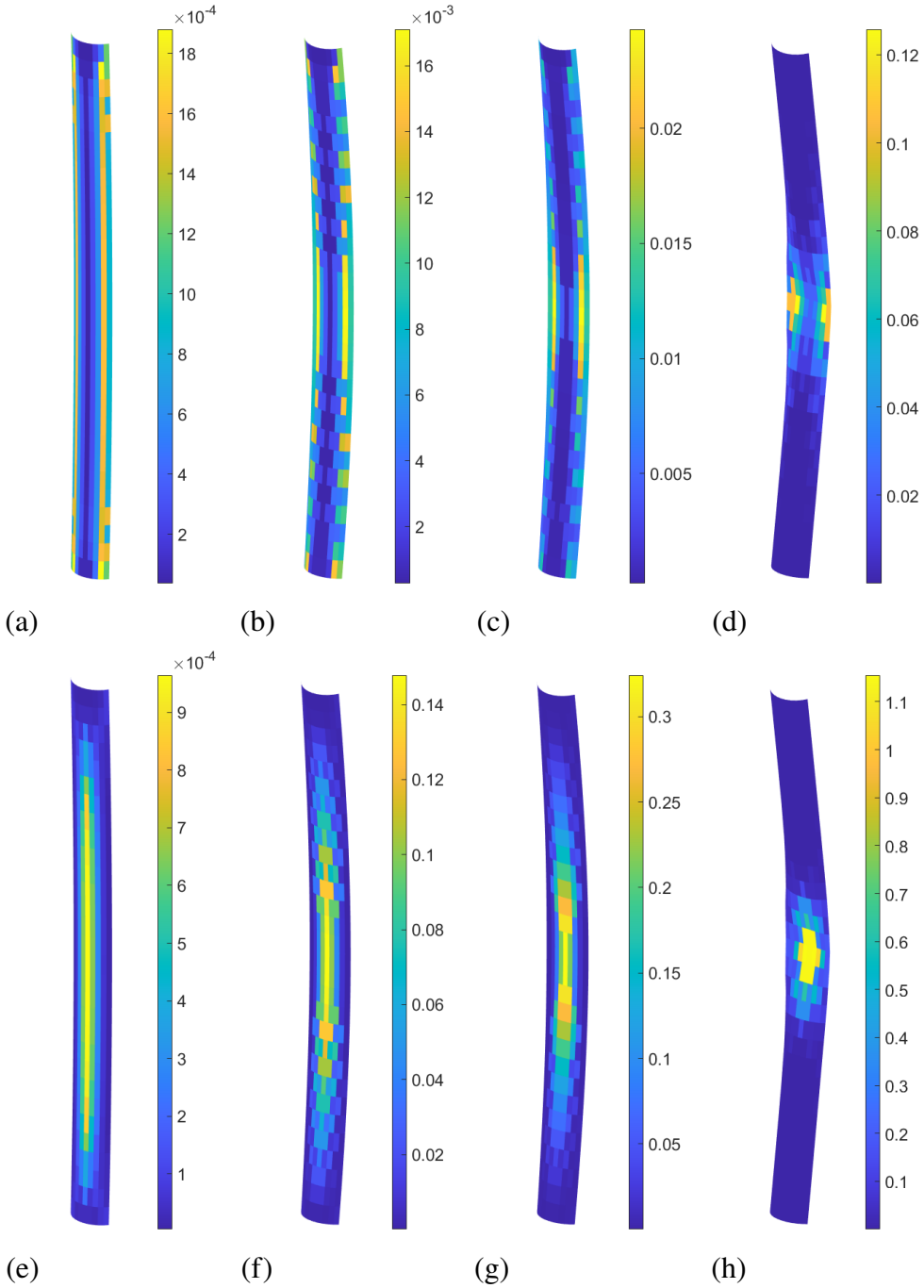

Figure 6.5: (a)—(d) Energy norm error and (e)—(h) bending strain energy (in mJ) at four different rotations $\theta \approx 4°, 13.4°, 14.7°, 16°$, respectively, of the opposite-sense bending of the tape spring with a uniform mesh 30×10 (Figure 6.4).

in Section 6.4. Since there was no change in the mesh, an appropriate method of solution transfer should not alter the result. The results from the multiple runs of the adaptive analysis were compared with the result from a non-adaptive analysis with the same mesh (Figure 6.6).

When the method based on recovered nodal stresses was used (referred to as Method 1), the solution deviated from that of the non-adaptive analysis using the same mesh. The amount of deviation increased every time the solution was transferred with no change in the mesh.

On the other hand, if the solution were transferred directly between the integration points without any stress recovery, the solution should not deviate from the non-adaptive analysis since the mesh remains the same. This is evident from Figure 6.6(b). The only deviation in this case is seen in the unstable equilibrium path traced by the Riks arclength solver in Abaqus. However, this path has no physical basis and can be non-unique (Figure 6.1). Therefore, this method is best suited for nonlinear analyses and will be used in the rest of this study.

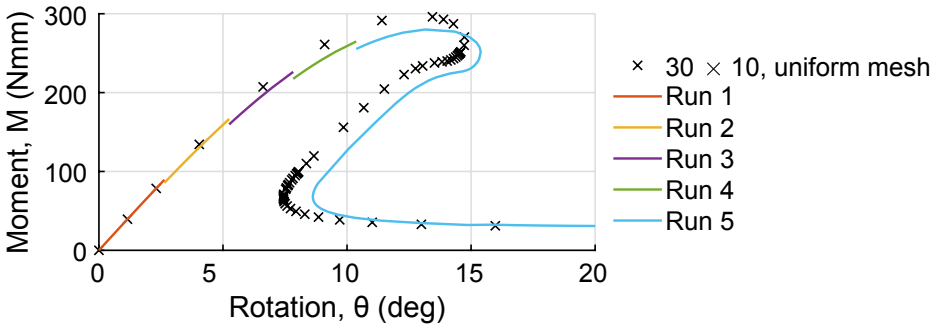

(a)

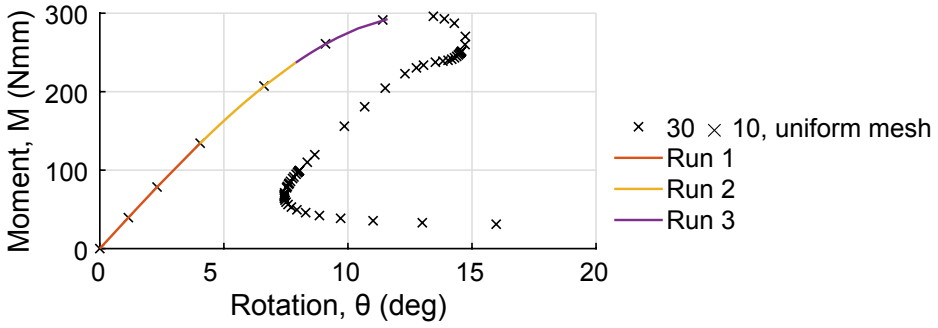

(b)

Figure 6.6: Moment vs rotation using (a) Method 1: transfer of variables based on recovered nodal stresses, and (b) Method 2: direct transfer of stress resultants from old integration points to the new.

Choosing a method of mesh refinement

There are various ways to generate a regular mesh without hanging nodes upon refinement. In case of long aspect ratio structures such as the tape spring, when an element is marked for refinement, all the elements in the same row along the longitudinal or transverse directions can also be refined. Refinement along the longitude refers to the increase in number of elements along the length of the tape spring (Figure 6.7). Carrying over the refinement to the boundaries does not leave any hanging nodes. While such a refinement in the longitudinal direction does not increase the total number of elements by a large number, refining along the transverse direction might result in an unnecessarily large number of elements.

To investigate the efficiency of these two refinement techniques, adaptive analyses were performed with refinement only in one direction in each case (Figures 6.7 and 6.8). a uniform mesh with size 20×5 was used to begin an analysis. For comparison, results from the non-adaptive analyses with uniform mesh of sizes 200×20 and 20×5 are also shown. An appropriate refinement technique would steer the solution from that of the 20×5 mesh towards the solution with a much finer mesh of 200×20.

In the case of mesh refinement in the longitudinal direction, three refinements were performed at arbitrary values of rotation. All the elements within the span of 40 mm in the middle of the tape spring were halved at each stage of refinement (Figure 6.7(b)–(d)). This method of refinement did not improve the result. This could be because although the refinement introduced more elements, there was no improvement in the finite element approximation of the cross-section of the tape spring. Only a small improvement in the $M-\theta$ curve can be noticed immediately after the snap-through buckling. This is because of the higher mesh density available in the middle of the tape spring to better approximate the curvature of the elastic fold.

In the case of refinement only in the transverse direction, when the new nodes were placed on the edges of the parent elements, the $M-\theta$ curve deviates from that of the non-adaptive analysis with mesh size 20×5. One of the reasons could be that there was no improvement in the approximation of the curved geometry of the tape spring. Another reason for the deterioration of the bending response could be the long aspect ratio of the newer elements. Each element in the initial mesh is 10 mm long and 3.82 mm wide. The width of an element gets halved with refinement. Therefore, the elements in the middle of the cross-section of the tape spring have widths 1.91 mm, 0.955 mm, and 0.475 mm after the first, second, and third refinements, respectively

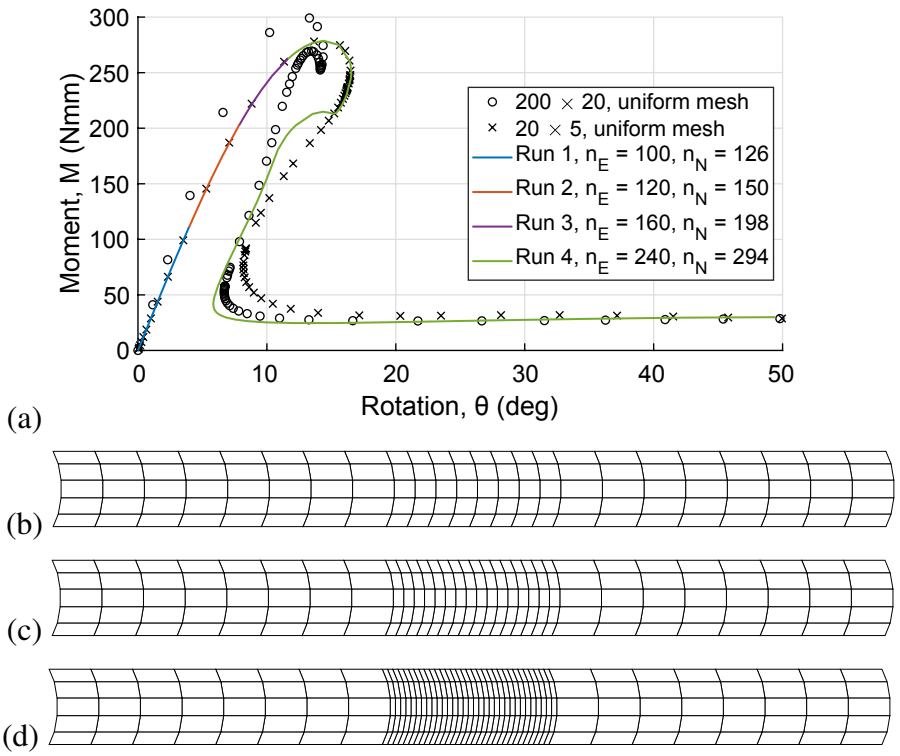

Figure 6.7: (a) Moment vs rotation when the refinement is performed only along the longitude of the tape spring. (b)—(d) Finite element mesh used for Runs 2, 3, and 4, respectively. n_E is the number of elements and n_N is the number of nodes in the mesh.

while the length remains at 10 mm.

The finite element response of a thin-shell structure is sensitive to the approximation of the curved cross-section. For the mesh adaption to be more effective for nonlinear shell analyses, the new nodes must be placed closer to the actual deformed surface of the structure. Actual deformed surface of a shell structure in current configuration is usually approximated by interpolating a smooth surface from the positions of the nodes. If linear interpolation of the displacements is used to find the current location of the new node, it would be placed midway between the nodes of the old mesh. Bilinear interpolation might introduce discretization errors in the transferred solution if the old mesh is relatively coarse. Often, cubic interpolation by means of Hermitian interpolation is used to estimate the true deformed surface [81, Chapter 6].

For the tape spring with a simple undeformed geometry, we also propose an 'exact' interpolation where the remeshing is first performed on the initial curved geometry.

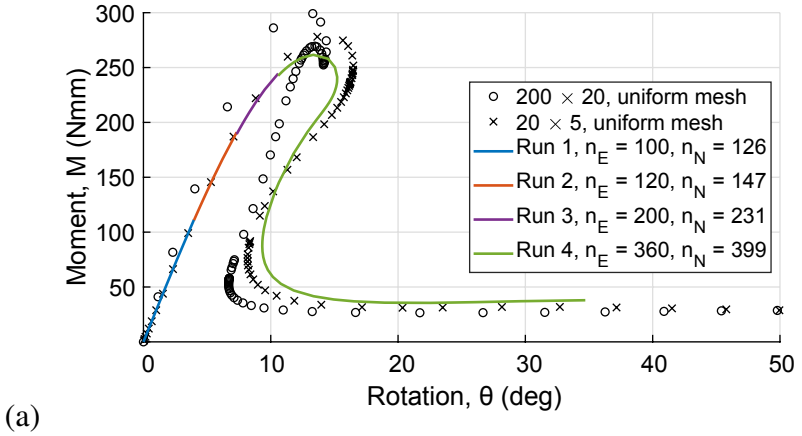

(a)

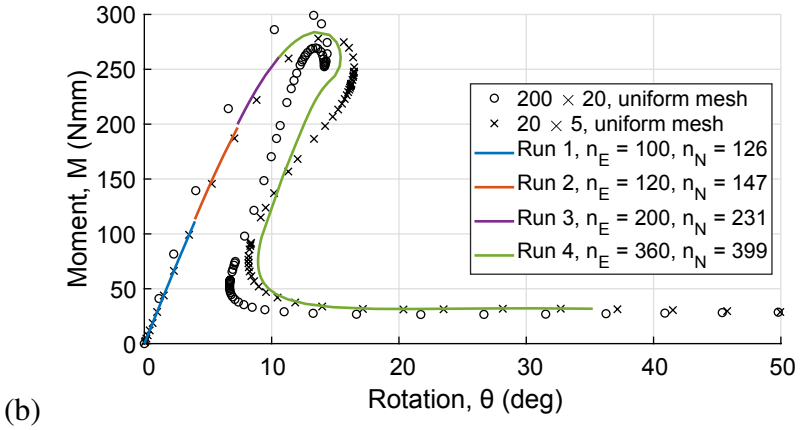

(b)

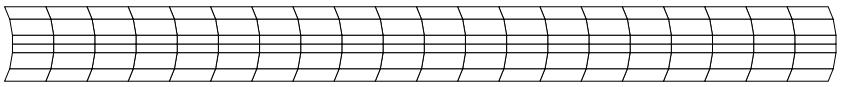

(c)

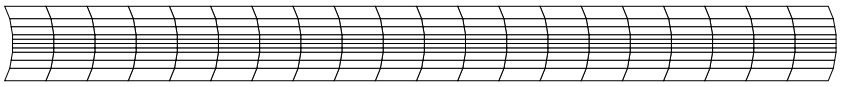

(d)

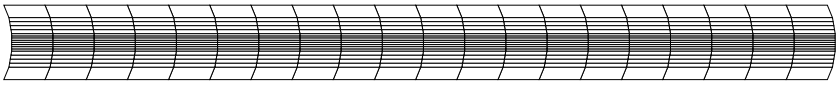

(e)

Figure 6.8: Moment vs rotation when the refinement is performed only in the transverse direction of the tape spring. New nodes are placed on the planes of the parent elements in (a). Exact interpolation is used to place new nodes on an approximate current geometry in (b). (c)—(e) Finite element mesh used for Runs 2, 3, and 4, respectively. n_E is the number of elements and n_N is the number of nodes in the mesh.

In other words, the new nodes are first placed on the exact circular surface of the tape spring and are then displaced in 3D space to their current positions. This displacement at a new node is the average of the displacements of the two neighboring nodes from the old nodes.

Repeating the above adaptive analysis using the proposed exact interpolation improves the bending response noticeably before buckling occurs (Figure 6.8(b)). However, the post-buckling response remains the same as before.

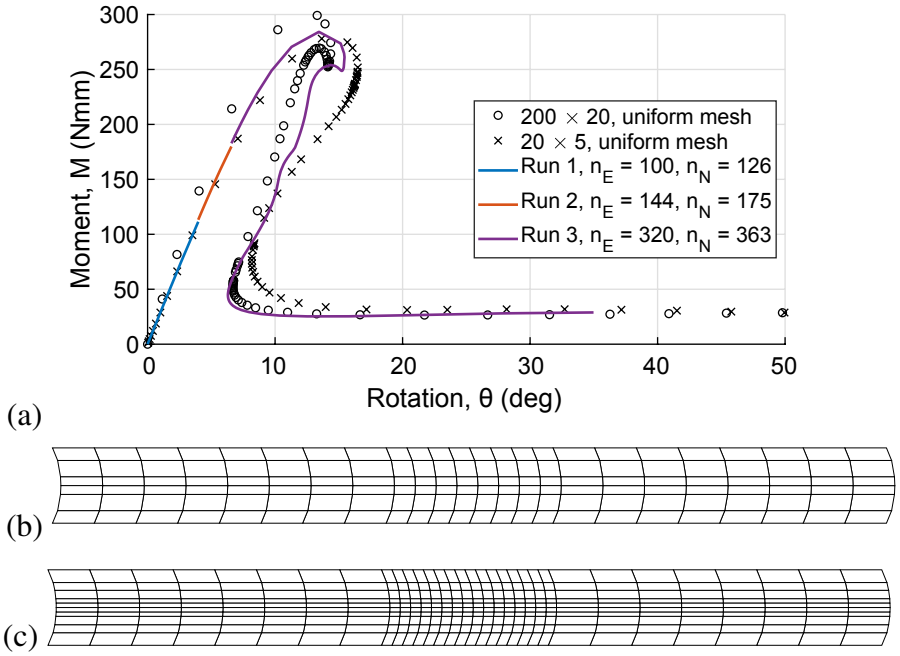

Figure 6.9: (a) Moment vs rotation when the refinement is performed along both the directions. (b), (c) Finite element mesh used for Runs 2, 3, respectively. n_E is the number of elements and n_N is the number of nodes in the mesh.

By refining the mesh in both the directions and using exact interpolation, the adaptive analysis inherits the advantages of the two techniques. Pre-buckling response improved because of the refinement in the transverse direction and the post-buckling response improved due to the refinement in the longitudinal direction. This improvement was seen with only two levels of refinement. Only two levels of refinement were performed to keep the maximum number of elements closer to that in the previous case for a fair comparison.

Despite the improvement, number of elements grows exponentially with each level of refinement. Aspect ratio of the refined elements also grows and the variation

of mesh density over the domain is not smooth. Hence, we turned to red-blue refinement for quadrilaterals to generate a regular mesh.

Improving the red-blue refinement of [1]

In red-blue refinement strategy, hanging nodes are eliminated by refining the neighboring elements into three quadrilaterals (blue elements). One blue refinement only shifts the location of the hanging node and several blue refinements are necessary to completely eliminate all hanging nodes. Because the hanging node is shifted from one edge to an adjacent edge, there is a directionality to this refinement strategy and if not implemented properly, it could trigger a long chain of refinements that ends only upon reaching a boundary. This is illustrated through three examples in Figure 6.10.

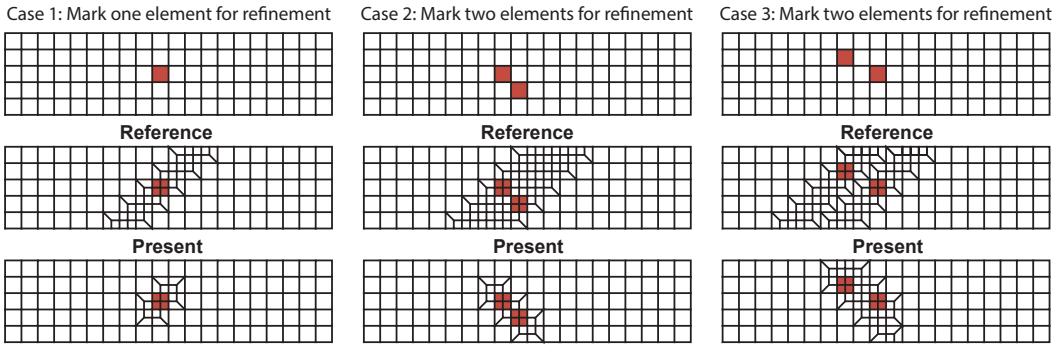

Figure 6.10: Comparison of the refinement efficiency of red-blue refinement of [1] (reference) and our improved version (present). The elements marked for refinement in the original mesh (top row) are shown in red. The reference version refines the mesh excessively and until the boundary is reached

The red-blue refinement implemented in [1] refines a significantly more number of elements than necessary for the reasons illustrated in Figure 6.11(a). In their technique, a node of the element is chosen as reference (the first node from the connectivity matrix for that element) and the Y- formation is limited to one of the two sides of the diagonal passing through the reference node (blue_r and blue_l). For this reason, when two edges on the opposite sides of the diagonal are marked, that element undergoes red refinement creating three new hanging nodes and triggering a new chain of blue refinements.

Moreover, since the blue refinements at various regions of the mesh happen independently of one another, the chain of refinements does not always come to an end before reaching the boundaries.

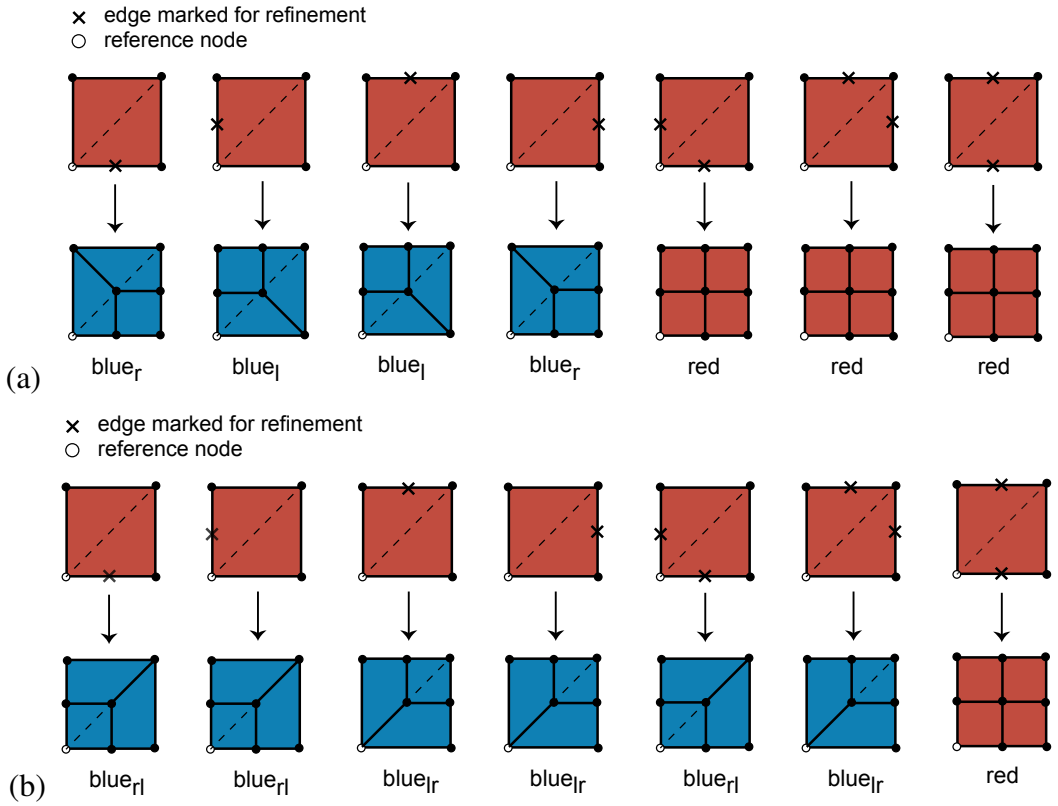

Figure 6.11: (a) Mapping used in [1]: Y-formation is restricted only one side of the diagonal (dashed line). (b) New mapping introduced in our improved version: When only one edge is marked for refinement, Y- refinement is centered about the diagonal. When two adjacent edges are marked for refinement, Y- is formed bisecting those two edges irrespective of the location of the reference node.

To improve these two situations, we introduced two new possibilities called blue_r and blue_l where the Y-formation always happens about the diagonal. In this strategy, the refinement has a tendency to loop around an element originally marked for refinement rather than branching away from it. Performance of this improved version is evident in Figure 6.10. For the sake of completion, the complete mapping needed to reproduce this improved version of the red-blue refinement strategy is presented in Figure 6.12.

We performed an adaptive analysis of the tape spring bending using the improved red-blue refinement and the compared the performance of Hermitian and exact interpolations (Figure 6.13(a)). Only one refinement was performed at an arbitrary rotation to assess the performance of this refinement strategy. Eight elements in the middle, along the length of the tape spring were marked for refinement and the resulting mesh has 222 elements in total (Figure 6.13(b)). Refinement

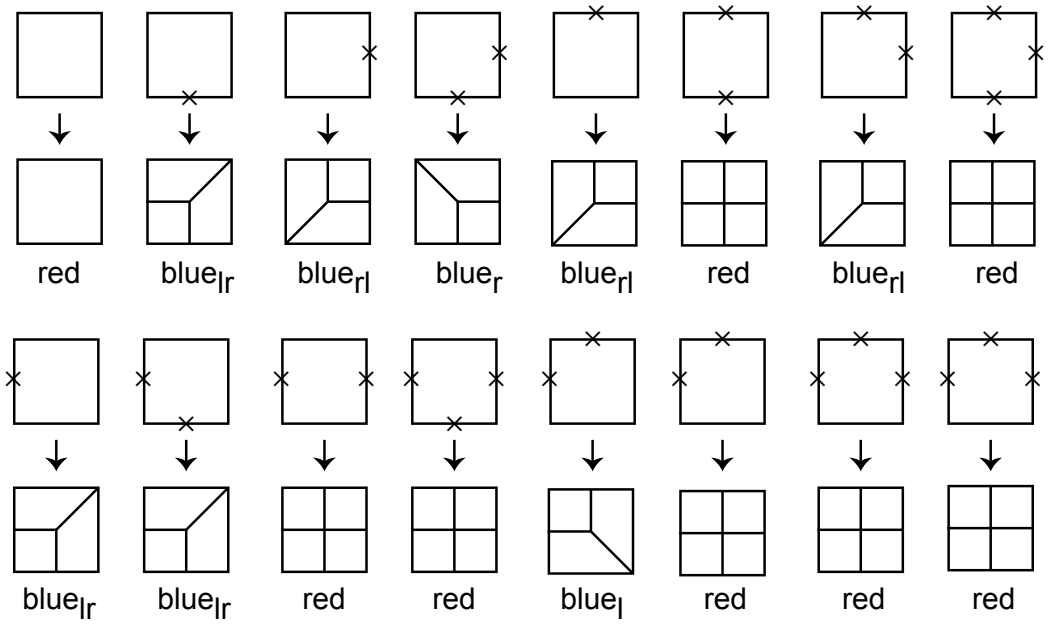

Figure 6.12: Complete mapping of red-blue refinement in the present improved version.

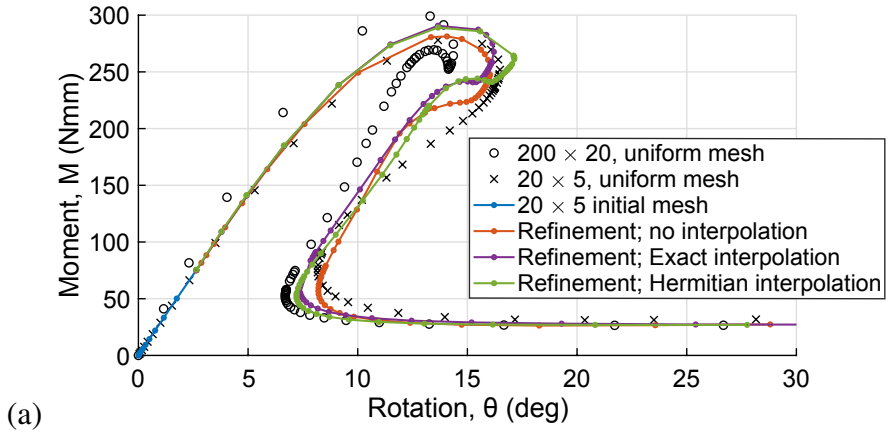

(a)

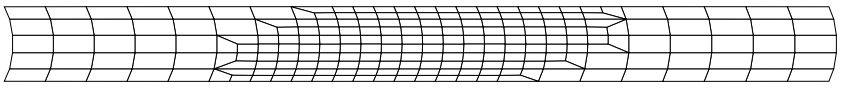

(b)

Figure 6.13: (a) Moment vs rotation with red-blue refinement. (b) Eight elements along the longitude in the middle of the tape spring were marked for refinement and the resulting mesh in (b) was used for Run 2; number of elements is 222 and number of nodes is 255.

with no interpolation or where the new nodes are placed on the planes of the old elements showed a slightly better approximation of the peak moment and the post-buckling behavior. Both the interpolation techniques further improved the response. The improvement can be further amplified by carefully choosing the instances of refinement, elements to be refined, and the number of levels of refinement.

Based on the above observations, red-blue refinement shows promise to the application of mesh adaptivity to geometrically nonlinear analysis of thin-shell deployable structures.

6.7 Conclusions

Mesh adaptivity for geometrically nonlinear analyses of thin-shell deployable structures have been non-existent in the literature. By using the opposite-sense bending of a tape spring as a case study, we showed that adaptive meshing shows promise in the field of deployable structures.

Mesh refinement has three components: error estimation or refinement indication, remeshing, and solution mapping. Most of the existing studies on nonlinear analyses of shells use inefficient error estimators that were originally proposed for linear elliptic problems. We compare the performance of one such error estimator based on energy norm with that of a refinement indicator based on strain energy, and showed that energy-based refinement indicators are best suited for nonlinear problems. Moreover, no extra computation is necessary to obtain such an indicator.

We also investigated the efficiency of a widely used solution mapping based on stress recovery and showed that it fails in a nonlinear analysis. We proposed a direct transfer of solution from the old integration points to the new and demonstrated its superior performance.

We applied the red-blue refinement strategy to refine the finite element mesh and proposed an improvement to an existing algorithm.

Overall, we have uncovered many open areas for potential research in the area of mesh adaptivity, and introduced novel and more efficient techniques to drive further research in the same area.

Chapter 7

CONCLUSIONS

The primary objective of this research was to achieve predictability in the unconstrained dynamic deployment of ultralight thin-shell space structures. This was done by developing effective numerical tools for simulating the folding and deployment of deployable structures, which were evaluated using the Caltech Space Solar Power Project (SSPP) structures as a case study. High-fidelity numerical simulations were used to understand the structure-mechanism interaction and the effects of initial and boundary conditions on deployment. To verify the accuracy of the simulations, a simple experiment benchmark was designed and deployment tests were performed.

Due to the computational expense of finite element methods, it is not feasible to simulate large deployable structures such as the next-generation Caltech SSPP structures at full scale. To address this, the study investigated the potential of more computationally efficient methods such as isogeometric analysis and h-adaptive finite element analysis.

This chapter provides a summary of the contributions made to the existing literature in achieving the research objectives. Additionally, it outlines possible directions for future research in related fields.

7.1 Experiments and numerical simulations of unconstrained dynamic deployment of Caltech SSPP structures

To understand the fundamental deployment behavior of the Caltech SSPP structures, a simplified deployment mechanism was devised to conduct tests on a quarter of the structure. Masses attached to diagonal cords drove the deployment, while infrared motion capture cameras tracked the structure's motion. Numerical simulations of the folding and deployment of the structure were developed using the explicit solver in the commercial finite element software, Abaqus. Verification of numerical simulations was carried out through point cloud data obtained from the experiments.

Contributions and future directions:

- This thesis addresses a gap in the literature regarding the unconstrained dynamic deployment of space structures, offering crucial insights and numerical

modeling tools for further research in this area. By establishing a foundation of knowledge and resources, this work provides a platform for advancing the design of space structures and encouraging more frequent use of unconstrained deployment in space missions. The implications of this research are significant, as they offer the potential to enhance the safety, efficiency, and reliability of space structures in the future.

- Until now, numerical simulations of thin-shell deployable structures have primarily focused on individual components or simplified systems. However, this study has achieved a significant breakthrough by successfully simulating the highly complex dynamic deployment of the Caltech SSPP. By developing high-fidelity numerical simulation techniques, this work offers a valuable resource that can be adapted to a wide range of thin-shell deployable structures, providing a promising avenue for future research and development.

- In order to better comprehend the fundamental behavior of SSPP structure deployment, a single quadrant was subjected to testing and simulation. To expand this understanding and explore the impact of neighboring quadrants on deployment, tests could be conducted using two quadrants, with the knowledge gained being applied to the full structure comprising four quadrants.

7.2 Making the deployment robust and predictable

Unconstrained deployment has the potential to offer significant advantages over controlled or sequential deployment schemes in terms of packaging efficiency and reducing the risk of failure. However, this approach has not been widely adopted due to concerns over its perceived unpredictability. The high-fidelity numerical simulations developed in this research were used to show that an unconstrained deployment can be made predictable.

The deployment of the structure was guided by constant force spring retractors connected to the diagonal cords. It was demonstrated that reducing the interaction between the structure and mechanism during deployment can lead to a smaller deployment envelope or reduced maximum height. Additionally, limiting the number of elastic folds and their location on the longeron can increase predictability. To further optimize the design, numerical simulations were conducted to analyze the effects of various parameters, such as gravity, initial orientation of the structure, mass of functional elements, as well as the positions of strip-cord connectors.

The fact that appropriate initial conditions can be selected to prevent the formation of new folds and maintain the stability of existing folds on the respective longerons enabled the construction of extended TRAC longerons by bonding multiple longerons together using epoxy. To demonstrate the efficacy of this approach, a deployment test was conducted on a larger four-strip structure. The deployment was guided by constant-force spring retractors and kickoff springs were utilized to minimize interaction between the structure and the cylinder. The deployment process exhibited no formation of additional folds, and the existing folds remained stationary, as desired.

Contributions and future directions:

- This thesis has successfully demonstrated a significant advancement in the deployment of space structures through the implementation of an unconstrained dynamic approach. The unconstrained dynamic deployment method developed herein ensures robustness and predictability throughout the deployment process. This breakthrough marks a pivotal contribution to the field, as it provides a solution to the long-standing problem of low confidence in unconstrained deployment methods. As a result, this novel approach has opened up new possibilities for the space industry and beyond, enabling researchers and practitioners to safely and efficiently deploy space structures with confidence and reliability.

- This study offers a promising solution for ensuring the safety of functional elements that will be carried by SSPP structures during deployment. Specifically, the study demonstrates that by limiting the number of elastic folds in a longeron to one and restricting its location, complex deformations can be avoided, thereby minimizing potential damage to functional components. These findings hold significant implications for the future deployment of SSPP structures, offering a new level of safety and reliability.

- Prior to this study, the design process of SSPP structures was limited to the stowed and fully deployed configurations. However, through a comprehensive investigation of the sensitivity of deployment to changes in the structure's design, this work has yielded a crucial finding: the need to consider intermediate deployment profiles. The implications of this discovery extend far beyond SSPP structures, as it underscores the importance of considering all possible deployment scenarios in the design of any deployable structure.

- The study validated the efficacy of ground tests in predicting in-space deployment of SSPP structures by demonstrating the consistency of the radial motion and strip shapes during deployment, irrespective of gravity. However, the study also revealed that gravity significantly impacts the maximum height attained by the structure. This highlights the importance of accounting for gravitational effects and designing deployment mechanisms with additional vertical clearance to ensure successful deployment in space. To further verify this observation, future deployment tests can be conducted with gravity offloading.

- Through simulations, the effect of functional element mass was investigated by approximating it with lumped masses at longeron-batten intersections. The study revealed that the additional mass did not affect the location or creation of folds on the longerons, indicating the robustness of the deployment. Future research can extend this study to explore the impact of membrane elasticity and tension on the unfolding of a strip.

- The size of the SSPP structure employed in previous experiments and simulations was constrained to approximately 1.7 m due to the limitations of the available autoclave for composite laminate curing. However, the SSPP envisions a structure measuring 60 m $\times$ 60 m. The insights gained from the deployment simulations facilitated the upscaling of SSPP structures. A practical out-of-autoclave bonding technique was proposed and successfully validated, enabling the construction of SSPP structures of any desired size.

7.3 Reducing the computation cost in modeling the folding of thin-shell structures:

The structure studied so far has a maximum length of around 1.7 m. However, the next generation of SSPP structures will be much larger, making full-scale simulations impractical. Therefore, more computationally efficient finite element methods are necessary. In this study, NURBS-based isogeometric analysis and h-adaptive meshing for quadrilateral shell elements were explored as potential solutions. To validate these methods, a simpler problem of quasi-static folding of a tape spring was used as a test case.

Isogeometric analysis for geometrically nonlinear, quasi-static analysis

An analysis of the folding of a tape spring, a prototypical thin-shell deployable structure, was conducted using both NURBS-based and bilinear Reissner-Mindlin finite elements available in the commercial software LS-DYNA. The analysis revealed that the isogeometric elements are slower than the bilinear finite elements by a factor of three. However, the use of a coarse mesh in the regions of the tape spring that do not deform significantly during folding leads to significant improvements in speed for both types of elements, although the difference in performance persists.

h-adaptive finite element analysis

There is currently a lack of literature on mesh adaptivity for geometrically nonlinear analyses of thin-shell deployable structures. This research aims to address this gap and has identified several areas for future investigation.

Contributions and future directions:

- The study found that, for the analysis of thin-shell deployable structures, it is not yet worth switching to NURBS-based elements. However, it may be expected that the performance of NURBS elements could be improved by using Kirchhoff-Love elements, which could be investigated in future studies.

- In this research, a significant contribution was made by demonstrating the ineffectiveness of existing error estimators originally proposed for linear elliptic problems and showing through a detailed comparison that the refinement indicator based on strain energy is the superior choice for nonlinear problems. By highlighting this issue and demonstrating a better solution, this research provides a crucial contribution to the literature on adaptive meshing for thin-shell deployable structures.

- This research proposes a new and effective technique for solution mapping in nonlinear analyses, which involves the direct transfer of solutions from old to new integration points. The superiority of this technique over the commonly used stress recovery-based solution mapping technique was demonstrated. However, the proposed method transfers stress resultants and the subsequent run is still affected by the inaccuracies in the previous runs. Therefore, future work could investigate a solution mapping based on the transfer of nodal degrees of freedom, which would enable the analysis to start from the undeformed configuration with transferred degrees of freedom as initial

conditions. This would require a short equilibrating step to bring the structure into the current configuration while generating the necessary stresses at the integration points to satisfy equilibrium.

- In this study, user-adaptivity was implemented to investigate the applicability of h-adaptive mesh refinement to thin-shell structures, and it was demonstrated to be effective. Future work can focus on developing self-adaptivity algorithms to determine the optimal instances of remeshing and the optimal level of mesh refinement. Additionally, adaptive mesh coarsening can be integrated into the algorithms. These advancements would result in more automated and efficient adaptivity methods for thin-shell structures.

- Finite element models of thin-shell structures are particularly sensitive to the accuracy of curvature approximation. In h-adaptive meshing, when new nodes are introduced, special interpolation techniques are required to place the nodes on an approximate true surface of the structure. Isogeometric analysis provides an advantage in this regard since it exactly interpolates the curved surface, resulting in more accurate and efficient analyses. By combining isogeometric analysis with mesh adaptivity, the benefits of both techniques can be utilized to achieve even greater accuracy and efficiency in the analysis of thin-shell structures.

BIBLIOGRAPHY

[1] S. A. Funken and A. Schmidt, "Adaptive mesh refinement in 2D–An efficient implementation in MATLAB," *Computational Methods in Applied Mathematics*, vol. 20, no. 3, pp. 459–479, 2020.

[2] B. Hoang, S. White, B. Spence, and S. Kiefer, "Commercialization of Deployable Space Systems' Roll-Out Solar Array (ROSA) technology for Space Systems Loral (SSL) solar arrays," in *2016 IEEE Aerospace Conference*, IEEE, 2016, pp. 1–12.

[3] J. M. Fernandez, G. K. Rose, C. J. Younger, *et al.*, "NASA's advanced solar sail propulsion system for low-cost deep space exploration and science missions that use high performance rollable composite booms," in *International Symposium on Solar Sailing*, 2017.

[4] M. Mobrem and D. S. Adams, "Deployment analysis of the lenticular jointed antennas onboard the mars express spacecraft," *Journal of Spacecraft and Rockets*, vol. 46, no. 2, pp. 394–402, 2009.

[5] A. Fikes, O. S. Mizrahi, A. Truong, F. Wiesemüller, S. Pellegrino, and A. Hajimiri, "Fully collapsible lightweight dipole antennas," in *2021 IEEE International Symposium on Antennas and Propagation and USNC-URSI Radio Science Meeting (APS/URSI)*, IEEE, 2021, pp. 545–546.

[6] J. Sicre, D. Givois, and A. Emerit, "Application of "MAEVA" hinge to myriade microsatellites deployments needs," in *11th European Space Mechanisms and Tribology Symposium, ESMATS 2005*, vol. 591, 2005, pp. 243–250.

[7] M. Sakovsky, S. Pellegrino, and H. Mallikarachchi, "Folding and deployment of closed cross-section dual-matrix composite booms," in *3rd AIAA Spacecraft Structures Conference*, 2016, p. 0970.

[8] M. J. Silver, M. A. Echter, B. M. Reid, and J. Banik, "Precision high strain composite hinges for the deployable in-space coherent imaging telescope," in *3rd AIAA Spacecraft Structures Conference*, 2016, p. 0969.

[9] H. Mao, P. L. Ganga, M. Ghiozzi, N. Ivchenko, and G. Tibert, "Deployment of bistable self-deployable tape spring booms using a gravity offloading system," *Journal of Aerospace Engineering*, vol. 30, no. 4, p. 04 017 007, 2017.

[10] J. M. Fernandez and A. J. Lee, "Bistable collapsible tubular mast booms," in *International Conference on Advanced Lightweight Structures and Reflector Antennas*, 2018.

[11] M. K. Chamberlain, S. H. Kiefer, and J. Banik, "On-orbit structural dynamics performance of the roll-out solar array," in *2018 AIAA Spacecraft Structures Conference*, 2018, p. 1942.

[12] A. J. Cook and S. J. Walker, "Experimental research on tape spring supported space inflatable structures," *Acta Astronautica*, vol. 118, pp. 316–328, 2016.

[13] F. Roybal, J. Banik, and T. Murphey, "Development of an elastically deployable boom for tensioned planar structures," in *48th AIAA/ASME/ASCE/AHS/ASC Structures, Structural Dynamics, and Materials Conference*, 2007, p. 1838.

[14] B. N. McPherson and J. L. Kauffman, "Dynamics and estimation of origami-inspired deployable space structures: A review," in *AIAA SciTech 2019 Forum*, 2019, p. 0480.

[15] M. Arya, N. Lee, and S. Pellegrino, "Ultralight structures for space solar power satellites," in *3rd AIAA Spacecraft Structures Conference*, 2016, p. 1950.

[16] E. Gdoutos, C. Leclerc, F. Royer, *et al.*, "A lightweight tile structure integrating photovoltaic conversion and rf power transfer for space solar power applications," in *2018 AIAA Spacecraft Structures Conference*, 2018, p. 2202.

[17] D. A. Türk and S. Pellegrino, "Parametric design of conforming joints for thin-shell coilable structures," in *AIAA Scitech 2019 Forum*, 2019, p. 1259.

[18] C. Leclerc and S. Pellegrino, "Nonlinear elastic buckling of ultra-thin coilable booms," *International Journal of Solids and Structures*, vol. 203, pp. 46–56, 2020.

[19] A. Pedivellano, E. Gdoutos, and S. Pellegrino, "Sequentially controlled dynamic deployment of ultra-thin shell structures," in *AIAA SciTech 2020 Forum*, 2020, p. 0690.

[20] E. Gdoutos, A. Truong, A. Pedivellano, F. Royer, and S. Pellegrino, "Ultralight deployable space structure prototype," in *AIAA Scitech 2020 Forum*, 2020, p. 0692.

[21] E. Gdoutos, C. F. Sommer, A. Truong, *et al.*, "Development of the deployable on-orbit ultralight composite experiment (dolce) for the space solar power project demonstration mission," in *AIAA SciTech 2022 Forum*, 2022, p. 1266.

[22] A. J. Lee and S. Pellegrino, "Mass efficiency of strip-based coilable space structures," *International Journal of Solids and Structures*, vol. 254, p. 111 867, 2022.

[23] A. Fikes, E. Gdoutos, M. Klezenberg, *et al.*, "The caltech space solar power demonstration one mission," in *2022 IEEE International Conference on Wireless for Space and Extreme Environments (WiSEE)*, IEEE, 2022, pp. 18–22.

[24] A. Pedivellano, "Deployment dynamics of thin-shell space structures," Ph.D. dissertation, California Institute of Technology, 2021. [Online]. Available: https://resolver.caltech.edu/CaltechTHESIS:06012021-002457442.

[25] H. Mallikarachchi and S. Pellegrino, "Deployment dynamics of ultrathin composite booms with tape-spring hinges," *Journal of Spacecraft and Rockets*, vol. 51, no. 2, pp. 604–613, 2014.

[26] S. Ferraro and S. Pellegrino, "Self-deployable joints for ultra-light space structures," in *2018 AIAA Spacecraft Structures Conference*, 2018, p. 0694.

[27] F. Dewalque, C. Schwartz, V. Denoël, J.-L. Croisier, B. Forthomme, and O. Brüls, "Experimental and numerical investigation of the nonlinear dynamics of compliant mechanisms for deployable structures," *Mechanical Systems and Signal Processing*, vol. 101, pp. 1–25, 2018.

[28] A. Pedivellano and S. Pellegrino, "Deployment dynamics of thin-shell space structures," *Journal of Spacecraft and Rockets*, vol. 59, no. 4, pp. 1214–1227, 2022.

[29] M. Smith, *Abaqus/standard user's manual, Version 6.9*, Providence, RI : Dassault Systèmes Simulia Corp, 2009.

[30] K. Miura and S. Pellegrino, *Forms and Concepts for Lightweight Structures*. Cambridge University Press, 2020. DOI: 10.1017/9781139048569.

[31] N. H. Reddy and S. Pellegrino, "Dynamics of the Caltech SSPP deployable structures: Structure–mechanism interaction and deployment envelope," in *AIAA SciTech 2023 Forum*, 2023, p. 2065. DOI: 10.2514/6.2023-2065,

[32] *OptiTrack documention*. [Online]. Available: https://docs.optitrack.com/.

[33] I. Daniel and O. Ishai, *Engineering Mechanics of Composite Materials*. Oxford University Press, 2005.

[34] T. Faschinger, "Integration of thin-film photovoltaics into ultralight deployable space structures," M.S. thesis, ETH Zurich, 2022.

[35] N. H. Reddy and S. Pellegrino, "Time-efficient geometrically non-linear finite element simulations of thin shell deployable structures," in *AIAA SciTech 2021 Forum*. 2021, p. 1795. DOI: 10.2514/6.2021-1795,

[36] D. Bushnell and W. D. Bushnell, *Shellbuckling.com*, 2015. [Online]. Available: shellbuckling.com.

[37] N. Hu and R. Burgueño, "Buckling-induced smart applications: Recent advances and trends," *Smart Materials and Structures*, vol. 24, no. 6, p. 063 001, 2015.

[38] P. M. Reis, "A perspective on the revival of structural (in) stability with novel opportunities for function: From buckliphobia to buckliphilia," *Journal of Applied Mechanics*, vol. 82, no. 11, p. 111 001, 2015.

[39] C. Bisagni and P. Cordisco, "An experimental investigation into the buckling and post-buckling of cfrp shells under combined axial and torsion loading," *Composite Structures*, vol. 60, no. 4, pp. 391–402, Jun. 2003. DOI: 10.1016/s0263-8223(03)00024-2.

[40] D. Galletly and S. Guest, "Bistable composite slit tubes. II. A shell model," *International Journal of Solids and Structures*, vol. 41, no. 16-17, pp. 4503–4516, Aug. 2004. DOI: 10.1016/j.ijsolstr.2004.02.037.

[41] A. Lazarus and P. Reis, "Soft actuation of structured cylinders through auxetic behavior," *Advanced Engineering Materials*, vol. 17, no. 6, pp. 815–820, Jan. 13, 2015. DOI: 10.1002/adem.201400433.

[42] E. Loukaides, S. Smoukov, and K. Seffen, "Magnetic actuation and transition shapes of a bistable spherical cap," *International Journal of Smart and Nano Materials*, vol. 5, no. 4, pp. 270–282, Oct. 2, 2014. DOI: 10.1080/19475411.2014.997322.

[43] S. Pellegrino, *Deployable structures*. Springer, 2014, vol. 412.

[44] C. Leclerc, L. Wilson, M. Bessa, and S. Pellegrino, "Characterization of ultra-thin composite triangular rollable and collapsible booms," in *4th AIAA Spacecraft Structures Conference*. 2017, p. 172.

[45] M. Sakovsky and S. Pellegrino, "Closed cross-section dual-matrix composite hinge for deployable structures," *Composite Structures*, vol. 208, pp. 784–795, Jan. 2019. DOI: 10.1016/j.compstruct.2018.10.040.

[46] F. Dai, H. Li, and S. Du, "A multi-stable lattice structure and its snap-through behavior among multiple states," *Composite Structures*, vol. 97, pp. 56–63, 2013.

[47] A. Pirrera, D. Avitabile, and P. Weaver, "On the thermally induced bistability of composite cylindrical shells for morphing structures," *International Journal of Solids and Structures*, vol. 49, no. 5, pp. 685–700, Mar. 2012. DOI: 10.1016/j.ijsolstr.2011.11.011.

[48] C. R. Calladine, "Understanding imperfection-sensitivity in the buckling of thin-walled shells," *Thin-Walled Structures*, vol. 23, no. 1-4, pp. 215–235, 1995. DOI: 10.1016/0263-8231(95)00013-4.

[49] O. C. Zienkiewicz and R. L. Taylor, *The finite element method for solid and structural mechanics, 6th edition*. Elsevier, 2005.

[50] T. Hughes, J. Cottrell, and Y. Bazilevs, "Isogeometric analysis: Cad, finite elements, NURBS, exact geometry and mesh refinement," *Computer Methods in Applied Mechanics and Engineering*, vol. 194, no. 39-41, pp. 4135–4195, Oct. 2005. DOI: 10.1016/j.cma.2004.10.008.

[51] J. Kiendl, K.-U. Bletzinger, J. Linhard, and R. Wüchner, "Isogeometric shell analysis with kirchhoff–love elements," *Computer Methods in Applied Mechanics and Engineering*, vol. 198, no. 49-52, pp. 3902–3914, Nov. 2009. DOI: 10.1016/j.cma.2009.08.013.

[52] D. Benson, Y. Bazilevs, M.-C. Hsu, and T. Hughes, "A large deformation, rotation-free, isogeometric shell," *Computer Methods in Applied Mechanics and Engineering*, vol. 200, no. 13-16, pp. 1367–1378, Mar. 2011. DOI: 10.1016/j.cma.2010.12.003.

[53] R. Echter, B. Oesterle, and M. Bischoff, "A hierarchic family of isogeometric shell finite elements," *Computer Methods in Applied Mechanics and Engineering*, vol. 254, pp. 170–180, Feb. 2013. DOI: 10.1016/j.cma.2012.10.018.

[54] B. Oesterle, E. Ramm, and M. Bischoff, "A shear deformable, rotation-free isogeometric shell formulation," *Computer Methods in Applied Mechanics and Engineering*, vol. 307, pp. 235–255, Aug. 2016. DOI: 10.1016/j.cma.2016.04.015.

[55] B. Oesterle, R. Sachse, E. Ramm, and M. Bischoff, "Hierarchic isogeometric large rotation shell elements including linearized transverse shear parametrization," *Computer Methods in Applied Mechanics and Engineering*, vol. 321, pp. 383–405, Jul. 2017. DOI: 10.1016/j.cma.2017.03.031.

[56] N. Nguyen-Thanh, K. Zhou, X. Zhuang, *et al.*, "Isogeometric analysis of large-deformation thin shells using rht-splines for multiple-patch coupling," *Computer Methods in Applied Mechanics and Engineering*, vol. 316, pp. 1157–1178, Apr. 2017. DOI: 10.1016/j.cma.2016.12.002.

[57] L. Leonetti, F. Liguori, D. Magisano, and G. Garcea, "An efficient isogeometric solid-shell formulation for geometrically nonlinear analysis of elastic shells," *Computer Methods in Applied Mechanics and Engineering*, vol. 331, pp. 159–183, Apr. 2018. DOI: 10.1016/j.cma.2017.11.025.

[58] B. Oesterle, S. Bieber, R. Sachse, E. Ramm, and M. Bischoff, "Intrinsically locking-free formulations for isogeometric beam, plate and shell analysis," *Proceedings in Applied Mathematics and Mechanics*, vol. 18, no. 1, e201800399, Dec. 2018. DOI: 10.1002/pamm.201800399.

[59] S. Bieber, B. Oesterle, E. Ramm, and M. Bischoff, "A variational method to avoid locking-independent of the discretization scheme," *International Journal for Numerical Methods in Engineering*, vol. 114, no. 8, pp. 801–827, Feb. 6, 2018. DOI: 10.1002/nme.5766.

[60] Y. Guo, H. Do, and M. Ruess, "Isogeometric stability analysis of thin shells: From simple geometries to engineering models," *International Journal for Numerical Methods in Engineering*, vol. 118, no. 8, pp. 433–458, Jan. 17, 2019. DOI: 10.1002/nme.6020.

[61] J. Praciano, P. Barros, E. Barroso, E. Parente, Á. Holanda, and J. Sousa, "An isogeometric formulation for stability analysis of laminated plates and shallow shells," *Thin-Walled Structures*, vol. 143, p. 106 224, Oct. 2019. DOI: 10.1016/j.tws.2019.106224.

[62] T. Le-Manh and J. Lee, "Postbuckling of laminated composite plates using NURBS-based isogeometric analysis," *Composite Structures*, vol. 109, pp. 286–293, Mar. 2014. DOI: 10.1016/j.compstruct.2013.11.011.

[63] S. Shojaee, N. Valizadeh, E. Izadpanah, T. Bui, and T.-V. Vu, "Free vibration and buckling analysis of laminated composite plates using the NURBS-based isogeometric finite element method," *Composite Structures*, vol. 94, no. 5, pp. 1677–1693, Apr. 2012. DOI: 10.1016/j.compstruct.2012.01.012.

[64] S. Pellegrino, "Folding and deployment of thin shell structures," in *CISM International Centre for Mechanical Sciences*, D. Bigoni, Ed. Vienna: Springer Vienna, 2015, vol. 562, pp. 179–267. DOI: 10.1007/978-3-7091-1877-1_5.

[65] K. Seffen and S. Pellegrino, "Deployment dynamics of tape springs," *Proceedings of the Royal Society of London. Series A: Mathematical, Physical and Engineering Sciences*, vol. 455, no. 1983, pp. 1003–1048, 1999.

[66] H. Mallikarachchi and S. Pellegrino, "Design of ultrathin composite self-deployable booms," *Journal of Spacecraft and Rockets*, vol. 51, no. 6, pp. 1811–1821, Nov. 2014. DOI: 10.2514/1.a32815.

[67] K. Seffen, B. Wang, and S. Guest, "Folded orthotropic tape-springs," *Journal of the Mechanics and Physics of Solids*, vol. 123, pp. 138–148, Feb. 2019. DOI: 10.1016/j.jmps.2018.09.017.

[68] K. Seffen, Z. You, and S. Pellegrino, "Folding and deployment of curved tape springs," *International Journal of Mechanical Sciences*, vol. 42, no. 10, pp. 2055–2073, Oct. 2000. DOI: 10.1016/s0020-7403(99)00056-9.

[69] A. M. Watt, "Deployable structures with self-locking hinges," Ph.D. dissertation, University of Cambridge, 2003.

[70] L. Wilson, E. Gdoutos, and S. Pellegrino, "Tension-stabilized coiling of isotropic tape springs," *International Journal of Solids and Structures*, vol. 188-189, pp. 103–117, Apr. 2020. DOI: 10.1016/j.ijsolstr.2019.09.010.

[71] L. Piegl and W. Tiller, *The NURBS book*, 1996. DOI: 10.1007/978-3-642-59223-2.

[72] M. Spink, *NURBS toolbox for MATLAB, https://octave.sourceforge.io/nurbs/overview.html*, 2010. [Online]. Available: https://octave.sourceforge.io/nurbs/overview.html.

[73] T. Hughes and W. Liu, "Nonlinear finite element analysis of shells: Part I. Three-dimensional shells," *Computer Methods in Applied Mechanics and Engineering*, vol. 26, no. 3, pp. 331–362, Jun. 1981. DOI: 10.1016/0045-7825(81)90121-3.

[74] A. Huerta, A. Rodríguez-Ferran, P. Díez, and J. Sarrate, "Adaptive finite element strategies based on error assessment," *International Journal for Numerical Methods in Engineering*, vol. 46, no. 10, pp. 1803–1818, 1999.

[75] M. Ainsworth and J. T. Oden, "A posteriori error estimation in finite element analysis," *Computer Methods in Applied Mechanics and Engineering*, vol. 142, no. 1-2, pp. 1–88, 1997.

[76] T. Grätsch and K.-J. Bathe, "A posteriori error estimation techniques in practical finite element analysis," *Computers & Structures*, vol. 83, no. 4-5, pp. 235–265, 2005.

[77] P. Hansbo, "Three lectures on error estimation and adaptivity," in *Adaptive Finite Elements in Linear and Nonlinear Solid and Structural Mechanics*, E. Stein, Ed. Springer, 2005.

[78] R. Moshfegh, X. Li, and L. Nilsson, "Adaptive finite element simulation of sheet metal forming processes using gradient based indicators," in *International LS-DYNA Users Conference Simulation, Dearborn, Michigan*, Citeseer, 2000.

[79] Q. Xie, K. Sze, and Y. Zhou, "Drape simulation using solid-shell elements and adaptive mesh subdivision," *Finite Elements in Analysis and Design*, vol. 106, pp. 85–102, 2015.

[80] O. C. Zienkiewicz and J. Z. Zhu, "A simple error estimator and adaptive procedure for practical engineerng analysis," *International Journal for Numerical Methods in Engineering*, vol. 24, no. 2, pp. 337–357, 1987.

[81] K. M. Okstad, "Adaptive methods for nonlinear finite element analysis of shell structures," Ph.D. dissertation, Department of Structural Engineering, The Norwegian Institute of Technology, Trondheim, Norway, 1994.

[82] J. Riccius, K. Schweizerhof, and M. Baumann, "Combination of adaptivity and mesh smoothing for the finite element analysis of shells with intersections," *International Journal for Numerical Methods in Engineering*, vol. 40, no. 13, pp. 2459–2474, 1997.

[83] J. Neumann, J. Riccius, and K. Schweizerhof, "Adaptive analysis of dynamically loaded shell structures," *Proc. WCCM Buenos Aires: Computational Mechanics: New trends and applications", S. Idelsohn, E. Onate and E. Dvorkin (Eds.), CIMNE, Barcelona, Spain*, 1998.

[84] Z. Yue, "Adaptive superposition of finite element meshes in linear and nonlinear dynamic analysis," Ph.D. dissertation, University of Maryland, College Park, 2005.

[85] S. Kizio, K. Schweizerhof, A. Düster, and E. Rank, "Benchmark computations of low and high order shell elements on adaptively generated fe meshes," in *Proceedings*, vol. 10, 2006, pp. 311–330.

[86] P. Destuynder, Y. Moguen, and M. Salaün, "Adaptive mesh refinements for thin shells whose middle surface is not exactly known," *Computer methods in applied mechanics and engineering*, vol. 197, no. 51-52, pp. 4789–4811, 2008.

[87] Z. Ullah, W. Coombs, and C. Augarde, "Parallel computations in nonlinear solid mechanics using adaptive finite element and meshless methods," *Engineering Computations*, 2016.

[88] S. Almi, S. Belz, S. Micheletti, and S. Perotto, "A dimension-reduction model for brittle fractures on thin shells with mesh adaptivity," *Mathematical Models and Methods in Applied Sciences*, vol. 31, no. 01, pp. 37–81, 2021.

[89] Y. Wang, "Mesh refinement of finite element method for free vibration analysis of variable geometrical rotating cylindrical shells," *Engineering Computations*, vol. 40, no. 1, pp. 210–228, 2023.

[90] O. C. Zienkiewicz and J. Z. Zhu, "The superconvergent patch recovery and a posteriori error estimates. part 1: The recovery technique," *International Journal for Numerical Methods in Engineering*, vol. 33, no. 7, pp. 1331–1364, 1992.

[91] O. C. Zienkiewicz and J. Z. Zhu, "The superconvergent patch recovery and a posteriori error estimates. part 2: Error estimates and adaptivity," *International Journal for Numerical Methods in Engineering*, vol. 33, no. 7, pp. 1365–1382, 1992.

[92] C. Lee and R. Hobbs, "Automatic adaptive refinement for shell analysis using nine-node assumed strain element," *International Journal for Numerical Methods in Engineering*, vol. 40, no. 19, pp. 3601–3638, 1997.

[93] A. Yazdani, H. Riggs, and A. Tessler, "Stress recovery and error estimation for shell structures," *International Journal for Numerical Methods in Engineering*, vol. 47, no. 11, pp. 1825–1840, 2000.

[94] C.-S. Han and P. Wriggers, "An h-adaptive method for elasto-plastic shell problems," *Computer Methods in Applied Mechanics and Engineering*, vol. 189, no. 2, pp. 651–671, 2000.

[95] J. Villard and H. Borouchaki, "Adaptive meshing for cloth animation," *Engineering with Computers*, vol. 20, pp. 333–341, 2005.

[96] W. Li, N. Nguyen-Thanh, J. Huang, and K. Zhou, "Adaptive analysis of crack propagation in thin-shell structures via an isogeometric-meshfree moving least-squares approach," *Computer Methods in Applied Mechanics and Engineering*, vol. 358, p. 112 613, 2020.

[97] E. Stein, B. Seifert, S. Ohnimus, and C. Carstensen, "Adaptive finite element analysis of geometrically non-linear plates and shells, especially buckling," *International Journal for Numerical Methods in Engineering*, vol. 37, no. 15, pp. 2631–2655, 1994.

[98] A. Huerta, A. Rodriguez-Ferran, and P. Diez, "Error estimation and adaptivity for nonlinear fe analysis," *International Journal of Applied Mathematics and Computer Science*, vol. 12, no. 1, pp. 59–70, 2002.

[99] T. Erhart, W. A. Wall, and E. Ramm, "Robust adaptive remeshing strategy for large deformation, transient impact simulations," *International Journal for Numerical Methods in Engineering*, vol. 65, no. 13, pp. 2139–2166, 2006.

[100] L. Fourment and J.-L. Chenot, "Error estimators for viscoplastic materials: Application to forming processes," *Engineering Computations*, vol. 12, no. 5, pp. 469–490, 1995.

[101] J. Mosler and M. Ortiz, "Variational h-adaption in finite deformation elasticity and plasticity," *International Journal for Numerical Methods in Engineering*, vol. 72, no. 5, pp. 505–523, 2007.

[102] C. Militello and C. Felippa, "r-adaptive methods based on element-level error indicators for parallel analysis of plates and shells," in *33rd Structures, Structural Dynamics and Materials Conference*, 1991, p. 2289.

[103] P. Nordlund, A. Giannakopoulos, and B. Häggblad, "Adaptive mesh-updating methods for non-linear finite element analysis of shells," *International Journal for Numerical Methods in Engineering*, vol. 43, no. 8, pp. 1523–1544, 1998.

[104] M. Cho and S. Jun, "r-adaptive mesh generation for shell finite element analysis," *Journal of Computational Physics*, vol. 199, no. 1, pp. 291–316, 2004.

[105] L. Ma and W. S. Klug, "Viscous regularization and r-adaptive remeshing for finite element analysis of lipid membrane mechanics," *Journal of Computational Physics*, vol. 227, no. 11, pp. 5816–5835, 2008.

[106] X. Gu, "Development and implementation of adaptive mesh refinement methods for numerical simulations of metal forming and machining," Ph.D. dissertation, Dortmund Technical University, 2008.

[107] J. F. Shepherd, M. W. Dewey, A. C. Woodbury, S. E. Benzley, M. L. Staten, and S. J. Owen, "Adaptive mesh coarsening for quadrilateral and hexahedral meshes," *Finite Elements in Analysis and Design*, vol. 46, no. 1-2, pp. 17–32, 2010.

[108] M. Kardani, M. Nazem, A. J. Abbo, D. Sheng, and S. W. Sloan, "Refined h-adaptive finite element procedure for large deformation geotechnical problems," *Computational Mechanics*, vol. 49, pp. 21–33, 2012.

[109] P. Šolín, J. Červenỳ, and I. Doležel, "Arbitrary-level hanging nodes and automatic adaptivity in the hp-fem," *Mathematics and Computers in Simulation*, vol. 77, no. 1, pp. 117–132, 2008.

[110] J. L. D. Calle, P. R. Devloo, and S. M. Gomes, "Implementation of continuous hp-adaptive finite element spaces without limitations on hanging sides and distribution of approximation orders," *Computers & Mathematics with Applications*, vol. 70, no. 5, pp. 1051–1069, 2015.

[111] R. E. Bank, A. H. Sherman, and A. Weiser, "Some refinement algorithms and data structures for regular local mesh refinement," *Scientific Computing, Applications of Mathematics and Computing to the Physical Sciences*, vol. 1, pp. 3–17, 1983.

[112] R. Verfürth, "A posteriori error estimation and adaptive mesh-refinement techniques," *Journal of Computational and Applied Mathematics*, vol. 50, no. 1-3, pp. 67–83, 1994.

[113] C. Carstensen, "An adaptive mesh-refining algorithm allowing for an h 1 stable l 2 projection onto courant finite element spaces," *Constructive Approximation*, vol. 20, pp. 549–564, 2004.

[114] K.-F. Tchon, J. Dompierre, and R. Scamarero, "Automated refinement of conformal quadrilateral and hexahedral meshes," *International Journal for Numerical Methods in Engineering*, vol. 59, no. 12, pp. 1539–1562, 2004.

[115] B. D. Anderson, S. E. Benzley, and S. J. Owen, "Automatic all quadrilateral mesh adaption through refinement and coarsening," in *Proceedings of the 18th International Meshing Roundtable*, Citeseer, 2009, pp. 557–574.

[116] X. Liang, M. S. Ebeida, and Y. Zhang, "Guaranteed-quality all-quadrilateral mesh generation with feature preservation," in *Proceedings of the 18th International Meshing Roundtable*, Springer, 2009, pp. 45–63.

[117] X. Zhao, S. Mao, and Z. Shi, "Adaptive finite element methods on quadrilateral meshes without hanging nodes," *SIAM Journal on Scientific Computing*, vol. 32, no. 4, pp. 2099–2120, 2010.

[118] L. Kobbelt, "Interpolatory subdivision on open quadrilateral nets with arbitrary topology," in *Computer Graphics Forum*, Wiley Online Library, vol. 15, 1996, pp. 409–420.

[119] D. Perić, C. Hochard, M. Dutko, and D. Owen, "Transfer operators for evolving meshes in small strain elasto-placticity," *Computer Methods in Applied Mechanics and Engineering*, vol. 137, no. 3-4, pp. 331–344, 1996.

[120] I. Tiller, K. M. Mathisen, and K. M. Okstad, "On the mapping of solution variables within adaptive analysis of nonlinear shell-type problems," in *European Congress on Computational Methods in Applied Sciences and Engineering*. 2000.

[121] G. Papazafeiropoulos, M. Muñiz-Calvente, and E. Martínez-Pañeda, "Abaqus2Matlab: A suitable tool for finite element post-processing," *Advances in Engineering Software*, vol. 105, pp. 9–16, 2017.